Dynamical Correlations of Disordererd One-dimensional Quantum Antiferromagnets

Master's Thesis in Physics

Presented by

Max Hörmann

August 14, 2017

Institut für Theoretische Physik I
Friedrich-Alexander Universität Erlangen-Nürnberg

Supervisor: Prof. Dr. Kai Phillip Schmidt

Abstract

A general framework for calculating the zero-temperature dynamic structure factor of the dimerized spin-$1/2$ chain and the Heisenberg spin-$1/2$ two-leg ladder in the presence of disorder is given. For that the methods of perturbative continuous unitary transformations and white graph expansions about the limit of isolated dimers are applied to derive the physical properties of the elementary triplon excitations. This way numerical high-precision results are obtained for large finite systems if the strength of the perturbation lies within the convergence radius of the perturbative expansion. All sorts of disorder can be treated within the framework. Apart from dynamical correlations of inelastic neutron scattering observables also the density of states and the inverse participation ratio is calculated. One- and two-triplon properties are investigated. Not only one- but also two-triplon states are found to be localized in the sense that almost all the weight of their eigenfunctions sits on a finite number of position states. The mean of the absolute squared one-triplon effective Hamiltonian in momentum space is derived analytically. Its values are used to calculate the self-energy within the self-consistent Born approximation for rung disorder and within the Born approximation for leg disorder. Various bimodal leg and rung disorder configurations are compared numerically and show the same qualitative behaviour of lifetimes as expected by the former theoretical results. While for the Lorentzian convolved dynamic structure factor Gaussian disorder on the leg shows similar features as bimodal disorder for Gaussian rung disorder the dynamic structure factor is very different especially for two-triplon weights. The density of states of bimodal rung disorder and also of strong enough bimodal leg disorder configurations is found to not converge to a smooth distribution in the one-triplon sector. In contrast to that Gaussian disorder always shows a smooth density of states. Sharp two-triplon bound states are found to get a finite lifetime but can still be separated as peaks from the continuum for some sorts of disorder. The dynamic structure factor calculations model material classes like $\mathrm{BPCB}_x\mathrm{C}_{1-x}$. Quantitatively trustful calculations with the couplings of that material have been performed and it is found that two-triplon bound states might survive not to big concentrations of bromine atoms.

Kurzzusammenfassung

Eine Methode zur Berechnung des dynamischen Strukturfaktors der dimerisierten Spin-$1/2$ Kette und der Heisenberg Spin-$1/2$ Zweibeinleiter am absoluten Temperaturnullpunkt und in Gegenwart von Unordnung ist entwickelt worden. Hierfür benutzt wurden perturbative kontinuierliche Transformationen um den Limes isolierter Dimere herum sowie sogenannte Weiße-Graphen Entwicklungen. Damit können die physikalischen Eigenschaften der elementaren Triplon Anregungen bestimmt werden. Alle möglichen Formen der Unordnung lassen sich mit der Methode untersuchen. Neben dynamischen Korrelationen inelastischer Neutronstreuobservablen wurde auch die Zustandsdichte und das inverse Partizipationsverhältnis berechnet. Anregungen von einem und zwei Triplonen wurden untersucht. In beiden Fällen sind die Anregungen lokalisiert in dem Sinne, dass fast das Ganze Gewicht ihrer Eigenfunktionen auf eine endliche Anzahl von Ortseigenzuständen verteilt ist. Der Mittelwert des Absolutquadrats des effektiven Hamilton-Operators im Sektor mit nur einem Triplon wurde analytisch bestimmt. Seine Werte wurden benutzt um die Selbstenergie innerhalb der selbst-konsistenten Born-Näherung für Sprossen- und innerhalb der Born-Näherung für Holmenunordnung auszurechnen. Verschiedenste bimodale Sprossen- und Holmenunordnungen wurden numerisch verglichen und qualitativ wurde das selbe Verhalten gefunden wie theoretisch erwartet. Der dynamische Strukturfaktor verhält sich für Gauß'sche Unordnung auf den Holmen ähnlich zu dem einer bimodalen Holmverteilung, falls er mit einer Lorentzkurve gefaltet wird. Dem entgegen zeigt sich bei Sprossen-Unordnung ein komplett anderes Verhalten, wenn man bimodale mit Gauß'scher Unordnung vergleicht. Innerhalb der Ein-Triplon Anregungen findet man keine glatte Zustandsdichte bei starker bimodaler Holmenunordnung und bei Sprossenunordnung. Im Gegensatz dazu zeigt Gauß'sche Unordnung immer eine glatte Zustandsdichte. Die gebundenen Zustände innerhalb des Zwei-Triplon Sektors bekommen durch die Unordnung eine endliche Lebensdauer. Für manche Arten von Unordnung können sie noch gut vom Kontinuum abgegrenzt werden. Die Berechnungen zum dynamischen Strukturfaktor können zur Modellierung von Materialklassen wie $\mathrm{BPCB}_x\mathrm{C}_{1-x}$ benutzt werden. Präzise Rechnungen mit Kopplungsstärken dieses Materials wurden durchgeführt und es wurde gefunden, dass für nicht zu große Konzentrationen von Brom-Atomen die Signaturen von Zwei-Triplon gebundenen Zuständen zu sehen bleiben.

Contents

1. Introduction

1.1. Disorder in quantum systems

Understanding the collective behaviour of matter by the properties of its single constituents is one of the central paradigms of modern science. Correlated many body states like spin liquids and superconductors can only be understood by the interplay of many single entities. To gain a systematic understanding of collective phenomena is decisive for identifying fundamentally new behaviour. It is thus also important for technological progress.

Disorder is ubiquitous in nature. Perfectly ordered structures are the exception rather than the rule. However, modern theory of solid state physics is built up on the basis of Bloch's theory of electrons states in a perfect regular lattice and Debye's and others work on phonons [1]. Interactions between electrons and phonons and lattice impurities can be accounted for with the Boltzmann equation when the concentration of impurities is low enough [1]. In many situations this is not the case anymore. One example material are substitutional alloys that are widely used in metallurgy. Generally doping produces disorder. Magnetic materials can obtain a quenched randomness in their exchange couplings by it.

Quantum antiferromagnets with such quenched disorder are starting to get in the focus of inelastic neutron scattering measurements. Already zero-temperature physics of non-disordered quantum magnets shows a rich spectrum of behaviour. Quantum phase transitions (QPT) between long-range non-disordered and paramagnetic phases [2] and magnetic monopoles in three dimensional frustrated spin systems like spin ice [3] are just two of many examples. In many situations it is not completely known how disorder affects such properties. For QPT's the effect of disorder was investigated in the past and can be summarized in short as follows. Disorder can substantially change the behaviour of a system close to a quantum phase transition and even stop the transition to occur [4]. The Harris criterion $d\nu > 2$ can be used to predict whether disorder is globally strong enough to change the critical point of a QPT. Here ν is the exponent of the correlation length $\propto |r|^{-\nu}$ and d the dimension. If fulfilled the clean critical point remains stable against weak disorder [4]. Speaking sloppy the Harris criterion is based on a global estimate of the systems distance to the quantum critical point. The global distance always has to stay bigger than local fluctuations of the distance. Potential effects of exponentially rare subclusters on macroscopic variables are not taken into account. If the Harris criterion is not fulfilled these rare regions change the QPT. One scenario is that macroscopic variables converge to a distribution with a certain width. It is also possible that for strong enough disorder the width of this distribution diverges [4]. Such rare region effects are strongest for temperature $T = 0$ since the effective dimensionality is $d_{\text{eff}} = d + 1$ then. One reason why rare regions are of importance is that the density of states for energies around the gap of a system can be built out of position eigenstates lying in the rare regions. Although exponentially rare they then can have a power-law density of states since the energy of the gap goes to zero exponentially as well with increasing size of the rare region [4]. In this work the focus is not laid on the interplay of disorder and QPT although this is an interesting topic with emerging effects due to disorder.

In 1957 Nobel prize laureate Philip Warren Anderson was confronted with an experiment that showed anomalously long relaxation times of electron spins in doped semiconductors performed by George Feher's group at Bell Labs. This was one motivation for his famous paper "Absence of diffusion in certain random lattices". He used a tight-binding model of an electron in a disordered lattice to show that electrons can localize in space [5]. The concept of localized electrons broke with the conventional diffusion picture.

Andersons approach based on a self-consistent diagrammatic expansions of the local density of states. Many more methods were developed in the following years to treat disordered quantum mechanical problems. Approaches range from calculations on an augmented space by Mokerjee in 1973 [6] to methods using supersymmetric statistical mechanics [7]. Localization became an important aspect to look at in physics as well as its cause - disorder. For macroscopic quantities like conductivity one can observe an exponentially decreased conductivity as a consequence of localized electron states. To know when disorder is sufficiently strong to lead to such an effect is thus important. One found that one-particle excitations of disordered systems can change from extended as in the non-disordered case to localized in two and three dimensions. Stronger disorder is needed in three dimensions for localisation to occur. Systems can undergo a transition from conducting to isolating while the strength of disorder is increased. Especially methods using supersymmetric statistical mechanics are well suited to predict those mobility edges [7]. In one dimensions the excitations are almost always localized and no transition can occur [8, 1].

For electronic systems it was found that disordered structures can lead to localization. Disordered problems in magnetic systems on a lattice are merely different mathematically. They mostly can be reduced to a tight-binding like Hamiltonian. Due to the similar mathematical structure magnetic excitations in disordered quantum magnets are also almost always localized in one dimension and localization will be an important aspect of this work.

Work on disorder in quantum magnets in the past mainly focused on ground state properties like QPT's. Dynamical correlations as measured in an inelastic neutron scattering experiment were first described using density matrix renormalization group (DMRG) methods in 2001 [9]. Also most work on ground state properties and QPT's was done with DMRG methods [10, 11]. In 2013 another approach using bond-operator mean field techniques developed by Matthias Vojta could qualitatively describe the behaviour of the dynamic structure factor close to and at quantum critical points of the QPT between the paramagnetic and long-range non-disordered phase in the Heisenberg bilayer with bimodal quenched randomness [12].

The effect of localization on the dynamic structure measured and determined by inelastic neutron scattering experiments is different to the one on conductivity. Inelastic neutron scattering will always measure momentum and energy resolved dynamical correlations no matter how localized the magnetic states in the material are. The shape of the intensity distribution in momentum and energy space however will depend strongly on the degree of localization. Since the resolution of such detectors are getting better and better and the disorder strength in quantum magnets can be adjusted very precisely it is called for quantitatively reliable theoretical calculations [13]. Mean field techniques are quite accurate in higher dimensions than one and have the advantage of being able to tune through the QPT [12]. However in one dimension their accuracy can not be called quantitatively anymore for high expansion parameters in models like the Heisenberg spin ladder [14, 15]. Renormalization group based disorder techniques often start with choosing the strongest bond. This naturally leads to problems when one studies bimodal disorder. Quantum Monte Carlo methods have to introduce a finite temperature and then need to extrapolate to temperature $T = 0$ which leads to a extrapolation uncertainty. The perturbative continuous unitary transformation (pCUT) approach used here has no such problems for expansion parameters in the convergence radius. The ansatz is independent of the disorder distribution. Not only the ground state but also the excitations can be calculated in the presence of disorder. Hence localization effects are captured by the method in a quantitative manner. Furthermore not only one quasi-particle energy eigenstates but also those containing two and more quasi-particles can be obtained with the method. This way for the first time the effect of disorder on bound states of two magnetic quasi-particles could be calculated. Only recently (2017) bound states signatures were captured in inelastic neutron scattering measurements on the spin-ladder material BPCC [16].

1.1.1. Disordered quantum antiferromagnets

The quantum antiferromagnet BPCC ($(\mathrm{C_5D_{12}N})_2\mathrm{CuCl_4}$) is of special interest because replacing the chlorine atoms by bromine atoms creates a disordered quantum antiferromagnet. The material BPCC has the monoclinic space group P2_1/c as structure. In one of the three directions it behaves like the two-leg spin ladder. These ladder segments only couple weakly since in the other two directions no ladders can form because of alternating different orientations of the ladder segment rungs (see Fig. 1.1) [16]. The material is thus effectively quasi-one dimensional in its magnetic behaviour [16] Plot is taken from [16]. The copper atoms carry the spin-$1/2$ in BPCC. Exchanges between the four chlorine atoms on each site of the material lead to antiferromagnetic exchange constants. The rung coupling has a strength of $J^{\perp}/\mathrm{k_B} = 3.42\mathrm{K}$ and the leg coupling of $J^{\parallel}/\mathrm{k_B} = 1.34\mathrm{K}$ [16]. For the complementary material BPCB where all chlorine atoms are replaced by bromine atoms the structure remains such that it is a two-leg ladder with coupling constants $J^{\perp}/\mathrm{k_B} = 12.9\mathrm{K}$ and $J^{\parallel}/\mathrm{k_B} = 3.6\mathrm{K}$ [17].

Via intentional doping the coupling constants range between those two maximum values. When one has reached a certain concentration of bromine and chlorine atoms these atoms do not change their position anymore. The term quenched randomness is used because it is constant in time. The spatial variation of chlorine and bromine however can be assumed to be purely random such that for every possible chlorine respectively bromine place there is a probability of x respectively $1 - x$ for such an atom to be there. Such doping could already be achieved and the so obtained materials can be seen in Fig. 1.2 [13].

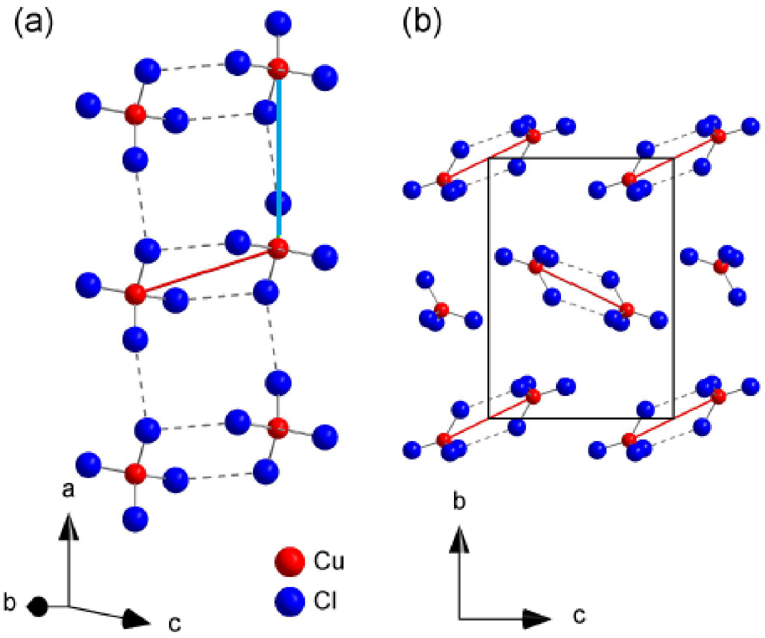

Fig. 1.1: (a) Ladder segment of BPCC. The direction of the ladder is along the a-axis. The copper atoms carry a spin-$1/2$. The legs and rungs of the ladder are coupled by Heisenberg couplings but the strength of the rung coupling is significantly stronger.
(b) Different orientations of ladder segments along the other two axis b and c are shown. Because of these different orientations the coupling between different ladder segments is very small and the material can be modelled as a quasi one-dimensional ladder.

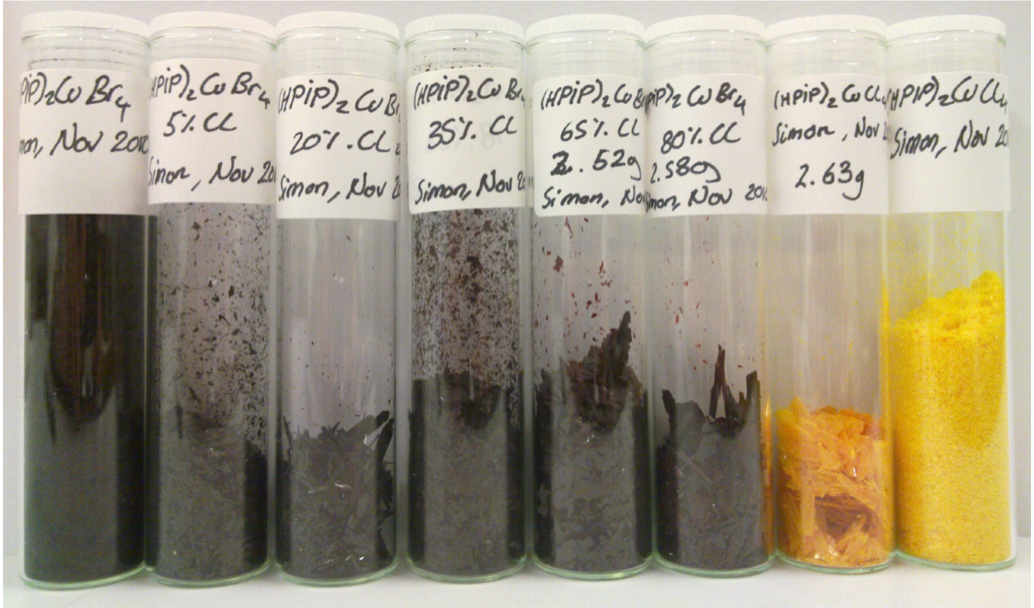

Fig. 1.2: Bromine doped BPCC is shown. The black probe on the left contains only bromine atoms and the one on the right only chlorine atoms. The probes in between contain both sorts and the concentration of chlorine is increased from left to right. The picture is taken from the PhD thesis of Simon Ward who investigated the properties of these doped materials by neutron scattering measurements [13].

1.1.2. Inelastic neutron scattering

Inelastic neutron scattering on the disordered material $((\mathrm{C}_5\mathrm{D}_{12}\mathrm{N})_2\mathrm{Cu}(\mathrm{Cl}_4^{0.1}\mathrm{Br}_4^{0.9}))$ in the presence of a $15\,\mathrm{T}$ magnetic field was only done recently (see Fig. 1.3) [13]. Measurements for other concentrations and without magnetic field come into reach. This is great since it offers the possibility to measure the effect of disorder on spin ladders quantitatively in an experiment for different disorder strengths corresponding to different concentrations of chlorine and bromine. It is always instructive to have such experimental data available since theoretical predictions for disordered systems can be validated. Theoretical investigations and quantitative numerical calculations of the dynamic structure factor of this material class are one subject of the thesis.

Also as already mentioned only recently for the first time the theoretical prediction of two-triplon bound states could be experimentally validated by means of inelastic neutron scattering measurements [16]. The measurements were done on the material BPCC. This makes it even more exciting that just this material can be made disordered via doping of bromine atoms. So far not much is known about the impact of disorder on two-triplon bound states. For the first time in this thesis dynamical correlations of disordered one-dimensional quantum antiferromagnets are calculated in the two-triplon sector and the disorder effect on the bound states is discussed. Experiments that can potentially measure two-triplon bound states in the disordered case do not seem to be far away as the material $((\mathrm{C}_5\mathrm{D}_{12}\mathrm{N})_2\mathrm{Cu}(\mathrm{Cl}_4^{x}\mathrm{Br}_4^{1-x}))$ can

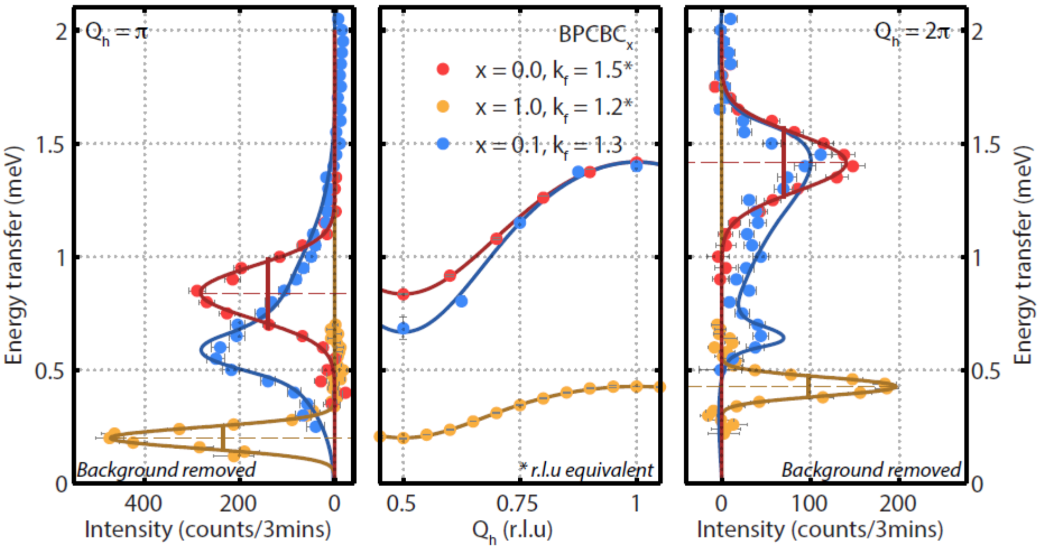

Fig. 1.3: The dotted points show inelastic neutron scattering data of Simon Ward and the plot is taken from its PhD thesis [13]. Red dots show measurements on BPCB, yellow dots on BPCC and blue dots on a sample with 10% chlorine and 90% bromine atoms. All measurements were done in the presence of a $15\,\mathrm{T}$ magnetic field. The plot in the middle shows averaged dispersion curves. On the left energy is plotted against intensity for a wavevector $k = \pi$ and on the right for $k = 0$. A disorder feature that can be seen from these plots is that the curves for fixed k have a significantly bigger width than those of the pure materials. This is due to disorder induced localization in these materials. The width of the non-disordered materials has its reason in a limited resolution of the detector only.

be synthesized for arbitrary x and as already mentioned for $x = 0$ bound states could be measured [16, 13]. Calculations of spectral densities of disordered two-leg ladder two-triplon states are thus a pressing issue and looked for.

The master thesis is organized as follows. In chapter two the quasi-one dimensional antiferromagnetic models of interest are introduced. These are the spin-$1/2$ two-leg ladder and the dimerized spin-$1/2$ chain. Furthermore leading order effects will be discussed analytically. Chapter three gives a short introduction to continuous unitary transformations and its perturbative realization via perturbative continuous unitary transformations (pCUT). For the pCUT it will be explained how it can be used to treat disordered problems and how the dynamic structure factor for a disordered problem can be calculated with it. The last chapter four gives a short classification of disorder and discusses potential momentum dependent effects on the dynamic structure factor. Convergence of numerics will be looked at and then finally the numerically obtained results of the disordered two-leg ladder dynamic structure factor will be presented.

2. Quasi one-dimensional antiferromagnetic models

2.1. Two-leg ladder

The most important model to be studied here is the quasi-one dimensional antiferromagnetic spin-$1/2$ two-leg ladder. Its spin interactions are modelled as Heisenberg couplings. The Hamiltonian of the system reads in its most general form

$$\mathcal{H} = \sum_{\nu} J_{\nu}^{\perp}\ \boldsymbol{S_{\nu,1}} \cdot \boldsymbol{S_{\nu,2}} + J_{\nu,1}^{\|}\ \boldsymbol{S_{\nu,1}} \cdot \boldsymbol{S_{\nu+1,1}} + J_{\nu,2}^{\|}\ \boldsymbol{S_{\nu,2}} \cdot \boldsymbol{S_{\nu+1,2}}. \tag{2.1}$$

$1, 2$ labels the two legs of the ladder and $\boldsymbol{S_{\nu,a}} \cdot \boldsymbol{S_{\nu',b}} = S_{\nu,a}^{x} S_{\nu',b}^{x} + S_{\nu,a}^{y} S_{\nu',b}^{y} + S_{\nu,a}^{z} S_{\nu',b}^{z}$. One sees that the model is $SU(2)$-invariant. In this general setting the coupling coefficients $J_{\nu}^{\perp}$, $J_{\nu,1}^{\|}$ and $J_{\nu,2}^{\|}$ are arbitrary for every supersite ν with only constraint to be positive reflecting the antiferromagnetic behaviour. Fig. 2.1 illustrates the model. The product of the two spin-$1/2$ spins $\boldsymbol{S_{\nu,1}}$ and $\boldsymbol{S_{\nu,2}}$ is a four dimensional linear operator. We choose its four basis states to be eigenstates of this operator. There are three degenerate symmetric states with spin one that belong to the energy $1/4$ called triplets and one antisymmetric state to the energy $-3/4$ called

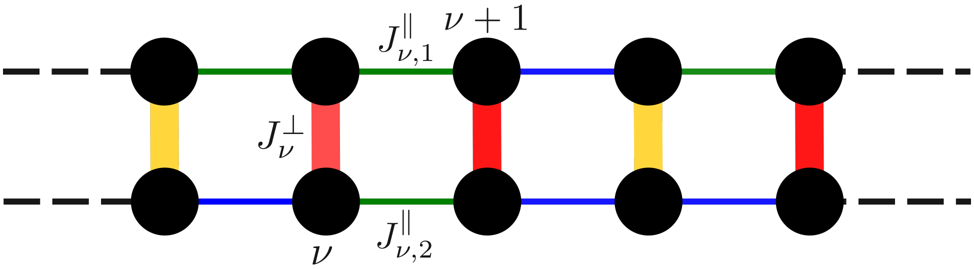

Fig. 2.1: The picture visualizes the two-leg ladder with arbitrary couplings. Different coupling strengths are shown by different colours. In principle every bond could have a different colour. Here only two different coupling strengths are allowed on rungs and legs which corresponds to bimodal disorder. The supersites are labelled by ν. Rung couplings are plotted thicker since they are assumed to be stronger than leg couplings.

singlet. Due to the degeneracy of the triplets there are various possible basis states one could choose. We do not use the states that are diagonal with respect to the magnetic quantum number here but the ones used in [18]. They are respectively given by

$$\begin{aligned} |s\rangle &= \frac{1}{\sqrt{2}}(|\uparrow\downarrow\rangle - |\downarrow\uparrow\rangle) \\ |t_x\rangle &= \frac{-1}{\sqrt{2}}(|\uparrow\uparrow\rangle - |\downarrow\downarrow\rangle) \\ |t_y\rangle &= \frac{i}{\sqrt{2}}(|\uparrow\uparrow\rangle + |\downarrow\downarrow\rangle) \\ |t_z\rangle &= \frac{1}{\sqrt{2}}(|\uparrow\downarrow\rangle + |\downarrow\uparrow\rangle)\ , \end{aligned} \tag{2.2}$$

where $|s\rangle$ is the singlet and $|t_{x,y,z}\rangle$ are the triplet states and the first arrow in the ket refers to the spin state of $\boldsymbol{S_{\nu,1}}$ and the second to the state of $\boldsymbol{S_{\nu,2}}$. Having chosen that basis one can represent $\boldsymbol{S_{\nu,1,2}}$ and $\boldsymbol{S_{\nu',1,2}}$ in terms of creation and annihilation operators

$$\begin{aligned} &t^\dagger_{\nu,\alpha}\,|s_\nu\rangle = |t_{\nu,\alpha}\rangle \\ &t^\dagger_{\nu,\alpha}\,|t_{\nu',\beta}\rangle = 0 \\ &t_{\nu,\alpha}\,|s\rangle = 0 \\ &t_{\nu,\alpha}\,|t_{\nu',\beta}\rangle = \delta_{\alpha,\beta}\delta_{\nu,\nu'}\,|s_{\nu'}\rangle \end{aligned} \tag{2.3}$$

with hardcore constraint $\sum_\alpha t^\dagger_{\nu,\alpha}t_{\nu,\alpha} \leq 1$ and $\alpha = x, y, z$ in the following way [18]:

$$S_{\nu,1\alpha} = \frac{1}{2}\left(t_{_{\nu,\alpha}} + t^\dagger_{\nu,\alpha} - i\epsilon_{\alpha\beta\gamma}t^\dagger_{\nu,\beta}t_{\nu,\gamma}\right), \tag{2.4}$$

$$S_{\nu',2\alpha} = \frac{1}{2}\left(-t_{_{\nu',\alpha}} - t^\dagger_{\nu',\alpha} - i\epsilon_{\alpha\beta\gamma}t^\dagger_{\nu',\beta}t_{\nu',\gamma}\right). \tag{2.5}$$

The representation is manifest $SU(2)$-invariant. By using the equations (2.4) and (2.5) the spin products can be expressed in terms of these creation and annihilation operators. For convenience we use the convention that over repeated indices has to be summed in the following three spin products.

$$\begin{aligned} &\boldsymbol{S_{\nu,1}} \cdot \boldsymbol{S_{\nu,2}} = \frac{1}{4}\left(t_{_{\nu,\alpha}} + t^\dagger_{\nu,\alpha} - i\epsilon_{\alpha\beta\gamma}t^\dagger_{\nu,\beta}t_{\nu,\gamma}\right)\left(-t_{_{\alpha,i}} - t^\dagger_{\nu,\alpha} - i\epsilon_{\alpha\beta\gamma}t^\dagger_{\nu,\beta}t_{\nu,\gamma}\right) \\ &= \frac{1}{4}\left(-t_{\nu,\alpha}t^\dagger_{\nu,\alpha} - t^\dagger_{\nu,\alpha}t_{\nu,\alpha} + \epsilon_{\alpha\beta'\gamma'}\epsilon_{\alpha\beta\gamma}t^\dagger_{\nu,\beta'}t_{\nu,\gamma'}t^\dagger_{\nu,\beta}t_{\nu,\gamma}\right) \\ &= \frac{1}{4}\left(-t_{\nu,\alpha}t^\dagger_{\nu,\alpha} - t^\dagger_{\nu,\alpha}t_{\nu,\alpha} + \delta_{\beta,\gamma'}\delta_{\beta',\gamma}\epsilon_{\alpha\beta'\gamma'}\epsilon_{\alpha\beta\gamma}t^\dagger_{\nu,\beta'}t_{\nu,\gamma'}t^\dagger_{\nu,\beta}t_{\nu,\gamma}\right) \\ &= \frac{1}{4}\left(-t_{\nu,\alpha}t^\dagger_{\nu,\alpha} - t^\dagger_{\nu,\alpha}t_{\nu,\alpha} + 2t^\dagger_{\nu,\alpha}t_{\nu,\alpha}\right) = \frac{1}{4}\left(-t_{\nu,\alpha}t^\dagger_{\nu,\alpha} + t^\dagger_{\nu,\alpha}t_{\nu,\alpha}\right) \\ &= -\frac{3}{4} + t^\dagger_{\nu,\alpha}t_{\nu,\alpha} \end{aligned} \tag{2.6}$$

$$
\begin{aligned}
\boldsymbol{S_{\nu,1}} \cdot \boldsymbol{S_{\nu+1,1}} &= \frac{1}{4}\left(t_{\nu,\alpha} + t^{\dagger}_{\nu,\alpha} - i\epsilon_{\alpha\beta\gamma} t^{\dagger}_{\nu,\beta} t_{\nu,\gamma}\right)\left(t_{\alpha,i+1} + t^{\dagger}_{\nu+1,\alpha} - i\epsilon_{\alpha\beta\gamma} t^{\dagger}_{\nu+1,\beta} t_{\nu+1,\gamma}\right)\\
&= \frac{1}{4}\Big(t_{\nu,\alpha}t_{\nu+1,\alpha} + t^{\dagger}_{\nu,\alpha}t^{\dagger}_{\nu+1,\alpha} + t_{\nu,\alpha}t^{\dagger}_{\nu+1,\alpha} + t^{\dagger}_{\nu,\alpha}t_{\nu+1,\alpha} + t^{\dagger}_{\nu,\beta}t_{\nu,\gamma}t^{\dagger}_{\nu+1,\gamma}t_{\nu+1,\beta}\\
&- t^{\dagger}_{\nu,\beta}t_{\nu,\gamma}t^{\dagger}_{\nu+1,\beta}t_{\nu+1,\gamma} - i\epsilon_{\alpha\beta\gamma}\left(t^{\dagger}_{\nu,\beta}t_{\nu,\gamma}(t_{\nu+1,\alpha} + t^{\dagger}_{\nu+1,\alpha}) + (t_{\nu,\alpha} + t^{\dagger}_{\nu,\alpha})t^{\dagger}_{\nu+1,\beta}t_{\nu+1,\gamma}\right)\Big)
\end{aligned}
\tag{2.7}
$$

$$
\begin{aligned}
\boldsymbol{S_{\nu,2}} \cdot \boldsymbol{S_{\nu+1,2}} &= \frac{1}{4}\left(-t_{\nu,\alpha} - t^{\dagger}_{\nu,\alpha} - i\epsilon_{\alpha\beta\gamma} t^{\dagger}_{\nu,\beta} t_{\nu,\gamma}\right)\left(-t_{\nu+1,\alpha} - t^{\dagger}_{\nu+1,\alpha} - i\epsilon_{\alpha\beta\gamma} t^{\dagger}_{\nu+1,\beta} t_{\nu+1,\gamma}\right)\\
&= \frac{1}{4}\Big(t_{\nu,\alpha}t_{\nu+1,\alpha} + t^{\dagger}_{\nu,\alpha}t^{\dagger}_{\nu+1,\alpha} + t_{\nu,\alpha}t^{\dagger}_{\nu+1,\alpha} + t^{\dagger}_{\nu,\alpha}t_{\nu+1,\alpha} + t^{\dagger}_{\nu,\beta}t_{\nu,\gamma}t^{\dagger}_{\nu+1,\gamma}t_{\nu+1,\beta}\\
&- t^{\dagger}_{\nu,\beta}t_{\nu,\gamma}t^{\dagger}_{\nu+1,\beta}t_{\nu+1,\gamma} + i\epsilon_{\alpha\beta\gamma}\left(t^{\dagger}_{\nu,\beta}t_{\nu,\gamma}\left(t_{\nu+1,\alpha} + t^{\dagger}_{\nu+1,\alpha}\right) + \left(t_{\nu,\alpha} + t^{\dagger}_{\nu,\alpha}\right)t^{\dagger}_{\nu+1,\beta}t_{\nu+1,\gamma}\right)\Big)
\end{aligned}
\tag{2.8}
$$

Plugging equations (2.6), (2.7) and (2.8) into equation (2.1) it follows

$$
\begin{aligned}
\mathcal{H} = &\sum_{\nu,\alpha,\beta,\gamma}\Bigg(J^{\perp}_{\nu}\left(-\frac{3}{4} + t^{\dagger}_{\nu,\alpha}t_{\nu,\alpha}\right)\\
&+ \frac{1}{4}\left(J^{\|}_{\nu,1} + J^{\|}_{\nu,2}\right)(t_{\nu,\alpha}t_{\nu+1,\alpha} + t^{\dagger}_{\nu,\alpha}t^{\dagger}_{\nu+1,\alpha} + t_{\nu,\alpha}t^{\dagger}_{\nu+1,\alpha} + t^{\dagger}_{\nu,\alpha}t_{\nu+1,\alpha}\\
&+ t^{\dagger}_{\nu,\beta}t_{\nu,\gamma}t^{\dagger}_{\nu+1,\gamma}t_{\nu+1,\beta} - t^{\dagger}_{\nu,\beta}t_{\nu,\gamma}t^{\dagger}_{\nu+1,\beta}t_{\nu+1,\gamma})\\
&- \frac{1}{4}\left(J^{\|}_{\nu,1} - J^{\|}_{\nu,2}\right)i\epsilon_{\alpha\beta\gamma}\left(t^{\dagger}_{\nu,\beta}t_{\nu,\gamma}(t_{\nu+1,\alpha} + t^{\dagger}_{\nu+1,\alpha}) + (t_{\nu,\alpha} + t^{\dagger}_{\nu,\alpha})t^{\dagger}_{\nu+1,\beta}t_{\nu+1,\gamma}\right)\Bigg).
\end{aligned}
\tag{2.9}
$$

The term $\sum_{\nu} -\frac{3}{4}J^{\perp}_{\nu}$ is just a number and has no influence on the dynamics. Therefore in the following the operator $\bar{\mathcal{H}} = \mathcal{H} + \sum_{\nu}\frac{3}{4}J^{\perp}_{\nu}$ is regarded. One can decompose $\bar{\mathcal{H}}$ into

$$
\bar{\mathcal{H}} = \mathcal{H}_0 + T_0 + T_1 + T_{-1} + T_2 + T_{-2}
\tag{2.10}
$$

with

$$
\mathcal{H}_0 = \sum_{\nu,\alpha} J^{\perp}_{0}\; t^{\dagger}_{\nu,\alpha}t_{\nu,\alpha},
\tag{2.11}
$$

$$
\begin{aligned}
T_0 = &\sum_{\nu,\alpha,\beta,\gamma}\Bigg(\left(J^{\perp}_{\nu} \; - J^{\perp}_{0}\;\right)t^{\dagger}_{\nu,\alpha}t_{\nu,\alpha}\\
&+ \frac{1}{4}\left(J^{\|}_{\nu,1} + J^{\|}_{\nu,2}\right)\left(t_{\nu,\alpha}t^{\dagger}_{\nu+1,\alpha} + t^{\dagger}_{\nu,\alpha}t_{\nu+1,\alpha} + t^{\dagger}_{\nu,\beta}t_{\nu,\gamma}t^{\dagger}_{\nu+1,\gamma}t_{\nu+1,\beta} - t^{\dagger}_{\nu,\beta}t_{\nu,\gamma}t^{\dagger}_{\nu+1,\beta}t_{\nu+1,\gamma}\right)\Bigg),
\end{aligned}
\tag{2.12}
$$

$$T_1 = \sum_{\nu,\alpha,\beta,\gamma} -\frac{1}{4}\left(J^{\|}_{\nu,1} - J^{\|}_{\nu,2}\right) i\epsilon_{\alpha\beta\gamma}\left(t^{\dagger}_{\nu,\beta}t_{\nu,\gamma}t^{\dagger}_{\nu+1,\alpha} + t^{\dagger}_{\nu,\alpha}t^{\dagger}_{\nu+1,\beta}t_{\nu+1,\gamma}\right), \tag{2.13}$$

$$T_{-1} = \sum_{\nu,\alpha,\beta,\gamma} -\frac{1}{4}\left(J^{\|}_{\nu,1} - J^{\|}_{\nu,2}\right) i\epsilon_{\alpha\beta\gamma}\left(t^{\dagger}_{\nu,\beta}t_{\nu,\gamma}t_{\nu+1,\alpha} + t_{\nu,\alpha}t^{\dagger}_{\nu+1,\beta}t_{\nu+1,\gamma}\right), \tag{2.14}$$

$$T_2 = \sum_{\nu,\alpha} \frac{1}{4}\left(J^{\perp}_{\nu} - J^{\perp}_{0}\right) t^{\dagger}_{\nu,\alpha}t^{\dagger}_{\nu+1,\alpha} \tag{2.15}$$

and

$$T_{-2} = \sum_{\nu,\alpha} \frac{1}{4}\left(J^{\perp}_{\nu} - J^{\perp}_{0}\right) t_{\nu,\alpha}t_{\nu+1,\alpha}. \tag{2.16}$$

In the non-disordered case ($J^{\perp}_{\nu} = J^{\perp}$, $J^{\|}_{\nu} = J^{\|}$) the gap of the spin ladder, i.e. the energy difference between ground state and first excitation, is always finite. It approaches a value close to 0.4 for $J^{\|} \to \infty$. There is thus no phase transition for the spin ladder in the non-disordered case [19, 20].

2.2. Dimerized chain

The dimerized chain is a chain of spin-$1/2$ spins that are coupled by Heisenberg couplings. In the non-disordered case there are two different coupling strengths so that every spin is coupled differently to its left and right neighbour. In the isotropic case there is no difference in couplings anymore and the dimerized chain is just the Heisenberg chain. For the Heisenberg chain it is known that the spectrum is gapless and the excitations are spinons [21]. In the other extreme case one of the couplings is zero and the ground state is a product state of decoupled singlets the same way as in the strong-rung limit of the two-leg ladder. The latter has a spin gap. By increasing one of the couplings so that the isotropic case is reached the dimerized chain undergoes a QPT. The dimerized chain can also be viewed as a special case of the two-leg ladder with zero upper leg-coupling on the right of every odd and zero lower leg-coupling on the right of every even two-leg ladder supersite $\nu = \lfloor s/2 \rfloor$ with $\lfloor\ \rfloor$ being the Gaussian bracket (see Fig. 2.2).

$$\mathcal{H} = \sum_{\nu} J^{\perp}_{\nu}\, \boldsymbol{S_{\nu,1}} \cdot \boldsymbol{S_{\nu,2}} + \delta_{\nu,\text{even}}\, J^{\|}_{\nu,1}\, \boldsymbol{S_{\nu,1}} \cdot \boldsymbol{S_{\nu+1,1}} + \delta_{\nu,\text{odd}}\, J^{\|}_{\nu,2}\, \boldsymbol{S_{\nu,2}} \cdot \boldsymbol{S_{\nu+1,2}}. \tag{2.17}$$

As a consequence the dimerized chain Hamiltonian is given by the same terms in second quantization as the two-leg ladder with arbitrary couplings. The energies of the dimerized chain can thus be obtained by calculating the energies of the two-leg ladder with arbitrary couplings. In contrast to the ladder the chain is fully one-dimensional. The dimerized chain spins are labelled by s. It follows that a chain of $2N$ spins carries $2N$ momenta compared to the N momenta of the ladder.

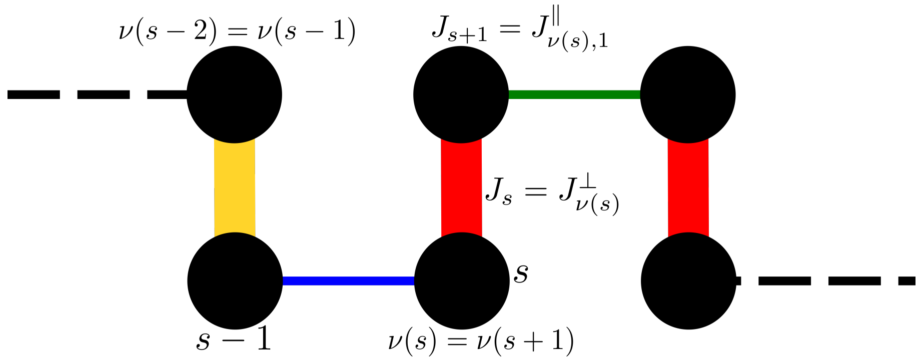

Fig. 2.2: The dimerized chain is shown as a special case of the two leg ladder with alternating either zero upper and lower leg couplings. Observables of the dimerized chain are labelled by the site labels s and not by the supersites ν anymore. The relation between those two is shown in the scheme. The rungs are equivalents to the dimers in the dimerized chain and are plotted thicker since their coupling strength should be significantly bigger than that of the leg couplings. Different colours mean different strengths of the couplings. This picture thus shows a realization of bimodal disorder.

2.3. Dynamic structure factor

Inelastic neutron scattering (INS) measures the dynamic structure factor. The systems reaction to the scattering can be calculated in a very good approximation by linear response theory. One useful form for the dynamic structure factor that shows the intensities measured in an experiment is then given by

$$\mathcal{S}(k,\omega) = -\frac{1}{\pi}\,\mathrm{Im}\left[\langle 0|\,\widetilde{S}^{\dagger}_{k,mz}\frac{1}{\omega-(\mathcal{H}-E_0)+i0^{+}}\widetilde{S}_{k,\mathrm{m}'z}\,|0\rangle\right] \tag{2.18}$$

for the ladder and

$$\mathcal{S}(k,\omega) = -\frac{1}{\pi}\,\mathrm{Im}\left[\langle 0|\,\widetilde{S}^{\dagger}_{k,z}\frac{1}{\omega-(\mathcal{H}-E_0)+i0^{+}}\widetilde{S}_{k,z}\,|0\rangle\right] \tag{2.19}$$

for the dimerized chain. For both $i0^{+}$ encodes that the Green's function is retarded, i.e. $t=0$ is the time when the neutrons starts scattering with the material and only times $t>0$ contribute. The structure factor is calculated by ground state averages because temperature $T=0$ is assumed. The tilde above the observables shall emphasize that observable and ground state have to act upon in the same basis.
$S_{k,m\alpha} = N^{-\frac{1}{2}}\sum_{\nu}\exp^{-i\nu k}S_{\nu,m\alpha}$ is a Fourier transformed spin observable that now carries the momentum k for the ladder. For the chain $S_{k,\alpha} = N^{-\frac{1}{2}}\sum_{s}\exp^{-isk}S_{s,\alpha}$ runs over all spins labelled by s. The momentum k is transferred between neutron and system during the scattering as well as the energy ω.

Because of $SU(2)$-invariance of both systems $\alpha = z$ w.l.o.g. There are no correlations between different α.
The two-leg ladder is only a quasi one-dimensional system. Thus $m = 1, 2$, i.e. correlations between upper and lower spins contribute. Easiest way to cover different combinations between m and m' is to go over to an antisymmetric

$$S_{k,1z} - S_{k,2z} \tag{2.20}$$

and symmetric

$$S_{k,1z} + S_{k,2z} \tag{2.21}$$

combination of both. These two different observables can be separated and extracted in the INS of pure ladder materials because the momentum transverse to the ladder direction that belongs to the antisymmetric observable is π and that of the symmetric observable is 0. Both together contain all possible INS information of ladder properties.
Later on quasi-particles called triplons will be introduced in the formalism of perturbative continuous unitary transformations. For the non-disordered ladder one important property is that the antisymmetric observable only shows weight in the triplon channels of odd particle number and the symmetric observable only for even triplon numbers. This is due to the fact that the non-disordered ladder is invariant under an exchange of upper and lower leg couplings. The property can be proven as follows. Let us denote the operator that does this exchange by P. For a state $|m\rangle$ with m triplets $P\,|m\rangle = (-1)^m\,|m\rangle$ and the same is true for triplons because the continuous unitary transformation described later preserves this parity [22, 23]. The antisymmetric spin observable can in principle inject any number of particles when acting on the vacuum and by symmetry its commutator with P is -1:

$$P\left(\tilde{S}_{\nu,1z} - \tilde{S}_{\nu,2z}\right)|0\rangle = P\sum_{m=1}^{\infty}|m\rangle = \sum_{m=1}^{\infty}(-1)^m\,|m\rangle = (-1)\sum_{m=1}^{\infty}|m\rangle \tag{2.22}$$

It follows that the antisymmetric observable can only inject odd numbers of triplons and in analogous way that the symmetric observable can only inject even numbers of triplons in the non-disordered case [22, 23]. For simplicity here only $|m\rangle$ was written for all states of a fixed number of triplons that the observable injects. An important consequence of some sorts of disorder is that this symmetry can be broken and weight of two triplons can e.g. contribute to the antisymmetric observable and that on the other hand the one triplon channel can show weight in the symmetric observable. For the non-disordered ladder most of the weight stays in the one triplon channel up to high values of the leg couplings. For $J^{\|}/J^{\perp} = 1$ still $\approx 74\%$ of the weight is contained in it and $\approx 20\%$ are in the two triplon channel [23]. For the symmetric observable it can be remarked that its weight at $k = 0$ is always zero. The symmetric observable at $k = 0$ is a sum over all spins. The unperturbed Hamiltonian commutes with $S_{\nu,1z} + S_{\nu,2z}$ due to an odd parity with respect to the mirror symmetry of the local rung spin product $\boldsymbol{S_{\nu,1}} \cdot \boldsymbol{S_{\nu,2}}$. For $k = 0$ this remains true for the leg spin products and the observable $S_{0,1z} + S_{0,2z}$. This observable thus commutes with the Hamiltonian and has zero weight. The situation for the dimerized chain is completely analogous so that the intensity of the dynamic structure factor is always zero at momentum $k = 0$.

The elementary excitations of the isotropic chain are gapless and can be modelled as spinons. The quasi-particle picture used for the dimerized chain is essentially the same as for the ladder. Since smaller gaps make it easier to excite higher particle number channels one expects the dimerized chain to behave differently than the ladder. Surprisingly for the isotropic chain still $> 99\%$ of the weight is in the two particle channel [23]. For $J^{\|}/J^{\perp} = 0.5$ there is still more than 80% of the weight in the one particle channel [23].
For the disordered case one is interested in the averaged dynamic structure factor $\langle \mathcal{S}(k,\omega) \rangle_{\mathrm{av}}$ which is defined as the mean of the dynamic structure factor over all disorder configurations:

$$\langle \mathcal{S}(k,\omega)_{\mathrm{av}} \rangle = \int dP(\{J_\nu\}) \mathcal{S}(k,\omega,\{J_\nu\}) \tag{2.23}$$

For several non-energy resolved quantities such means are given in the thermodynamic limit in appendix D. The energy-resolved average structure factor will be calculated in the results chapter for different probability distributions of the rung and leg couplings.

2.4. Leading-order effects

The starting point for perturbation theory is an unperturbed Hamiltonian of isolated rungs. The ground state consists of a condensate of singlet states and the first excitation is a local triplet on an arbitrary supersite ν denoted by $|\nu\rangle$. It follows that the energy corresponding to the first excitation has a degeneracy of the number of rungs. Taking the leg and rung coupling fluctuations as small perturbations first order degenerate perturbation theory leads to the following Hamiltonian for the one triplon sector:

$$\mathcal{H}^{\mathrm{order}=1}_{\nu',\nu} = \delta_{\nu,\nu'} J^{\perp}_{\nu} + \frac{1}{4}\left(\delta_{\nu+1,\nu'}(J^{\|}_{\nu,1} + J^{\|}_{\nu,2}) + \delta_{\nu-1,\nu'}(J^{\|}_{\nu-1,1} + J^{\|}_{\nu-1,2})\right) \tag{2.24}$$

For the dimerized chain this will be analogous with only difference that $J^{\|}_{\nu,1}$ is zero for every even supersite and vice versa $J^{\|}_{\nu,2}$ for every odd.
In the absence of disorder - $J^{\perp}_{\nu} = J^{\perp}$ - the momentum states

$$|k\rangle = \frac{1}{\sqrt{N}} \sum_{\nu} e^{-i\nu k} |\nu\rangle \tag{2.25}$$

are eigenstates and we obtain the dispersion relation

$$w(k) = J^{\perp} + J^{\|} \cos(k). \tag{2.26}$$

Effects due to disorder shall be discussed in the following section.

2.4.1. Localization

It was Anderson who first showed for the Anderson model that every eigenstate is localised in one dimension [5]. The Anderson model equals Hamiltonian (2.24) with uniform rung disorder which can be viewed as a free particle in a disordered potential. Quite general one particle Hamiltonians with disorder can be expressed as a matrix in one dimension. If the interaction between the particles has finite range the matrix is a random banded matrix. This band structure incorporates the geometry of the lattice. One dimensional physical systems with short-ranged interactions almost always have localised states in the presence of disorder [8, 1]. In [24] it is shown with transfer matrix methods that the states in the middle of the band remain extended in most cases of purely super- and subdiagonal disorder. However the amount of those extended states is so small that they have no statistical significance [8, 1]. In the case of only rung disorder it is relatively simple to show localization for a Hamiltonian as in equation (2.24) by using transfer matrix methods [25]. It can be shown that the components of the wavefunction undergo an exponential growth when a semi-infinite chain is regarded. The rate of growth can be related to the localization length in an infinite system. A non-rigorous argument for that is that one can build a wavefunction for a large finite system by superposing two wavefunctions of the semi-infinite systems, one with the open boundaries on the right and one on the left. If the two wavefunctions lie close in energy they can match at the maximum of the resulting wavefunction. For a sufficiently large system the resulting state will be exponentially localised. Being only dependent on a limited finite region of the lattice this eigenstate will remain to be an eigenstate also of the infinite lattice [1]. The study of localization induced by off-diagonal disorder like the hopping term in equation (2.24) is more difficult. However, there exist quite rigorous results. The power-law random banded matrix model is defined by matrices with centred Gaussian entries and covariance structure

$$\left\langle |H_{x,y}|^2 \right\rangle = \left(1 + \left(\frac{|x-y|}{b}\right)^{2\alpha}\right)^{-1}. \tag{2.27}$$

For $\alpha > 1$ the system is in the localized regime. It undergoes an Anderson transition at $\alpha = 1$. The parameter b hereby characterizes the behaviour at the critical point. This model can be identified with a random long-range hopping Hamiltonian whose hopping amplitudes decay as $|x-y|^{-\alpha}$ [7].

It can be concluded that localization is expected not only for the leading-order Hamiltonian but for all disordered one dimensional systems with sufficiently weak long-range interactions. For the quantities at interest, namely the dynamic structure factor that is measured in an inelastic neutron scattering experiment, it will be of importance how disorder changes the shape of eigenfunctions in momentum space. The most important observable for the INS of the two-leg ladder is $\frac{1}{\sqrt{N}} \sum_\nu e^{-i\nu k} \left(\boldsymbol{S_{\nu,1z}} - \boldsymbol{S_{\nu,2z}}\right) = t_k + t_k^\dagger$. In zeroth order this observable measures the projection of an energy eigenstate on its momentum components. Generally eigenfunctions will get wider and wider distributed in momentum space as the localization length decreases. For small disorder however, e.g. an eigenfunction that has substantial weight on more than thousand rungs, the width measured by a neutron scattering experiment will not be very different from the resolution of the apparatus. Thus localization alone is not important for the neutron scattering response. It is crucial what value the localization length takes and how the shapes of the eigenfunctions change in momentum space.

2.4.2. Self-energy calculations

We want to start discussing small disorder effects as a perturbation of the momentum eigenstates. For that the Hamiltonian has to be transformed in its momentum representation.

$$\begin{aligned}\mathcal{H}^{\text{order}=1}_{k',k} =& \frac{1}{N}\left\langle \sum_{\nu'} e^{-i\nu' k'}\left|\nu'\right\rangle \middle| \mathcal{H}^{\text{order}=1} \middle| \sum_{\nu} e^{-i\nu k}\left|\nu\right\rangle \right\rangle \\ =& \frac{1}{N}\delta_{k,k'}\sum_{\nu}\left(J^{\perp}_{\nu} + \frac{1}{2}(J^{\|}_{\nu,1} + J^{\|}_{\nu,2})\cos(k)\right) \\ &+ \frac{1}{N}(1-\delta_{k,k'})\sum_{\nu} e^{i\nu(-k+k')}\left(J^{\perp}_{\nu} + \frac{1}{4}(e^{ik'} + e^{-ik})(J^{\|}_{\nu,1} + J^{\|}_{\nu,2})\right).\end{aligned} \tag{2.28}$$

The non-diagonal terms only vanish in the non-disordered case because disorder breaks translational symmetry. In the thermodynamic limit the diagonal terms are just the mean values of the hopping elements (in the following also denoted by mean band)

$$\mathcal{H}^{\text{order}=1}_{k,k} = \left\langle J^{\perp}_{\nu}\right\rangle + \frac{1}{2}\left\langle J^{\|}_{\nu,1} + J^{\|}_{\nu,2}\right\rangle\cos(k) =: \overline{w}(k). \tag{2.29}$$

This motivates the use of

$$G^{0+}_{0}(k,w) = \frac{1}{w - \overline{w}(k) + i0^{+}} \tag{2.30}$$

as unperturbed retarded Green's function. Treating the non-diagonal terms (and the fluctuation on the diagonal) as perturbation $V(k,k')$ the new Green's function has to fulfil the relation

$$G^{0+}(k,w) = G^{0+}_{0}(k,w) + \int G^{0+}(k',w)V(k',k)G^{0+}_{0}(k,w)dk'. \tag{2.31}$$

Only a resummation of infinitely many terms can lead to a change in the pole structure of $G^{0+}(k,w)$. A quantity that contains the effect of a summation of infinitely many terms is the self-energy $\Sigma(k,w)$. It relates the perturbed and unperturbed Green's function by

$$G^{0+}(k,w) = \frac{1}{w - \Sigma(k,w) - \overline{w}(k) + i0^{+}} \tag{2.32}$$

and is given by Dyson's equation

$$G^{0+}(k,w) = G^{0+}_{0}(k,w) + \int G^{0+}_{0}(k,w)\Sigma(k,w)G^{0+}(k',w)dk'. \tag{2.33}$$

In first-order Born approximation it is

$$\begin{aligned}\Sigma(k,w)_{\text{Born}} &= \int V(k,k')G_0^{0+}(k',w)V(k',k)dk' \approx \int \left\langle |V(k,k'|^2 \right\rangle G_0^{0+}(k',w)dk' \\ &=: \overline{\Sigma}(k,w)_{\text{Born}}.\end{aligned} \tag{2.34}$$

The idea to treat disorder by self-energy calculations was inspired by the Diplomarbeit of Christian Harrer about matter waves in disordered media [26]. If one assumes $J^{||}_{\nu,1}$, $J^{||}_{\nu,2}$ and $J^{\perp}_{\nu}$ to be stochastically independent and $J^{||}_{\nu,1}, J^{||}_{\nu,2}$ to be identically distributed one obtains using the Wiener-Khinchin theorem

$$\left\langle |V(k,k'|^2 \right\rangle = \frac{1}{N^2} N \left(\operatorname{Var}(J^{\perp}_{\nu}) + \frac{1}{4}\left(1+\cos(k+k')\right) \operatorname{Var}(J^{||}_{\nu}) \right). \tag{2.35}$$

A generalization for correlated disorder and higher orders of the perturbation theory is given in Appendix B. Disorder on the rungs does not show any k-dependence in first order reflecting its local character. This non-dispersive behaviour is linked to stronger localization effects of rung disorder as will be seen later. With (2.35) and by letting N go to infinity the self-energy can be written as

$$\overline{\Sigma}(k,w)_{\text{Born}} = \frac{1}{2\pi}\int_0^{2\pi} \frac{\operatorname{Var}(J^{\perp}_{\nu}) + \frac{1}{4}\left(1+\cos(k+k')\right)\operatorname{Var}(J^{||}_{\nu})}{w - \langle J^{\perp}_{\nu}\rangle - \left\langle J^{||}_{\nu}\right\rangle \cos(k') + i0^+} dk'. \tag{2.36}$$

The Dirac identity $\frac{1}{x+i0^+} = \mathcal{P}(1/x) - i\pi\delta(x)$ yields for the imaginary part

$$\begin{aligned}\operatorname{Im}(\overline{\Sigma}(k,w)_{\text{Born}}) =& -\frac{1}{2}\int_0^{2\pi} \delta\left(w - \left\langle J^{\perp}_{\nu}\right\rangle - \left\langle J^{||}_{\nu}\right\rangle \cos(k')\right) \\ &\left(\operatorname{Var}(J^{\perp}_{\nu}) + \frac{1}{4}\left(1+\cos(k+k')\right)\operatorname{Var}(J^{||}_{\nu})\right) dk' \\ =& -\Theta\left(\left\langle J^{||}_{\nu}\right\rangle - \left|w - \left\langle J^{\perp}_{\nu}\right\rangle\right|\right)\left(\frac{1}{\left\langle J^{||}_{\nu}\right\rangle}\frac{1}{\sqrt{1-\left(\frac{w-\left\langle J^{\perp}_{\nu}\right\rangle}{\left\langle J^{||}_{\nu}\right\rangle}\right)^2}}\operatorname{Var}(J^{\perp}_{\nu})\right. \\ &\left. -\frac{\operatorname{Var}(J^{||}_{\nu})}{4\left\langle J^{||}_{\nu}\right\rangle}\left(\frac{1}{\sqrt{1-\left(\frac{w-\left\langle J^{\perp}_{\nu}\right\rangle}{\left\langle J^{||}_{\nu}\right\rangle}\right)^2}} + \cos(k)\,\frac{w-\left\langle J^{\perp}_{\nu}\right\rangle}{\sqrt{\left\langle J^{||}_{\nu}\right\rangle^2 - \left(w-\langle J^{\perp}_{\nu}\rangle\right)^2}}\right)\right).\end{aligned} \tag{2.37}$$

The broadening due to rung disorder is solely depending on energy. In contrast to that, leg disorder also shows a strong dependence on k. For states in the middle of the band, $k = \frac{\pi}{2}$, the broadening is zero in agreement with [24]. For both sorts of disorder the imaginary part

of the self-energy grows towards the band edges and is diverging there. Inside the band the cosine term damps the broadening in the leg disorder case, so that it can be several orders of magnitude smaller than with comparable rung disorder strength.
The absence of an imaginary part outside the interval of the mean dispersion is unphysical and caused by the Born approximation.
The principal value of equation (2.36) is zero for rung disorder and $-\left(\mathrm{Var}\left(J_\nu^{\|}\right)/4\left\langle J_\nu^{\|}\right\rangle\right)\cos(k)$ for leg disorder. Thus

$$\mathrm{Re}(\overline{\Sigma}(k,w)) = -\frac{\mathrm{Var}(J_\nu^{\|})}{4\left\langle J_\nu^{\|}\right\rangle}\cos(k). \tag{2.38}$$

In the rung disorder case even the self-consistent Born approximation can be calculated. One obtains

$$\begin{aligned}\overline{\Sigma}(k,\omega) =& \frac{1}{2\pi}\int_0^{2\pi}\frac{\mathrm{Var}(J_\nu^{\perp})}{w-\langle J_\nu^{\perp}\rangle-\left\langle J_\nu^{\|}\right\rangle\cos(k')-\Sigma(k,\omega)+i0^+}dk' \\ =& \frac{-i\mathrm{Var}(J_\nu^{\perp})}{\sqrt{\left\langle J_\nu^{\|}\right\rangle^2-\left(\langle J_\nu^{\perp}\rangle-\omega+\overline{\Sigma}(k,\omega)\right)^2}}.\end{aligned} \tag{2.39}$$

The self-consistent equation allows to calculate the self-energy outside the mean dispersion range. It is compared with numerical data in Fig. 2.3. One sees that the broadening is also strongest at the band edges when dealing with rung disorder only. For energies in the middle of the band the self-consistent curve and the numerically obtained one in Fig. 2.3 fit well. For $k=\pi$ the self-consistent ansatz starts to deviate. There is an exponential tail in the numerical calculations which can not be reproduced with the self-consistent ansatz.
One underlying assumption for all these calculations is that the matrix elements of the Hamiltonian in the momentum basis are stochastically independent. While for all kinds of disorder the matrix elements are marginally Gaussian due to the central limit theorem and uncorrelated by the Karhunen-Loeve theorem only in the case of Gaussian disorder they are stochastically independent. Interference effects between stochastically dependent matrix elements in equation (2.33) give contributions of higher moments of the disorder distribution to the self-energy. E.g. the sum of the first column is fixed by the first entry of the hopping element sequences and thus can only take two values for bimodal disorder. The error due to this simplification is biggest at the band edges. In Fig. 2.4, where bimodal disorder was compared with the self-consistent ansatz, the agreement in the middle of the band is still satisfying while at the edges there is no similarity anymore. As an example for the contribution of higher moments a non-vanishing skewness of the distribution can have substantial effects. This can be seen in Fig. 2.5 for $k=\pi/2$. Asymmetric bimodal configurations with same mean and variance were compared with the self-consistent ansatz. The non-vanishing skewness of the distribution leads to first differences between the self-consistent and the $p=0.6$ case such that the orange curve is not symmetric anymore in Fig. 2.5. The increase from $p=0.6$ to $p=0.8$ of course leads to even stronger dependencies on the odd moments of the probability distribution. The peak shifts to higher energies and its intensity increases.

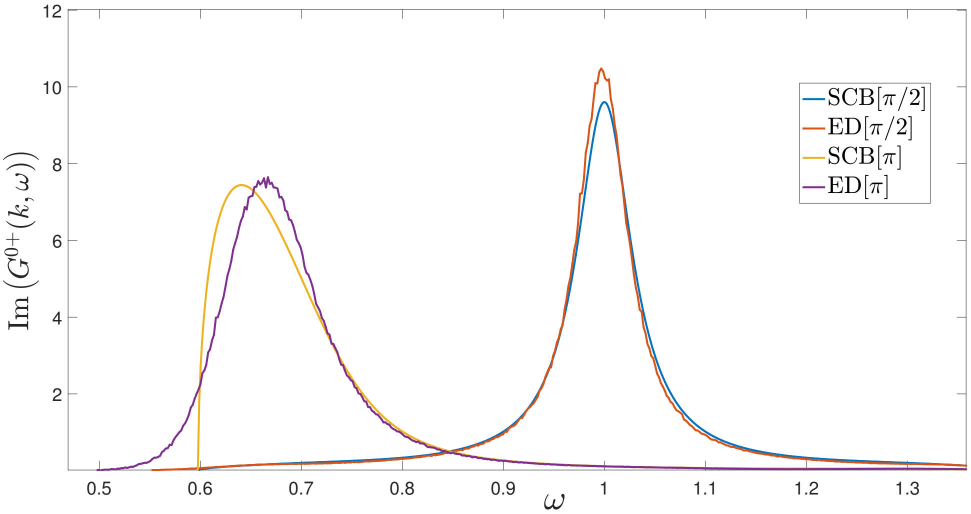

Fig. 2.3: Left curves (yellow and violet) show the imaginary part of the Green's function for $k = \pi$. The yellow curve was obtained by the self-consistent Born approximation (SCB) whereas the violet curve was obtained by exact diagonalizations of a 200-supersite system with Gaussian rung disorder and averaging of 1000 energy bins over 20000 samples (ED). In both cases the disorder strength was $\mathrm{Var}(J_\nu^\perp) = 0.1^2$ and $J_\| = 0.3$, $\left\langle J_\nu^\perp \right\rangle = 1$.

Still, the magnitude of the mean absolute square of the entries can give important insight in the behaviour of the system and the ansatz used here can be a good approximation for small enough disorder.

With stronger and stronger disorder the eigenstates usually get more and more localized. For bimodal disorder the density of states (DOS) can become non-smooth showing many peaks. This does not happen for Gaussian disorder and can also not be predicted with the self-energy methods described so far. By using conventional perturbation theory in position space we can qualitatively describe those findings.

2.4.3. Position space arguments

An upper (lower) bound for the energy is given by the maximum (minimum) value on the diagonal plus (minus) two times the maximum absolute value of the superdiagonal. This can be shown with Gerschgorin's circle theorem. These upper and lower bounds are reached when the system size N approaches infinity. Then there will be bigger and bigger finite chain segments within the infinite chain that are build of these maximum (minimum) values. However the possibility for such a finite chain to occur decreases exponentially with its length. E.g. for bimodal disorder only and probability p for value a the mean amount of finite chains with n consecutive a values on the diagonal is $N(1-p)^2p^n$.

We want to consider the situation of bimodal rung disorder only in first order degenerate perturbation theory to learn more about the DOS. $J_\nu^\perp$ now takes two values a and b with probabilities p and $1-p$ respectively and $J_\nu^\| = J^\| << a, b$. The Hamiltonian is of size N so that

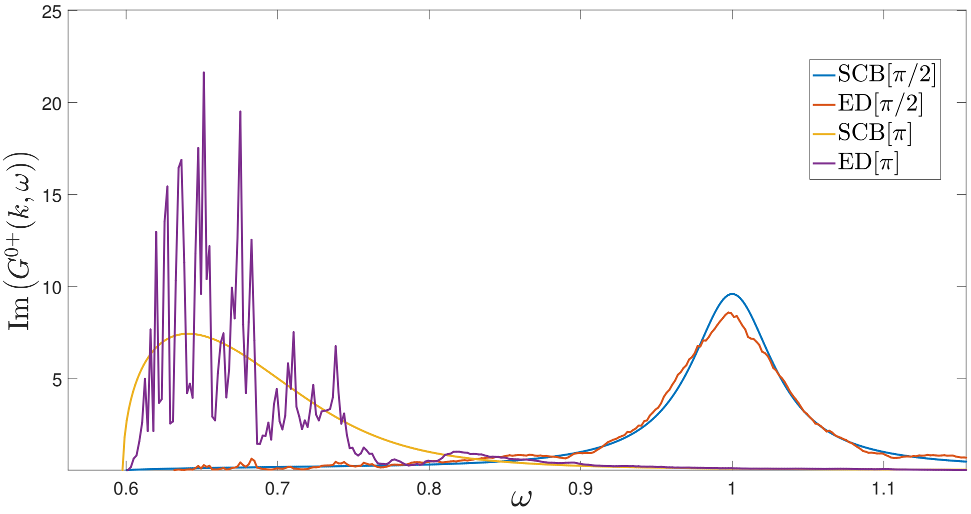

Fig. 2.4: Left curves (yellow and violet) show the imaginary part of the Green's function for $k = \pi$. The yellow curve was obtained by the self-consistent born equation (SCB) whereas the violet curve was obtained by exact diagonalizations (ED) of a 200-supersite system with bimodal rung disorder and averaging of 1000 energy bins over 20000 samples. In both cases the disorder strength was $\mathrm{Var}(J_\nu^\perp) = 0.1^2$ and $J_\parallel = 0.3$, $\left\langle J_\nu^\perp \right\rangle = 1$. The rung couplings took values of 1.1 respectively 0.9 with probability 0.5 each.
Right curves (red and blue) are for $k = \frac{\pi}{2}$. The deviation of both curves is bigger than in the Gaussian disorder case but still small. The big difference between $k = \pi$ and $k = \frac{\pi}{2}$ is remarkable.

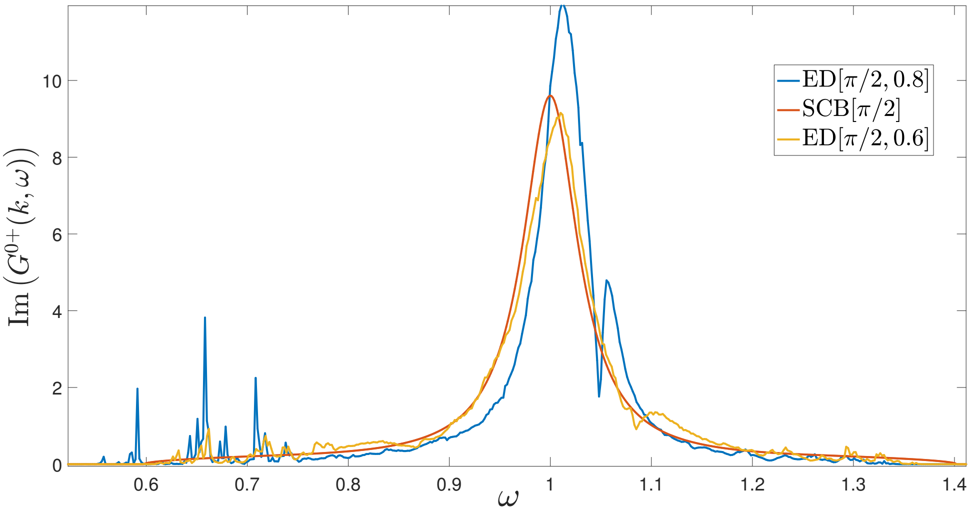

Fig. 2.5: All curves show rung disorder with strength $\mathrm{Var}(J_\nu^\perp) = 0.1^2$, $J_\parallel = 0.3$, $\left\langle J_\nu^\perp \right\rangle = 1$ at $k = \pi/2$. The yellow and blue curves were obtained by exact diagonalizations of a 200-supersite system with bimodal rung disorder and averaging of 1000 energy bins over 20000 samples. In the yellow case (ED[$\pi/2, 0.6$]) the probability for the bigger of the two rung couplings was 0.6, in the blue case (ED[$\pi/2, 0.8$]) 0.8. The red curve was obtained by the self-consistent Born approximation.

the mean amount of a-values is Np and of b-values is $N(1-p)$. The subset I_a of the position basis contains the basis vectors $|\nu\rangle$ for which $\mathcal{H}_{ii} = a$ and I_b in an analogous manner for b. First step in the degenerate perturbation theory is to diagonalize the matrices $\mathcal{H}^{a,b}_{i,j} = \langle i| \mathcal{H} |j\rangle$ with $|i\rangle, |j\rangle \in I_{a,b}$. W.l.o.g. consider the a-case. The matrix $\mathcal{H}^{a}_{i,j}$ is a symmetric tridiagonal matrix with a on the diagonal and $J^{\|}$ or 0 on the off-diagonal. Whenever an a on the diagonal of the original Hamiltonian is neighboured by two b's, let us say at supersite ν, $\mathcal{H}^a$ has $|\nu\rangle$ as eigenvector with eigenvalue a. Furthermore the matrix is block diagonal at that place. More generally the matrix $\mathcal{H}^a$ splits into blocks belonging to connected sequences of a on the diagonal of $\mathcal{H}$. The mean amount of blocks with size n will be $N(1-p)^2p^n$. Its eigenvalues and eigenvectors can be given explicitly as those of symmetric tridiagonal Toeplitz matrices and can be viewed as those of a finite chain with open boundary conditions. They are

$$\lambda_k = a + J^{\|} \cos\left(\frac{\pi k}{n+1}\right) \tag{2.40}$$

and

$$\boldsymbol{v_k}^T = \left(\sin\left(\frac{1\pi k}{n+1}\right), ..., \sin\left(\frac{n\pi k}{n+1}\right)\right) \tag{2.41}$$

with $k = 1, .., n$. These eigenfunctions are the eigenfunctions of zeroth order for the degenerate perturbation problem and the corresponding energies are of first order. The so calculated DOS shows many discrete peaks rather than a continuous curve. In Fig. 2.6 and Fig. 2.7 this calculation is compared with a numerically obtained DOS for a rung disorder of $P(J^{\perp}_{\nu} = 1.5) = 0.7$, $P(J^{\perp}_{\nu} = 0.5) = 0.3$ and $J^{\|}_{\nu} = 0.1$. Qualitatively they show the same

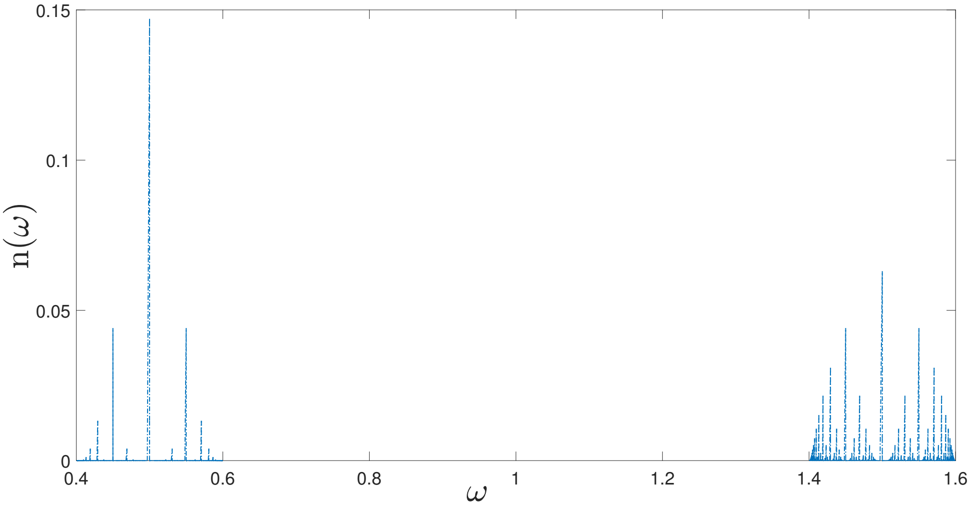

Fig. 2.6: The figure shows the percentage of states with energy ω one obtains with a first-order degenerate perturbation theory calculation for rung disorder of $P(J^{\perp}_{\nu} = 1.5) = 0.7$, $P(J^{\perp}_{\nu} = 0.5) = 0.3$ and $J^{\|} = 0.1$.

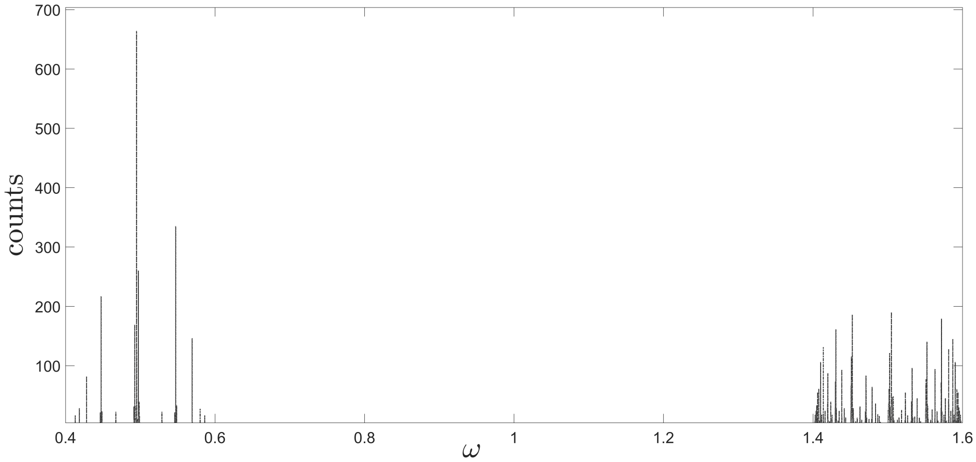

Fig. 2.7: One can see a histogram of 5000 bins obtained by numerically diagonalizing a 10000-rung chain for rung disorder of $P(J_\nu^\perp = 1.5) = 0.7$, $P(J_\nu^\perp = 0.5) = 0.3$ and $J^{||} = 0.1$. The histogram shows qualitatively the same features as the DOS obtained by first-order degenerate perturbation theory.

features leading us to conclude that the argument of a splitting into finite segments is an important aspect of bimodal rung disorder. In Fig. 2.8 also the eigenfunctions belonging to a finite chain of four 0.5 values on the diagonal were compared for the same disorder showing good quantitative agreement. This is not surprising since the error of the perturbative calculation is smallest for long segments (the probability for four consecutive 0.5 values is approximately 0.4%).

For sufficiently large rung disorder there appear bandgaps in the DOS (see also Fig. 2.7). Gerschgorin's circle theorem predicts that this has to occur in the presence of bimodal rung disorder and arbitrary leg couplings if

$$\max(J_\nu^\perp) - \max(J_\nu^{||}) > \min(J_\nu^\perp) + \max(J_\nu^{||}) \tag{2.42}$$

holds. This can be generalized for banded matrices with bandwidth bigger than one. This condition is not necessary but sufficient and if fulfilled there will also be exactly a percentage of p states above and $1-p$ states below the gap with p the probability for $\max(J_\nu^\perp)$ and $N \to \infty$. Gerschgorin's circle theorem suggests that only rung disorder leads to such bandgaps. In [1] it is shown for bimodal rung disorder and fixed leg couplings that the condition

$$\max(J_\nu^\perp) > \min(J_\nu^\perp) + J^{||} \tag{2.43}$$

is already enough to predict that $\frac{1-p}{2-p}$ states will have energy less than $\min(J_\nu^\perp)$. It can also be shown as $\max(J_\nu^\perp)$ gets bigger while $\min(J_\nu^\perp)$ remains fixed there will be more and more energies below $\min(J_\nu^\perp)$ with vanishing DOS [27]. This is a further agreement to the prediction that the DOS will show many peaks and be non-smooth.

In the case of weak bimodal leg disorder only we do not have strong localization in between the mean band. The eigenvectors of the maximum (minimum) energies lying outside the mean

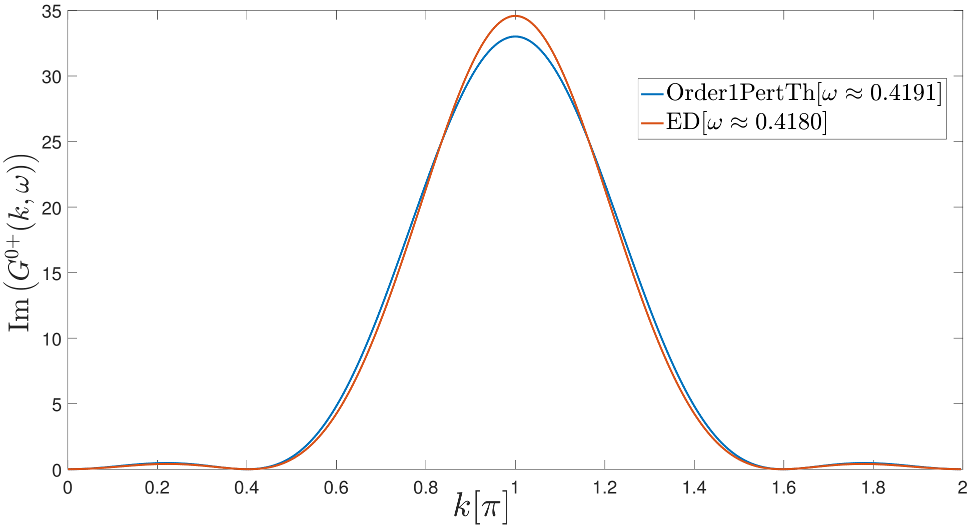

Fig. 2.8: The red curve was obtained by 8000 numerical diagonalizations of 500 rungs with 5000 bins and rung disorder of $P(J^{\perp}_{\nu} = 1.5) = 0.7$, $P(J^{\perp}_{\nu} = 0.5) = 0.3$ and $J^{\parallel} = 0.1$. The energy (0.4180) was chosen as the one closest to the energy obtained by first-order degenerate perturbation theory for a chain of four 0.5-rungs (0.4191).

band however have most of their weight on consecutive finite chains with only the maximum value of the leg disorder. Because of the exponentially decreasing probability with length for such a chain to occur we will see discrete peaks of the DOS. Each peak can be assigned to a certain length of these chains and the weight of the peak will get smaller the longer the length becomes. The eigenvectors will be much stronger localized than in the mean band. The longer these finite chains are the more the eigenvectors will become like plane waves on the finite chain and zeros outside. The error of a variational ansatz that chooses the eigenfunction to be just ones on the finite chain and zero elsewhere to the upper bound of Gerschgorin's theorem is given by $\max(J^{\parallel}_{\nu})/n$.

In the extreme case of values 0 and c for the leg disorder the infinite chain would split into finite chains and we have the same situation as in the first-order degenerate calculation for the bimodal rung disorder. We therefore will have a non-smooth DOS with many peaks in that situation. We expect the DOS to interpolate between discrete and smooth as 0 approaches c. There can also be a DOS that is partially smooth and partially consisting of many discrete peaks.

The shape of the DOS and the degree of localization depend highly on the sort of disorder. While all states are localized there can be big differences in the localization length. Leg disorder generally shows weaker and more energy dependent localization effects than rung disorder when the disorder strength is comparable. Bimodal disorder can lead to a DOS consisting of many discrete peaks without any smooth structure.

2.5. Inverse participation ratio

The inverse participation ratio (IPR)

$$IPR = \sum_{\nu} |\langle n|\nu\rangle|^4 \tag{2.44}$$

with $|\nu\rangle$ position states is a simple and intuitive measure for the localization length of a normalized eigenfunction $|n\rangle$. Suppose $|n\rangle$ is a plane wave eigenstate of a periodic one-dimensional chain with one atom in the unit cell. Then the IPR will be $1/N$, N being the length of the chain. For all other extended states the IPR will be bigger but always remain $\propto 1/N$ [1, 12, 7]. For a perfectly localized eigenstate - $|n\rangle = |\nu\rangle$ - the value of the IPR is just one. An exponentially localized state

$$|\langle n|\nu\rangle|^2 \propto \exp\left(-\frac{|\nu-\nu_0|}{\xi}\right) \tag{2.45}$$

has an IPR of

$$\frac{\sum_\nu \exp\left(-2\frac{|\nu-\nu_0|}{\xi}\right)}{\left(\sum_\nu \exp\left(-\frac{|\nu-\nu_0|}{\xi}\right)\right)^2} = \frac{2\,\frac{1}{1-\exp\left(-\frac{2}{\xi}\right)}-1}{\left(2\,\frac{1}{1-\exp\left(-\frac{1}{\xi}\right)}-1\right)^2} \approx \frac{\xi-1}{(2\xi-1)^2} \approx \frac{1}{4\xi}. \tag{2.46}$$

The approximation used hereby is already quite good for localization lengths ξ bigger than 2. The IPR ranges between 1 for a perfectly localized state and 0 for extended states as the system size $N \to \infty$. For values in between the localization length can be estimated as $\xi \approx {}^{1}/_{(4IPR)}$ assuming they have an exponentially localized shape. For localized states of different shape the scaling with the IPR will be different but again the IPR will be bigger if the states are more localized.

For two particles position states $|\nu, \nu+\delta\rangle$ and their corresponding eigenfunctions $|n\rangle$ in position space we propose an analogous quantity to the IPR denoted by IPR_2:

$$IPR_2 = \sum_{\nu,\delta} |\langle n|\nu, \nu+\delta\rangle|^4 \tag{2.47}$$

Clearly this quantity goes to zero with system size for extended states as well and only remains finite if the eigenfunctions are localized on a finite subset of two-particle position states.

3. pCUT approach

3.1. Continuous unitary transformations

The number of states of finite two-leg ladders or dimerized chains rises exponentially with system size. Hence only small systems can be diagonalized exactly to find the energies and eigenstates of such systems. Problems are a limited momentum resolution and depending on the system huge finite-size effects. Often only the low-lying excitations of a system are of interest. They are the most important states for low temperatures and enough to describe the phase behaviour of the system at $T = 0$. Methods that truncate at some energy but still describe the energies below accurately are thus looked for. One method that even goes beyond that is a continuous unitary transformation (CUT). It does not truncate the Hilbert space but preserves it during the transformation. The method can be used to obtain a Hamiltonian that is block-diagonal in the number of quasi-particles. One condition for this is that the unperturbed Hamiltonian had a similar block-diagonal structure. The perturbation introduces interactions between blocks of different particle numbers. With the CUT these interactions can be eliminated again as illustrated in Fig. 3.1. The so obtained new quasi-particles interact differently depending on the strength of the perturbation. Because each particle number channel is independent of the others, the problem of an exponentially increasing Hilbert space is solved. For most problems in the end a truncation is done in the quasi-particle block of interest. Other quasi-particle blocks are not affected by it. The physics of lowest energies is covered by a few quasi-particles, i.e. the original interacting many body problem has been projected on an equivalent but simplified few quasi-particle problem. The main idea of such continuous unitary transformations goes back to Wegner for in 1994 [28]. 1993 similar ideas were published in the context of high-energy physics by Glazek and Wilson [29]. Knetter and Uhrig modified Wegner's method to make it more robust and easier calculable for most models on the one hand and on the other hand they changed Wegner's idea of making the Hamiltonian more "diagonal" to the just introduced idea of quasi-particles and making the Hamiltonian block-diagonal in the number of those quasi-particles [30]. They followed ideas of Stein [31]. Mathematically the procedure is similar to that of flow equations that diagonalize block-diagonal matrices. Those were written down by Mielke in 1998 [32, 31]. His generator equals the commonly called "Toda flow" generator used to diagonalize tridiagonal matrices [33]. For all following calculations the approach of Knetter and Uhrig is used. Mathematically the CUT can be expressed as follows. One starts with an initial Hamiltonian

$$\mathcal{H}(0) = \mathcal{H}_0 + \lambda \sum_n T_n, \tag{3.1}$$

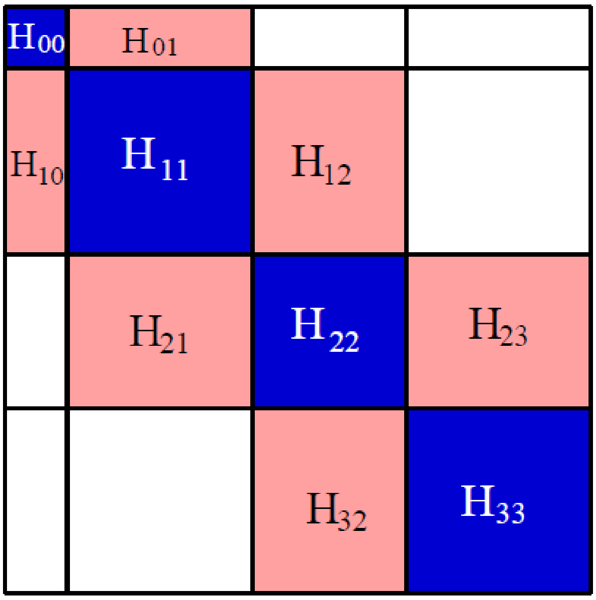

Fig. 3.1: One can see the block structure of the Hamiltonian in the quasi-particle number that is referred to by the indices. After the CUT has been done the red parts of the Hamiltonian will have vanished and the so obtained effective Hamiltonian will be block diagonal in the number of quasi-particles.

where $\mathcal{H}_0$ is the unperturbed Hamiltonian and $[\mathcal{H}_0, T_n] = nT_n$. The unperturbed Hamiltonian is assumed to have an equidistant energy spectrum bounded from below $\mathcal{H}_0 = \sum_\nu t^\dagger_{\nu,\alpha} t_{\nu,\alpha}$. Thus T_n increments or decreases the number of these energy quanta by n. Furthermore n is assumed to be bounded from below and above ($n = -N, ..., N$). The energy quanta of $\mathcal{H}_0$ can be interpreted as particles that can be created or annihilated. The dimerized chain and the two-leg ladder both fulfil the stated requirements.

Starting with $\mathcal{H}(0)$ the idea now is to perform a unitary transformation that is continuously transforming the Hamiltonian for $l \in \mathbb{R}^+$ such that $\mathcal{H}(\infty)$ gives the desired transformed Hamiltonian. The continuous unitary transformation that achieves that can be specified and given for every $l \in \mathbb{R}^+$:

$$\frac{d}{dl}\mathcal{H}(l) = [\eta(l), \mathcal{H}(l)]. \tag{3.2}$$

The quasi-particle generator is given by

$$\eta_{i,j}(l) = \mathrm{sgn}(q_i - q_j)\mathcal{H}_{i,j}(l) \tag{3.3}$$

in the eigenbasis $|i\rangle$ of $\mathcal{H}_0$ which equals a number operator, i.e. $\mathcal{H}_0 |i\rangle = q_i |i\rangle$. In this flow equation the choice of $\eta(l)$ was modified by Knetter and Uhrig to that of Wegner. Stein used a similar generator earlier [31]. The advantage of this generator compared to Wegner's is that $|q_i - q_j| \leq N$ remains bounded during the transformation. If the transformation gets performed this way for $l = \infty$ the Hamiltonian will be block diagonal in the different particle number blocks, i.e. it will be achieved that $\mathcal{H}_{i,j}(\infty) = \delta_{i,j}\mathcal{H}_{i,j}(\infty)$.

3.2. Perturbative continuous unitary transformations

The difficulty in calculating $\mathcal{H}(\infty)$ is that one has to solve an infinite hierarchy of differential equations. In most cases of practical interest this is not possible. One way to derive approximate solutions is to truncate the set of differential equations at some point. If the point of truncation is a good one or not will usually depend on the strength of the perturbation λ. The way the truncation is done here is by using perturbative continuous unitary transformations (pCUT), i.e. the truncation is done in a perturbative manner. One uses a series ansatz for the generator

$$\eta(l) = \sum_{k=1}^{\infty} \sum_{|\boldsymbol{m}|=k} \mathrm{sgn}(M(\boldsymbol{m})) F(l;\boldsymbol{m}) \widetilde{T}_\lambda(\boldsymbol{m}) \tag{3.4}$$

with

$$\widetilde{T}_\lambda(\boldsymbol{m}) = (\lambda \widetilde{T}_{m_1}) \cdot \ldots \cdot (\lambda \widetilde{T}_{m_k}) \tag{3.5}$$

and

$$M(\boldsymbol{m}) = \sum_{i=1}^{k} m_i. \tag{3.6}$$

The vector $\boldsymbol{m}$ has as many components as the perturbation order and its components values are bounded by $-N$ and N:

$$\boldsymbol{m} = (m_1, .., m_k),\ m_i \in [-N, ..., N]. \tag{3.7}$$

$F(l;\boldsymbol{m})$ are real valued functions. By using the flow equation differential equations for the functions $F(l;\boldsymbol{m})$ can be explicitly written down. Finally for $l = \infty$ the effective Hamiltonian reads

$$\mathcal{H}_{\text{eff}}(\lambda) = \mathcal{H}(\infty) = \mathcal{H}_0 + \sum_{k=1}^{\infty} \sum_{|\boldsymbol{m}|=k, M(\boldsymbol{m})=0} C(\boldsymbol{m}) \widetilde{T}_\lambda(\boldsymbol{m}) \tag{3.8}$$

with $C(\boldsymbol{m}) = F(\infty;\boldsymbol{m})$ being rational numbers. The summands can be viewed as virtual fluctuations of the new dressed particles defined by the effective Hamiltonian [34]. Once the coefficients $C(\boldsymbol{m})$ are known up to a finite order of the perturbation the effective particle conserving Hamiltonian can be calculated to this order. In practice quite high orders can be reached for the perturbation theory, e.g. calculations of order 14, although the number of coefficients rises exponentially with the order of perturbation [35, 23]. The coefficients can be calculated with the differential equations for $F(l;\boldsymbol{m})$. A big advantage is that once the coefficients are known they can be used for any model that fulfils the properties of $\mathcal{H}$ stated above. Model dependent properties come into play with the different structure of the $\widetilde{T}(\boldsymbol{m})$ operators and their normal ordering only. This ansatz and more details can be found in [30].

3.2.1. Linked-cluster expansion

One important property of the pCUT and the resulting effective Hamiltonian is its cluster additivity [36]. A cluster is a finite subset of supersites of the system and its bonds. Cluster additivity means that for the clusters A, B, C with $C = A \cup B$ and $A \cap B = 0$

$$\mathcal{H}_{\text{eff}}^{C} = \mathcal{H}_{\text{eff}}^{A} \otimes \mathbf{1}^{B} + \mathbf{1}^{A} \otimes \mathcal{H}_{\text{eff}}^{B}. \tag{3.9}$$

As a consequence of the cluster additivity the linked cluster theorem holds and only linked processes have an overall contribution to $\mathcal{H}_{\text{eff}}$ [34]. Thus in the truncated effective Hamiltonian only clusters of the size of the perturbation order ord contribute to

$$\mathcal{H}_{\text{eff}}^{ord}(\lambda) = \mathcal{H}_0 + \sum_{k=1}^{ord} \sum_{|\boldsymbol{m}|=k, M(\boldsymbol{m})=0} C(\boldsymbol{m}) \widetilde{T}_{\lambda}(\boldsymbol{m}). \tag{3.10}$$

E.g. in a one-dimensional model with only nearest neighbour couplings a cluster of 9 linked supersites is enough for all calculations up to order 8. Apart from the context of pCUT it was only in 1996 when Gelfand was the first to set up a true linked-cluster expansion for a one-particle dispersion [28]. The linked-cluster property of the pCUT is an essential key for its ability to efficiently model quenched disorder.

3.2.2. White-graph expansion

In a disordered problem every disordered bond has to get an own perturbation parameter assigned to since its value is not site-independent anymore. The pCUT scheme is able to treat several perturbation parameters quite generally. The effective Hamiltonian in that case is given by

$$\mathcal{H}_{\text{eff}}^{ord}(\{\lambda\}) = \mathcal{H}_0 + \sum_{k=1}^{ord} \sum_{|\boldsymbol{m}|=k, M(\boldsymbol{m})=0} C(\boldsymbol{m}) \widetilde{T}_{\{\lambda\}}(\boldsymbol{m}) \tag{3.11}$$

with more general

$$\widetilde{T}_{\{\lambda\}}(\boldsymbol{m}) = \widetilde{T}_{m_1,\{\lambda\}} \cdot \ldots \cdot \widetilde{T}_{m_k,\{\lambda\}} \tag{3.12}$$

whose perturbation parameters can depend on the lattice supersite and on the possible kind of processes in $\widetilde{T}_{m_i,\{\lambda\}}$ labelled by γ [34]:

$$\widetilde{T}_{m_i,\{\lambda\}} = \sum_{\nu,\gamma} \lambda_{m_i,\nu,\gamma} \tau_{m_i,\nu,\gamma}. \tag{3.13}$$

The linked-cluster property stays valid since several perturbation parameters do not change the cluster additivity. An efficient numerical method to calculate effective Hamiltonian and observables for multiple perturbation parameters on a finite cluster is the so called white-graph expansion developed by Coester and Schmidt [34]. With it the computation time for the effective Hamiltonian can be fastened significantly. Hereby the different perturbation parameters are just plugged in at the very end of a calculation. During the calculation of a certain process the only thing that has to be counted is how often one perturbation parameter has appeared [34]. By asserting a perturbation parameter to every bond of the lattice any possible disorder configuration can be modelled.

3.2.3. pCUT and quenched disorder

Due to the linked-cluster property of the pCUT only clusters of the size of the perturbation order have to be treated. This only has to be done once with arbitrary perturbation parameters. The so obtained series of effective Hamiltonian matrix elements and observables fully incorporates any possible kind of disorder with only limitation the respective perturbation order. Compare e.g. to a treatment with exact diagonalization: The method is limited to finite systems. For a possible disorder configuration the system has to be fully diagonalized just in the same manner as for the non-disordered case. This has to be done a lot of times to obtain good statistics and thus is time consuming. With the pCUT scheme much bigger system sizes can be reached for few-particle problems because the Hilbert space is only growing polynomially. Consequently the time to diagonalize these system is shorter and good statistics is reached earlier. The only drawback is the size of the effective Hamiltonian and observable series - one perturbation parameter for every bond on the finite cluster. The amount of terms in these expressions rises exponentially with the perturbation order and so does the time to evaluate them. This limits the perturbation order that can be reached. Nevertheless orders enough to obtain quantitative results within the convergence radius of the pertubative expansion (her order 8) can be reached. In the following sections the calculation of effective observables and the effective Hamiltonian is described. For the non-disordered two-leg ladder and the non-disordered dimerized chain a lot of insight was gained by these calculations and most is well known [23, 35, 22, 37, 30]. The influence of disorder on these models however is rather little-known. By using the general validity of the following calculations also for the more general disorder setting we want to shed light on the disordered case.

3.2.4. Ground state energy

Quasi-particles can be viewed as emergent phenomena in a complicated system that behaves as if it contained different weakly interacting particles. The same way the description of phonon quasi-particles simplifies the problem of many vibrating atoms in a lattice to a few-body problem here the problem of many interacting spins is reduced to the description of a few quasi-particles on a lattice. These dressed quasi-particles for the two-leg ladder are emerging from the elementary excitations in the isolated rung-limit and incorporate the perturbation. While the triplet operators were denoted by $t_{\nu,\alpha}$ we want to denote the operators of the dressed particles, in the following called triplons, by $\tilde{t}_{\nu,\alpha}$. They generate particles from the new vacuum $|0\rangle$ which is not a product state of singlets anymore, i.e.

$$\tilde{t}^{\dagger}_{\nu,\alpha} |0\rangle = |\nu_{\alpha}\rangle \, . \tag{3.14}$$

Different disorder configuration are denoted as $\{J_\nu\}$. As the effective Hamiltonian is quasi-particle conserving it can always be written in the form

$$\begin{aligned}\mathcal{H}_{\text{eff}}(\{J_\nu\}) &= E_0 + \sum_{\nu,\alpha,\delta} a_{\nu,\delta}\left(\tilde{t}^\dagger_{\nu,\alpha}\tilde{t}_{\nu+\delta,\alpha} + h.c.\right) \\ &+ \sum_{\nu,\alpha}\sum_{\delta_1,\beta_1,\delta_2,\beta_2,\delta_3,\beta_3} V^{\beta_1,\beta_2,\beta_3}_{\nu,\delta_1,\delta_2,\delta_3}\left(\tilde{t}^\dagger_{\nu,\alpha}\tilde{t}^\dagger_{\nu+\delta_1,\beta_1}\tilde{t}_{\nu+\delta_2,\beta_2}\tilde{t}_{\nu+\delta_3,\beta_3} + h.c.\right) + ... \\ &= \mathcal{H}_0 + \mathcal{H}_1 + \mathcal{H}_2 + ...\end{aligned} \tag{3.15}$$

This representation of the effective Hamiltonian makes it manifest that it is particle conserving. The only part acting on zero particles is E_0. On one particle both E_0 and the terms where first one particle is annihilated and afterwards again created act on and so on for more particles. In short on a certain number n of particles all parts of $\mathcal{H}_{\text{eff}}$ that act on more than n particles have no influence. The form (3.15) of the effective Hamiltonian could in principle be obtained by normal ordering of equation (3.11). In practice however it is easier to leave the Hamiltonian in form (3.11), let it act upon an input state and then project on the desired output state. This can be done with the so called "Solver" developed by Daniel Klagges. From equation (3.15) it is clear that $E_0 = \langle 0|\,\mathcal{H}_{\text{eff}}(\{J_\nu\})\,|0\rangle$. The linked cluster theorem has to be used to obtain it in the thermodynamic limit for a certain perturbation order ord. For that the contributions of all linked clusters have to be summed. One needs to let $\mathcal{H}_{\text{eff}}$ act on clusters of $i = 2, ..., ord + 1$ supersites and each time calculate the cluster dependent value $\bar{E}_{0,\text{cl}_i}$. The total ground state energy is extensive and thus infinite for an infinite system. Finite is the average ground state energy per rung and it is

$$\bar{E}_0 = \sum_{i=2}^{ord+1} \bar{E}_{0,\text{cl}_i}. \tag{3.16}$$

This quantity is constant also for an infinitely disordered system since the disorder averages out. One obtains it by averaging the cluster dependent quantities $\bar{E}_0(i)$ over all disorder configurations.

$$\bar{E}_0 = \sum_{i=2}^{ord+1} \left\langle \bar{E}_{0,\text{cl}_i} \right\rangle. \tag{3.17}$$

3.2.5. One-triplon effective Hamiltonian

The one triplon coefficients can be calculated analogously by letting the Hamiltonian in form (3.11) act on triplons and because of magnetic quantum number conservation of the two-leg ladder and $SU(2)$-invariance it is enough to only consider $\alpha = z$. For the hopping coefficients of the triplons one just has to calculate

$$a_{\nu,\delta} = \langle 0|\, t_{\nu,z}\mathcal{H}_{\text{eff}}(\{J_\nu\})_{\text{cl}} t_{\nu+\delta,z}\,|0\rangle \tag{3.18}$$

if $\delta \neq 0$. For $\delta = 0$ one has to take into account that this calculation would also give the contribution of $\bar{E}_{0,\mathrm{cl}}$ on the cluster where one calculates the hopping elements. Thus for $\delta = 0$ this has to be subtracted to obtain the appropriate contribution

$$a_{\nu,0} = \langle 0|\, t_{\nu,z}\mathcal{H}_{\mathrm{eff}}(\{J_\nu\})_{\mathrm{cl}} t_{\nu+\delta,z}\, |0\rangle - \langle 0|\, \mathcal{H}_{\mathrm{eff}}(\{J_\nu\})_{\mathrm{cl}}\, |0\rangle \,. \tag{3.19}$$

3.2.6. Two-triplon effective Hamiltonian

The two triplon effective Hamiltonian contains all parts of $\mathcal{H}_{\mathrm{eff}}$ that act on two particles simultaneously.

$$\mathcal{H}_2 = \sum_{\nu,\alpha} \sum_{\delta_1,\beta_1,\delta_2,\beta_2,\delta_3,\beta_3} V^{\beta_1,\beta_2,\beta_3}_{\nu,\delta_1,\delta_2,\delta_3} \left(\tilde{t}^\dagger_{\nu,\alpha}\tilde{t}^\dagger_{\nu+\delta_1,\beta_1}\tilde{t}_{\nu+\delta_2,\beta_2}\tilde{t}_{\nu+\delta_3,\beta_3} + h.c.\right) \tag{3.20}$$

For inelastic neutron scattering observables only the two particle states with total spin 1 and magnetic quantum number 0 are of relevance. These states are antisymmetric combinations of x- and y-triplons and because they are the only ones of interest from now on are simply denoted by

$$|\nu, \nu+\delta\rangle = \frac{1}{\sqrt{2}} \left(\tilde{t}^\dagger_{\nu,x}\tilde{t}^\dagger_{\nu+\delta,y} - \tilde{t}^\dagger_{\nu,y}\tilde{t}^\dagger_{\nu+\delta,y}\right)|0\rangle \tag{3.21}$$

with $\delta > 0$. A calculation of

$$\langle \nu+\delta_2, \nu+\delta_3|\, \mathcal{H}_{\mathrm{eff}}(\{J_\nu\})_{\mathrm{cl}}\, |\nu, \nu+\delta_1\rangle \tag{3.22}$$

is only equivalent to

$$\langle \nu+\delta_2, \nu+\delta_3|\, \mathcal{H}_2(\{J_\nu\})_{\mathrm{cl}}\, |\nu, \nu+\delta_1\rangle \tag{3.23}$$

if $\delta_{\nu+\delta_2,\nu}\delta_{\nu+\delta_3,\nu+\delta_1}\delta_{\nu+\delta_2,\nu+\delta_1}\delta_{\nu+\delta_3,\nu} = 0$. If both particles remain at the same place contributions of $\mathcal{H}_0$ and $\mathcal{H}_1$ have to be subtracted. If just one place remains the same contributions of $\mathcal{H}_1$ have to be subtracted only. For a calculation on a finite cluster cl this can be expressed as

$$\begin{aligned}
&\langle \nu+\delta_2, \nu+\delta_3|\, \mathcal{H}_2(\{J_\nu\})_{\mathrm{cl}}\, |\nu, \nu+\delta_1\rangle = \langle \nu+\delta_2, \nu+\delta_3|\, \mathcal{H}_{\mathrm{eff}}(\{J_\nu\})_{\mathrm{cl}}\, |\nu, \nu+\delta_1\rangle \\
&- \delta_{\nu+\delta_2,\nu}(1-\delta_{\nu+\delta_3,\nu+\delta_1})\, \langle \nu+\delta_3|\, \mathcal{H}_{\mathrm{eff}}(\{J_\nu\})_{\mathrm{cl}}\, |\nu+\delta_1\rangle \\
&- (1-\delta_{\nu+\delta_2,\nu})\delta_{\nu+\delta_3,\nu+\delta_1}\, \langle \nu+\delta_2|\, \mathcal{H}_{\mathrm{eff}}(\{J_\nu\})_{\mathrm{cl}}\, |\nu\rangle \\
&+ \delta_{\nu+\delta_2,\nu+\delta_1}(1-\delta_{\nu+\delta_3,\nu})\, \langle \nu+\delta_3|\, \mathcal{H}_{\mathrm{eff}}(\{J_\nu\})_{\mathrm{cl}}\, |\nu\rangle \\
&+ (1-\delta_{\nu+\delta_2,\nu+\delta_1})\delta_{\nu+\delta_3,\nu}\, \langle \nu+\delta_2|\, \mathcal{H}_{\mathrm{eff}}(\{J_\nu\})_{\mathrm{cl}}\, |\nu+\delta_1\rangle \\
&- \delta_{\nu+\delta_2,\nu}\delta_{\nu+\delta_3,\nu+\delta_1}\, (\langle \nu+\delta_2|\, \mathcal{H}_{\mathrm{eff}}(\{J_\nu\})_{\mathrm{cl}}\, |\nu\rangle + \langle \nu+\delta_3|\, \mathcal{H}_{\mathrm{eff}}(\{J_\nu\})_{\mathrm{cl}}\, |\nu+\delta_1\rangle) \\
&+ \delta_{\nu+\delta_2,\nu}\delta_{\nu+\delta_3,\nu+\delta_1}\, \langle 0|\, \mathcal{H}_{\mathrm{eff}}(\{J_\nu\})_{\mathrm{cl}}\, |0\rangle \,.
\end{aligned} \tag{3.24}$$

3.2.7. Effective observables

The observables for inelastic neutron scattering are expressed in terms of triplet operators. To obtain them in terms of the new triplon operators they have to be transformed by the pCUT:

$$\mathcal{O}_{\text{eff}}(\{\lambda_j\}) = \sum_{k=1}^{ord} \sum_{i=1}^{k+1} \sum_{M(\boldsymbol{m})=k} \widetilde{C}(\boldsymbol{m};i) \mathcal{O}_{\{\lambda\}}(\boldsymbol{m};i), \tag{3.25}$$

with $\mathcal{O}(\boldsymbol{m};i) = \widetilde{T}_{m1} \cdot ... \cdot \widetilde{T}_{m_{i-1}} \mathcal{O} \widetilde{T}_{m_i} \cdot ... \cdot \widetilde{T}_{m_k}$. The coefficients $\widetilde{C}(\boldsymbol{m};i)$ are again model independent rational numbers and can be calculated by recursive differential equations [34]. In contrast to the effective Hamiltonian here terms that can create or annihilate particles occur. For ground state expectations only terms that create particles from the vacuum are of interest. For a local observable on the two-leg ladder or the dimerized chain they can be written as

$$\mathcal{O}_{\text{eff}}(\{J_\nu\}) \left|0\right\rangle = \left(c_0 + \sum_{\alpha} \sum_{\delta} c_{\nu,\delta} t^{\dagger}_{\nu+\delta,\alpha} + \sum_{\alpha_1,\alpha_2} \sum_{\delta_1,\delta_2} c_{\nu,\delta_1,\delta_2} t^{\dagger}_{\nu+\delta_1,\alpha_1} t^{\dagger}_{\nu+\delta_2,\alpha_2} + (..) \right) \left|0\right\rangle . \tag{3.26}$$

In practice these coefficients will be obtained by letting all terms in equation (3.25) act on the vacuum and that followed projecting on the output state of interest. This can also be done with the "Solver".

3.3. Implementation on lattice

3.3.1. One-particle effective Hamiltonian

In the non-disordered case the one-particle Hamiltonian can be diagonalized in the thermodynamic limit by doing a Fourier transform. In the disordered case at the moment it seems out of reach to obtain results for an infinite system. Hence finite systems with periodic boundary conditions are investigated here.

Depending on a certain probability distribution the couplings on the finite system are chosen randomly but then are fixed (quenched randomness). The one-particle hopping amplitudes are calculated for these couplings by choosing the appropriate subcluster of the finite sytem for each local hopping term (see Fig. 3.2 for an illustration). Once all hopping elements on the finite system are obtained they can be written in a matrix of banded form. The bandwidth is determined by the order of the perturbation series. The calculations in this work were done up to order 8 so that hopping can at most occur 8 supersites to the left or right and the maximum bandwidth of the one-particle matrices is 8.

These matrices were diagonalized with Matlab. Eigenvectors and eigenvalues found this way are all that is needed to calculate the dynamic structure factor. System sizes of up to 15000 supersites can be reached. In practice however it is more useful to diagonalize smaller finite

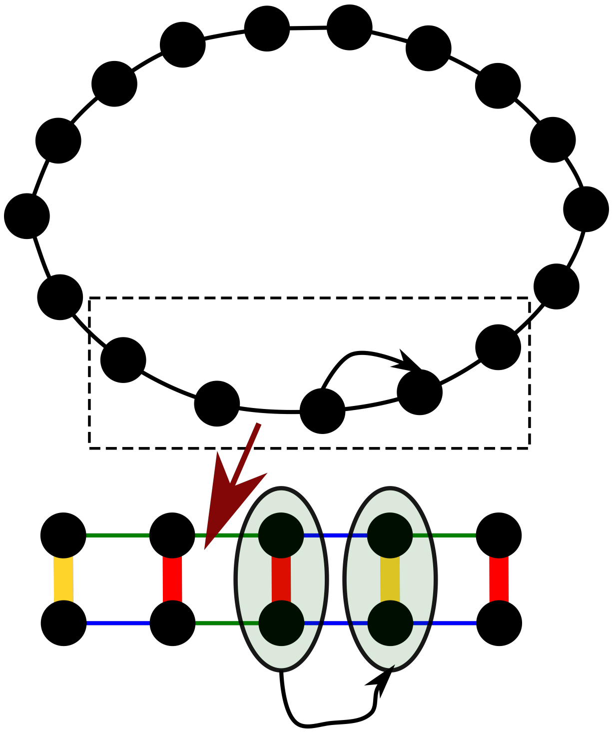

Fig. 3.2: This scheme shall visualize the implementation of disorder on the lattice. The lattice is of finite-size and coupled periodically at the boundaries. The local couplings inside the lattice depend on the disorder configurations of local clusters. As an example five supersites were marked by a rectangle. For a perturbative calculation up to order 4 the next-neighbour hopping process shown by the arrow depends on at most all the different couplings in the local cluster. For a bimodal disorder configuration on the local cluster as shown in the lower part of the scheme this means that every bond and its two possible strengths (colours) will influence the value of the marked next-neighbour hopping process.

sample systems and to average over many of them since this is a lot faster. Finite size effects are usually not that huge and often can already be discarded if system sizes of $N = 100$ are used.

3.3.2. Two-particle effective Hamiltonian

For two particles even in the non-disordered case it is not possible anymore to analytically diagonalize the effective Hamiltonian. The maximum distance of two particles $\mathcal{H}_2$ can act on is given by the perturbation order. Nevertheless one has to include the action of $\mathcal{H}_1$ on two particles as well. Thus the distance of two particles can be infinite. The action of $\mathcal{H}_1$ alone would simply produce two particles states that are built as superpositions of the one particle states. By taking both the action of $\mathcal{H}_1$ and $\mathcal{H}_2$ into account the continua of mixtures of one-particle states remain but also bound states can emerge.
For the disordered case we again take a finite system with periodic boundary conditions and choose its couplings after a certain probability distribution. For a system size of N there are then $N(N+1)/2$ two particle states with total spin 1 and magnetic quantum number 0. The action of $\mathcal{H}_1 + \mathcal{H}_2$ on those states is calculated by choosing the appropriate clusters to calculate every local hopping term of $\mathcal{H}_1$ and all local two-particle interactions induced by $\mathcal{H}_2$. Finite-size effects are huger for the two-particle effective Hamiltonian in the non-disordered case. For reasonable computation times it is however necessary to not make the system size bigger than $N = 100$ which corresponds to diagonalizing a 5050×5050 matrix. Doing this a hundred times takes about 100 minutes. Once the eigenenergies and eigenvectors are obtained this is again everything needed from the sum of the effective one- and two-particle Hamiltonian to calculate the dynamic structure factor in the two-triplon branch.

3.3.3. Dynamic structure factor of the two-leg ladder

The actions of the local observables are calculated on all subclusters of the finite system. To understand the further method we have to bring the dynamic structure factor into another form with the Dirac identity $\frac{1}{x+i0^+} = \mathcal{P}(1/x) - i\pi\delta(x)$:

$$\begin{aligned}\mathcal{S}(k,\omega) &= -\frac{1}{\pi}\operatorname{Im}\left[\langle 0|\left(\widetilde{S}_{k,1z} \pm \widetilde{S}_{k,2z}\right)^\dagger \frac{1}{\omega - (\mathcal{H} - E_0) + i0^+}\left(\widetilde{S}_{k,1z} \pm \widetilde{S}_{k,2z}\right)\,|0\rangle\right] \\ &= \sum_n \delta\left(\omega - \omega_n\right)\langle 0|\left(\widetilde{S}_{k,1z} \pm \widetilde{S}_{k,2z}\right)^\dagger |n\rangle\langle n|\left(\widetilde{S}_{k,1z} \pm \widetilde{S}_{k,2z}\right)\,|0\rangle \\ &= \sum_n \delta\left(\omega - \omega_n\right)\left|\langle n|\left(\widetilde{S}_{k,1z} \pm \widetilde{S}_{k,2z}\right)\,|0\rangle\right|^2 ,\end{aligned} \tag{3.27}$$

where $\sum_n$ sums over all eigenstates $|n\rangle$. They are obtained by diagonalizing the finite systems for one or two particles. Once the action of the local observables is known $\widetilde{S}_{k,1z} \pm \widetilde{S}_{k,2z} = N^{-\frac{1}{2}}\sum_\nu \exp^{-i\nu k}\widetilde{S}_{\nu,1z} \pm \widetilde{S}_{\nu,2z}$ and its action on the ground state can be calculated. The so obtained state has to be projected on the eigenstate $|n\rangle$. The absolute square of this projection then is calculated for the momentum k in discrete steps of $2\pi/N$. The delta function has to be replaced by a discrete binning and the so obtained weights are grouped into size-dependent momentum bins and energy bins of artificial stepwidth. The energy bins can be left like this or be broadened by a discrete Lorentzian curve. Repeating this for all eigenenergies and averaging over many samples finally yields a converged dynamic structure factor that is depending on the energy and momentum binning but shows no system size dependence anymore from a certain system size on. By arguing that the infinite system is independent of a certain infinite disorder configuration one can then say that the finite system shows the same behaviour as the infinite system for discrete energy and momentum bins.

3.3.4. Dynamic structure factor of the dimerized chain

The dynamic structure factor observable for the dimerized chain is different to that of the two-leg ladder but can be reconstructed by using both the symmetric and antisymmetric observables of the ladder. This is the most convenient way since then only the two-leg ladder observables have to be known. The main idea is to split the Fourier transformed spin observable of the dimerized chain in a sum over odd and even sites:

$$\widetilde{S}_{k,z} = \delta_{s,\mathrm{odd}} N^{-\frac{1}{2}} \sum_{s} \exp^{-isk} \widetilde{S}_{s,z} + \delta_{s,\mathrm{even}} N^{-\frac{1}{2}} \sum_{s} \exp^{-isk} \widetilde{S}_{s,z} = \widetilde{S}^{\mathrm{odd}}_{k,z} + \widetilde{S}^{\mathrm{even}}_{k,z}. \tag{3.28}$$

The dimerized chain can then be seen as a special case of the two-leg ladder. Both the sums over even and odd sites are Fourier series running along the supersites of the ladder. Using that one can write the dynamic structure factor as

$$\mathcal{S}(k,\omega) = \sum_{n} \delta\left(\omega - \omega_n\right) \left| \langle n| \, \widetilde{S}^{\mathrm{odd}}_{k,z} + \widetilde{S}^{\mathrm{even}}_{k,z} \, |0\rangle \right|^2 \tag{3.29}$$

with

$$\begin{aligned} \widetilde{S}^{\mathrm{odd}}_{k,z} &= \alpha \, \frac{1}{2} N^{-\frac{1}{2}} \sum_{\nu} \exp^{-i\nu k} \left(\widetilde{S}_{\nu,1z} + \widetilde{S}_{\nu,2z} \right) + (-1)^{\nu} \left(\widetilde{S}_{\nu,1z} - \widetilde{S}_{\nu,2z} \right), \\ \widetilde{S}^{\mathrm{even}}_{k,z} &= \beta \, \frac{1}{2} N^{-\frac{1}{2}} \sum_{\nu} \exp^{-i\nu k} \left(\widetilde{S}_{\nu,1z} + \widetilde{S}_{\nu,2z} \right) + (-1)^{\nu+1} \left(\widetilde{S}_{\nu,1z} - \widetilde{S}_{\nu,2z} \right) \end{aligned} \tag{3.30}$$

and

$$\frac{\alpha}{\beta} = \exp\left(\pm iks\right). \tag{3.31}$$

The phase factor gets a minus if the first upper leg coupling $J^{||}_{1,1} = 0$ and a plus if $J^{||}_{1,2} = 0$. With this mapping the dynamic structure factor of the dimerized chain can be calculated with the two-leg ladder observables in an analogous way as described before. The momenta calculated by the supersite ν based Fourier series have to be divided by two to obtain the corresponding ones for the chain.

3.4. Convergence of numerics

As calculations of the dynamic structure factor can only be obtained for finite systems possible finite-size effects have to be examined. It can also only be calculated for a finite number of samples and a finite number of energy bins. Hence the convergence of the dynamic structure factor with the number of samples for a fixed system size and fixed energy bin width has to be looked at. Assuming that the value in each bin is a random variable and that the disorder configurations of each sample are independent the behaviour of its standard deviation with the number of samples R is $\propto 1/\sqrt{R}$. A system of $N = 100$ rungs and energy bin width of 0.001 was used to examine this behaviour. The disorder configuration of that system was a bimodal disorder on the rungs with $P(J^{\perp} = 1.2) = 0.5$, $P(J^{\perp} = 0.8) = 0.5$ and $J^{\parallel} = 0.3$. For different numbers of samples R the calculation of the dynamic structure factor was done 10 times, i.e. in total $10\,R$ times, and of this series of 10 measurements to fixed sample number R the standard deviation was determined. In Fig. 3.3 one sees the ratio of this standard deviation and the dynamic structure factor for every bin at fixed momentum $k = \pi$. One clearly sees that it goes down for greater numbers of samples. Only at the edges of zero density of states regions this behaviour changes. There the ratio can get bigger for a greater number of samples since the parts of the disordered lattice that contribute are so rare that they just were not there for a smaller number of samples. The statistical behaviour at these edges is excluded in the following. The impact of these energy intervals is arguably negligible for thermodynamic quantities as they are only very small. In the energy range $0.6 < \omega < 0.9$ the values of Fig. 3.3 were averaged and a plot of this average against the number of samples can be seen in Fig. 3.4. From the plot it is evident that this averaged standard deviation goes indeed with $1/\sqrt{R}$. The standard deviation thus scales inversely proportional to the square root of numbers of energies that fall into one bin. From that it is clear that the dependence on the width of the energy bins $\Delta\omega$ is $\propto 1/\sqrt{\Delta\omega}$. One can conclude that for fixed system size and energy bin width the dynamic strucuture factor converges and that the rate of convergence is proportional to $1/\sqrt{\Delta\omega\, R}$.

For the question of finite-size effects it is instructive to have a look at the IPR. Fig. 3.5 shows the IPR of the same bimodal rung disorder system as discussed before. Also the IPR is calculated with the same energy binning. There is no change in the IPR anymore when system size gets changed from $N = 100$ to $N = 500$. One conclusion is that the energy states fit with almost all their weight already on 100 rungs and that there should be no finite-size effects anymore for system sizes of $N = 100$ rungs. Fig. 3.6 shows the dynamic structure factor at fixed momentum $k = \pi$ for both systems. Plotted above each other one can only make out minor differences between the two plots. The relative deviation of both ranges mostly beneath 10%. It makes sense to look at the average deviation of both since their mean values lie very close. In the energy interval $0.6 < \omega < 0.9$ it was approximately 3%. For both figures 3.5 and 3.6 the total number of energies was $2.5 \cdot 10^{6}$ and thus ten times as high as in Fig. 3.4 the value for 500 samples. Reading of the value from Fig. 3.4 as 0.1 this divided by $\sqrt{10}$ gives the standard deviation we expect for the $N = 500$ system in Fig. 3.6 and we thus see that the difference to the $N = 100$ system is below the statistical fluctuations of the $N = 500$ system itself. We thus conclude that these deviations are of a statistical nature and not due

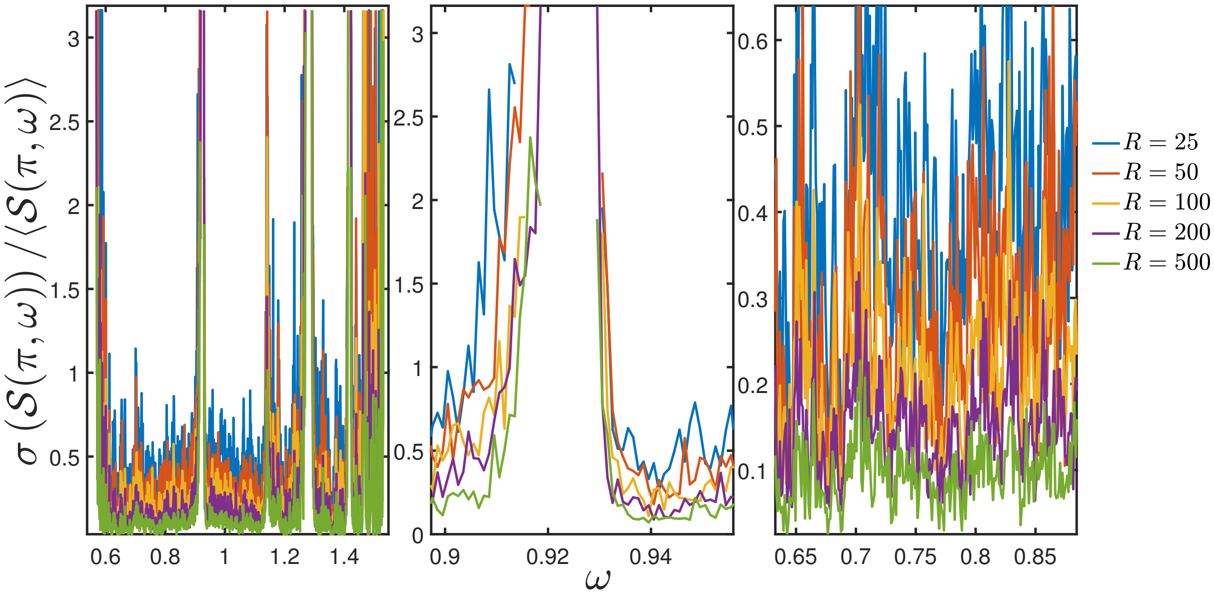

Fig. 3.3: The plots show the standard deviation of 10 independent calculations of the dynamic structure factor at $k = \pi$ for a bimodal rung disorder of $P(J^\perp = 1.2) = 0.5$, $P(J^\perp = 0.8) = 0.5$ and $J^\| = 0.3$. The system size was $N = 500$ and the energy bin width $\Delta\omega = 1/1000$. One can see that the standard deviation goes down with the number of samples for every energy bin except for those at the boundaries of regions with vanishing DOS. The plot in the middle shows the different behaviour at such a zone boundary while the right plot shows the usual behaviour in the energy range $0.6 < \omega < 0.9$.

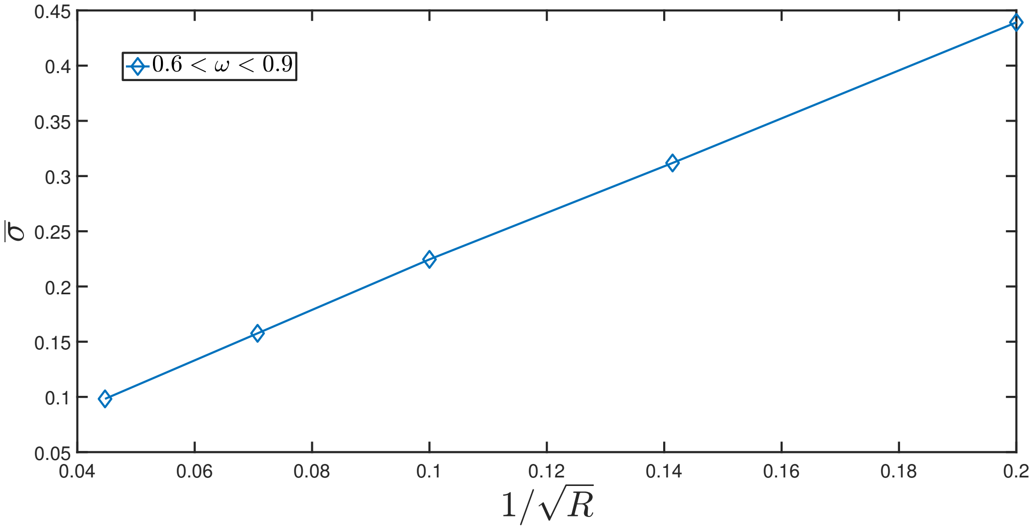

Fig. 3.4: For the region $0.6 < \omega < 0.9$ of the bimodal rung disorder configuration of $P(J^\perp = 1.2) = 0.5$, $P(J^\perp = 0.8) = 0.5$, $J^\| = 0.3$, system size $N = 500$ and an energy bin width of $\Delta\omega = 1/1000$ the mean standard deviation is plotted against the reciprocal square root of the number of samples. The dependence is clearly linear.

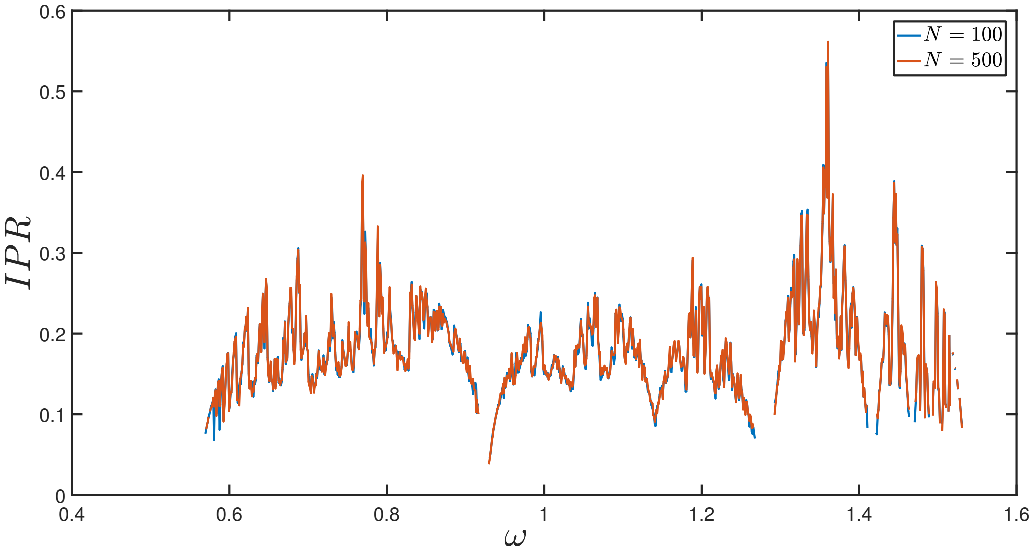

Fig. 3.5: For bimodal rung disorder of $P(J^{\perp} = 1.2) = 0.5$, $P(J^{\perp} = 0.8) = 0.5$ and $J^{\parallel} = 0.3$ and an energy bin width of $\Delta\omega = 1/1000$ the inverse participation ratio shows no finite-size scaling anymore for system sizes greater than $N = 100$.

to finite-size effects. It is claimed that finite-size effects are of no importance anymore for fixed energy bin width when the IPR shows no finite-size scaling anymore for the same energy bin widths. For two-triplon properties the claim is that the same is true when the generalized version of the IPR - IPR_2 - shows no finite-size scaling anymore for the same fixed energy bin widths. The expectation thus is that for moderate rung disorder already small system sizes are sufficient since the value of the IPR is bigger the stronger the disorder is. It hence stops showing finite-size scaling from smaller system sizes on. Reversing this argument weak disorder should show stronger finite-size effects. Generally comparing rung and leg disorder of similar strength the rung disorder will show stronger localization effects. In Fig. 3.7 one sees calculations for a bimodal leg disorder configuration of $P(J^{\parallel} = 0.2) = 0.8$ and $P(J^{\parallel} = 0.3) = 0.2$. This weak disorder configuration still shows big finite-size effects at $k = \pi/2$. One clearly sees that this momentum belongs to the energies where the IPR also has not converged at all for $N = 100$. On the other hand for $k = \pi$ - the IPR has converged for that energies - no finite-size effects can be seen anymore for $N = 100$.

Most of the following results were obtained for system sizes of $N = 100$ and $R = 100$ samples. To increase the convergence with system size often a Lorentzian broadening with full width at half maximum (FWHM) of 0.02 or 0.01 and cut-off at 1% of the maximum value of the Lorentz curve was used. This increases the rate of convergence with number of samples. From Fig. 3.4 one can conclude that deviations to the converged values should be less than 10%. For qualitative discussions of the effects this should be enough. It should be emphasized that this inaccuracy is of a statistical nature and that it is only a matter of time to obtain more precise results. There is no inherent accuracy of the method when one stays within the convergence radius of the perturbative expansion. In some cases better statistics was used to allow smaller bins. Also for the experimentally relevant calculation of

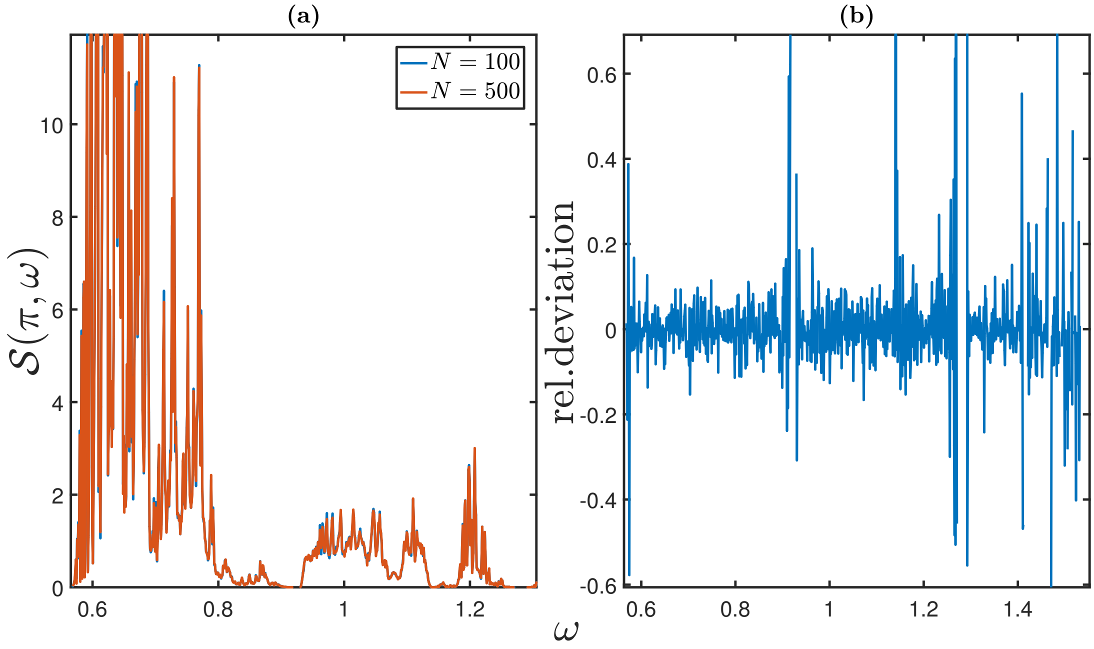

Fig. 3.6: Finite size effects of the dynamic structure factor at $k = \pi$ are looked at for the bimodal rung disorder configuration of $P(J^{\perp} = 1.2) = 0.5$, $P(J^{\perp} = 0.8) = 0.5$ and $J^{\parallel} = 0.3$ and an energy bin width of $\Delta\omega = 1/1000$. Both plotted above each other only show small differences by eye. The relative deviation of both is within the statistical fluctuations of the $N = 500$ system.

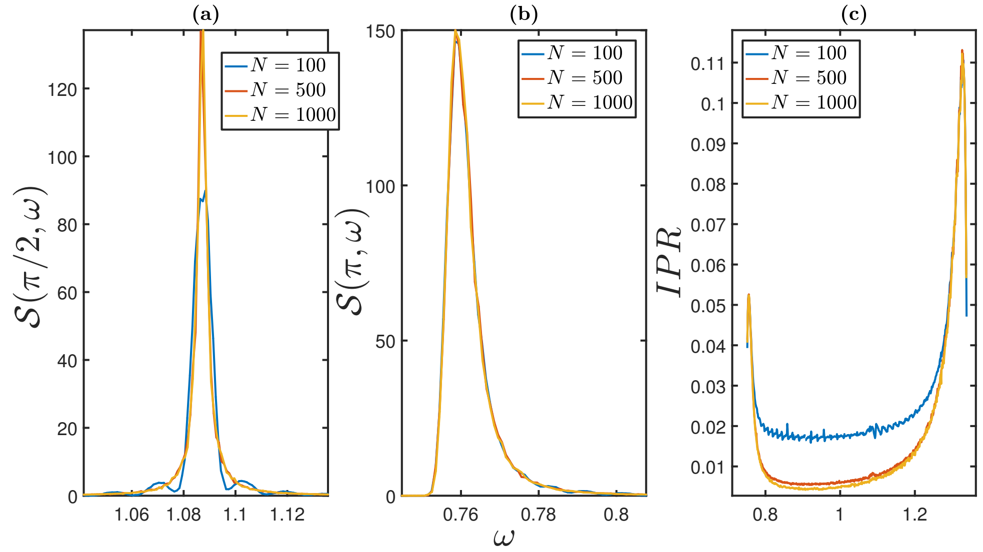

Fig. 3.7: For a bimodal leg disorder configuration of $P(J^{\|} = 0.2) = 0.8$ and $P(J^{\|} = 0.3) = 0.2$ and energy bin width of $\Delta\omega = 1/1000$ strong finite-size effects can be seen at $k = \pi/2$ for a system size of $N = 100$. The inverse participation ratio also still shows order of magnitude differences between systems of $N = 100$ and $N = 500, 1000$ rungs respectively at the corresponding energies. On the other hand for $k = \pi$ the inverse participation ratio seems to be nearly converged and the dynamic structure factor shows no finite-size effects anymore by eye.

the disordered material BPCB$_x$C$_{1-x}$ more samples were used to obtain an accuracy of 1 % for the dynamic structure factor broadened with instrumental resolution. The convergence of the dimerized chain dynamic structure factor can be assumed to behave similarly. Less samples are needed to obtain a good accuracy for the static structure factor since fluctuations in energy are obsolete.

4. Results

The results section will only focus on the two-leg ladder. In appendix A one can find the dynamic structure factor of the dimerized chain for various bimodal rung and leg disorder configurations. The first section gives a short summary of the dynamic structure factor of the non-disordered ladder. Next an overview shall be given for the effects one expects for certain kinds of disorder. After that bimodal disorder on leg and rung is closer looked at. The differences between both as well as the changes with increasing coupling strengths shall be investigated. In contrast to bimodal disorder for continuous disorder rung and leg values can take a continuum of values. Gaussian disorder and also a continuous distribution close to the bimodal one is used to point out differences in density of states and dynamic structure factor when compared to the bimodal distribution. In the last section the experimentally accessible material BPCB$_x$C$_{1-x}$ is modelled and its dynamic structure factor is discussed.

4.1. Short summary of the non-disordered ladder

The non-disordered ladder is translationally invariant. Hence momentum states are one-triplon eigenstates and the dynamic structure factor consists of delta peaks when momentum is fixed. Two curves are needed to describe its behaviour, namely the dispersion curve and the static structure factor. The value of the delta peak for fixed momentum equals the static structure factor for that momentum. One can give the dynamic structure factor as

$$\mathcal{S}(k,\omega') = \sum_k \delta(\omega' - \omega(k))\mathcal{S}(k). \tag{4.1}$$

Fig. 4.1 shows the dispersions for the coupling ratios of 0.15 and 0.5. Clearly visible is that the maximum (minimum) values increase (decrease) when the coupling ratio is increased. Furthermore the dispersion becomes flatter at $k = 0$ and steeper at $k = \pi$ for the coupling ratio of 0.5. This is an effect of higher order terms. In first order the derivatives at $k = 0$ and $k = \pi$ have the same absolute values but different signs. The static structure factor of the antisymmetric observable is 1 for zero leg coupling and becomes dispersive when leg couplings are switched on. The value at $k = 0$ decreases and there it shows its minimum whereas at $k = \pi$ it shows its maximum (see Fig. 4.6). For zero leg coupling the total weight of the 2π normalized antisymmetric structure factor or equivalently the total weight of the static structure factor of this observable is 1. The weight in this sector decreases slowly. For leg couplings of 0.5 it is still bigger than 0.9. In general the total weight of the antisymmetric and the symmetric observable is 1. This holds independently of disorder and coupling ratios and will be used later as a criteria to estimate the convergence of the pCUT. For the non-disordered

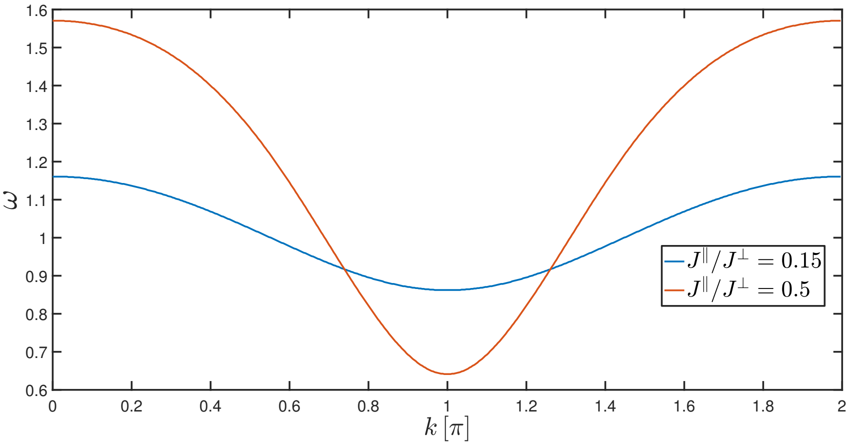

Fig. 4.1: Two-leg ladder dipersion curves for the two different coupling ratios $J^{\|}/J^{\perp} = 0.15$ (blue) and $J^{\|}/J^{\perp} = 0.5$ (red) are shown.

case the convergence radius of the perturbation series is around 0.6 [23].

Even in the non-disordered case the two-triplon problem can not be solved analytically anymore. For fixed momenta the dynamic structure factor can on the one hand take values in a certain range of energies which is given by the upper and lower band edge of the two-triplon continuum. These lower (upper) band edges of the continuum are given by $min_{k'}(\omega(k/2-k')+\omega(k/2+k'))$ $(max_{k'}(\omega(k/2-k')+\omega(k/2+k')))$ for fixed total momentum k [23]. Translational invariance still causes that the total momentum is a conserved quantity. One obtains these upper and lower bounds for the continuum by only considering the action of $\mathcal{H}_1$ on two-triplon states. Due to the hardcore constraint the density of states goes with $\sqrt{\omega}$ at the band edges [38]. On the other hand an attractive interaction between two-triplons is induced by $\mathcal{H}_2$. This shifts the maximum of the DOS to lower energies. Furthermore bound states for fixed total momentum k emerge. Their energy lies below the lower band edge at that momentum. These bound states are two-triplon states with the two triplons very close to each other. At the same time the symmetric observable only ejects weight into two-triplon states with short distances between the two triplons. For small coupling ratios almost all the weight is on two-triplon states with neighboured or next-neighboured two triplons. Both together has the effect that spin-1 and magnetic number 0 two-triplon bound states carry almost all the weight of the symmetric observable in the two-triplon sector although the amount of bound states goes only sub-extensive with system size. In Fig. 4.9 the two-triplon dynamic structure factor is shown for the two coupling ratios 0.15 and 0.5. The influence of the two-triplon interactions is compared to the case with $\mathcal{H}_2 = 0$. One can see that the continuum carries a lot more weight if $\mathcal{H}_2 = 0$ and that the intensities are biggest at $k = \pi$. This is partly because the distance between upper and lower band edge is smallest at π but mainly because the static structure factor of the symmetric observable has biggest weight at π (see Fig. 4.6). Biggest weights can be found close to the lower band edge. This is an effect of the observable that injects most weight on two-triplon states with them being very close as already mentioned. The two-triplon interaction shifts almost all the weight of the observable to bound states that lie below the lower band edge. For the ratio of 0.5 more weight is contained in the bound states than in

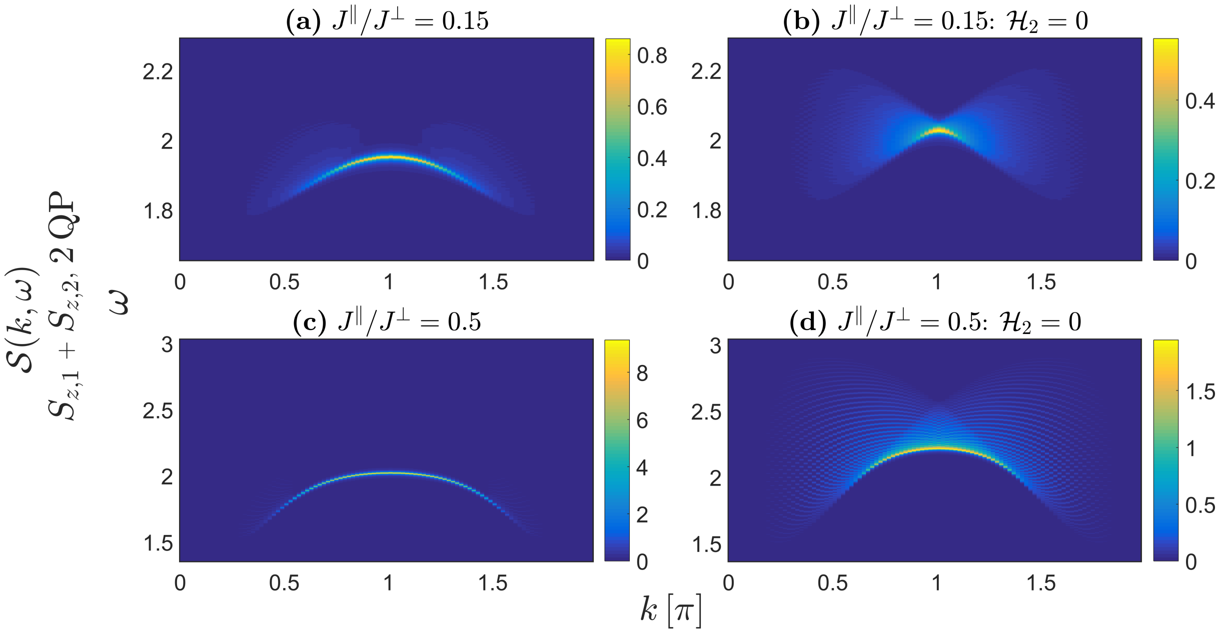

Fig. 4.2: The dynamic structure factor of the symmetric observable in the two-triplon sector is shown for the two different coupling ratios of $J^{\|}/J^{\perp} = 0.15$ and $J^{\|}/J^{\perp} = 0.5$ and with or without two-triplon interactions.

the $J^{\|}/J^{\perp} = 0.15$-case and the continuum is only visible as a shadow above $k = \pi/2$. The maximum value of the dynamic structure factor at $k = \pi$ is ten times bigger for $J^{\|}/J^{\perp} = 0.5$ than for $J^{\|}/J^{\perp} = 0.15$ what can be explained by the much bigger static structure factor of the symmetric observable at $k = \pi$ for the bigger coupling ratio (see Fig. 4.6).

4.2. Different sorts of disorder and their effect on momentum state lifetimes

Disorder on the rung is quite different to disorder on the legs (see also section 2.4). In first order the action of rung disorder is completely local while leg disorder leads to random next-neighbour hopping and comparable rung disorder leads to stronger localization. Hence the first thing to do for distinguishing disorder is by considering if its action is on rung or legs.

Disorder on either leg or rung means that their couplings take values after a certain probability distribution. The information of a probability distribution is covered in all its moments. Two distributions with same mean and variance but different higher moments can show completely different behaviour. Nevertheless these two quantities are convenient measures to group disorder into categories. Disorder configurations with same mean leg and rung couplings and same standard deviations for both couplings will be referred to as configurations with same disorder strength. Next there exist discrete and continuous probability distributions. To examine the differences between both in section 4.4 bimodal disorder is compared with a distribution that

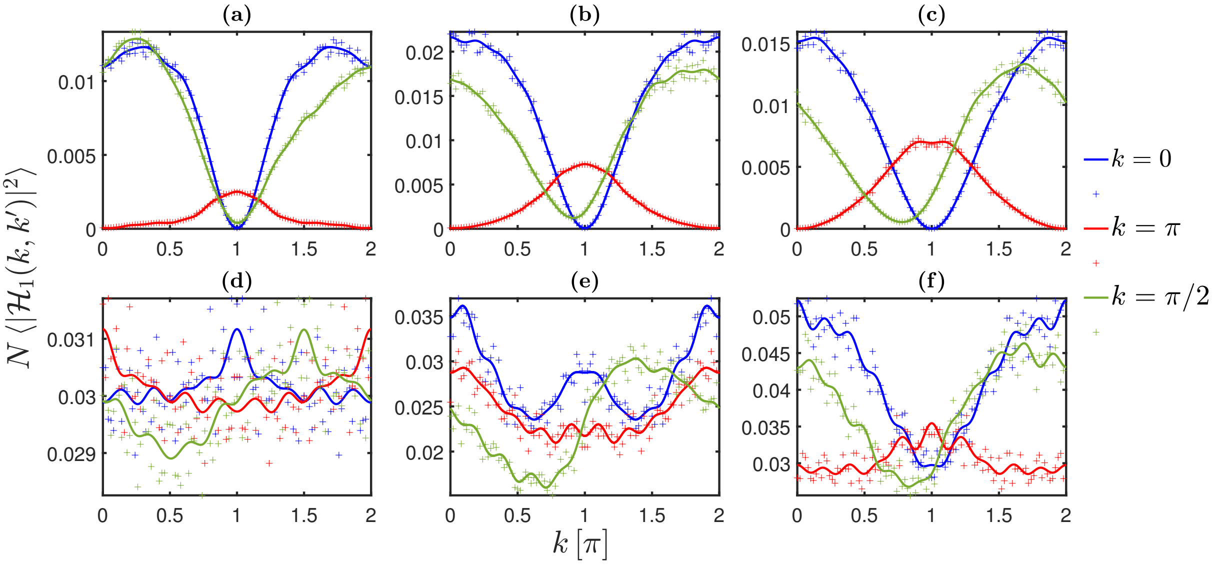

Fig. 4.3: The figure shows the mean of the absolute squared effective one-triplon Hamiltonian in momentum space. Lines were calculated by the analytic expression obtained with the cross-correlation theorem. Crosses were obtained numerically with system sizes of $N = 100$ and $R = 500$ samples. The moments used in the analytic expression were also obtained with these samples.
(a)-(c): Leg disorder of $P(J^{\|} = 0.15) = x$ and $P(J^{\|} = 0.5) = 1 - x$ with $x = 0.2, 0.5, 0.8$.
(d)-(e): Rung disorder of $P(J^{\perp} = 1.175) = 0.5$ and $P(J^{\perp} = 0.875) = 0.5$. In (d) and (e) the leg couplings take the values 0.15 and 0.5. In (f) there is additionally also the leg disorder of (b) occurrent.

has the same mean and same bounds and also takes the two values of the bimodal distribution most often but can also take values in between with a small probability. Then probability distributions can be bounded or not. An example of a not bounded distribution is the Gaussian distribution. In section 4.4 the bimodal distribution is also compared with a Gaussian distribution of same mean and variance.
In the next section a bimodal leg disorder of $P(J^{\|} = 0.15) = x$ and $P(J^{\|} = 0.5) = 1 - x$ will be looked at. As the parameter is x is tuned through the mean and the variance of this distribution changes. The mean increases with x and the variance has its maximum for $x = 1/2$. It shall be qualitatively shown now that rather than the first and the second central moment the ratio $\sigma(J^{\|}_{\nu})/\left\langle J^{\|}_{\nu}\right\rangle$ and $\left\langle J^{\|}_{\nu}\right\rangle$ is decisive for the effect on momentum state lifetimes. For that the mean of the absolute squared one-particle effective Hamiltonian in momentum space is considered. By using the cross-correlation theorem an analytic form can be derived for it that contains only the covariances of the different hopping processes (see appendix B). In first order the broadening of the momentum state $|k\rangle$ follows approximately $\mathrm{Var}(\mathcal{H}_1(k,k)) + \langle|\mathcal{H}_1(2\pi - k, k)|^2\rangle$ and the inverse of the derivative at $\langle\mathcal{H}_1(k,k)\rangle$ (see section 2.4). Clearly this is not true anymore for $k = 0, \pi$ since the derivative is zero there. This is because of the invalidity of the born-approximation at those points. Nevertheless the behaviour of the momentum lifetimes at $k = 0, \pi$ can be assumed to be approximately proportional to

$\mathrm{Var}(\mathcal{H}_1(k,k))$. In first order one could see that the broadening is smallest at $k = \pi/2$ and grows towards $k = 0, \pi$. Also in first order $\mathrm{Var}(\mathcal{H}_1(k,k)) + \langle|\mathcal{H}_1(2\pi - k, k)|^2\rangle$ scales with the variance of the leg disorder. Hence for small values of $\left\langle J^{||}_\nu \right\rangle$ the expectation is that the dynamic structure factor will broaden strongest at $k = 0, \pi$ and that this broadening increases with $\sigma(J^{||}_\nu)$. At $k = \pi/2$ the momentum lifetime should be biggest. That for the shape of the dynamic structure factor not $\sigma(J^{||}_\nu)$ but $\sigma(J^{||}_\nu)/\left\langle J^{||}_\nu \right\rangle$ is the important quantity has to do with the scaling of energy with increasing mean coupling ratio. The broadening of the momentum state scales with $\sigma(J^{||}_\nu)$ but the bandwidth of the mean dispersion scales with $\left\langle J^{||}_\nu \right\rangle$ in first order. In Fig. 4.3 one sees that $\langle|\mathcal{H}_1(k,k')|^2\rangle$ behaves closest to the expectation for $x = 0.8$. All these considerations only used first order terms. When $\left\langle J^{||}_\nu \right\rangle$ is increased higher order terms gradually play a bigger role. Quite remarkable they change the behaviour at the different momentum values $k = 0, \pi/2, \pi$. Fig. 4.3 (a) shows the leg disorder for $x = 0.2$ and Fig. 4.3 (b) for $x = 0.5$. For $x = 0.8$ one could see small deviations between $k = 0, \pi$ that are not there in first order. These increase and for $x = 0.2$ the value of $\mathrm{Var}(\mathcal{H}_1(0,0))$ is already an order of magnitude bigger than the one of $\mathrm{Var}(\mathcal{H}_1(\pi,\pi))$. Also remarkably $\mathrm{Var}(\mathcal{H}_1(\pi/2,\pi/2))$ is an order of magnitude bigger whereas in (c) it was only half as big as $\mathrm{Var}(\mathcal{H}_1(\pi,\pi))$. This leads to conclude that with increasing $\left\langle J^{||}_\nu \right\rangle$ there are big differences in the momentum lifetime at $k = 0$ and $k = \pi$. The expectation is that the lifetime at $k = \pi$ will be significantly bigger. Fig. 4.3 also implies that the dynamic structure factor will have a bigger width at $k = \pi/2$ than at $k = \pi$ for a certain strength of $\left\langle J^{||}_\nu \right\rangle$ on. As cause for the different behaviour at the mean band edges correlations between the local hopping term $a_{\nu,0}$ and other hopping terms were identified. Fig. 4.4 shows the dynamic structure factor for the momenta $k = 0$ and $k = \pi$ one time with the normal local hopping term and one time with it frozen to its mean value. It can be clearly seen that the behaviour of momentum state lifetimes changes completely in between those two scenarios. Thus the fluctuations of the local hopping play a crucial role. In Fig. 4.5 $\langle|\mathcal{H}_1(k,k')|^2\rangle$ is plotted with correlations between the local hopping term $a_{\nu,0}$ and other hopping terms switched off or not for $x = 0.2$. It is obvious that these correlations are responsible for the different momentum lifetimes. One pictorial explanation is that for the non-disordered case, neglecting that there are local hopping terms, an increase in $J^{||}$ decreases the energy at $k = \pi$ and increases it at $k = 0$. The local hopping term also increases with $J^{||}$. It thus increases the value at $k = 0$ further but also increases it at $k = \pi$. This means that correlations between the local hopping term and the other hopping terms lead to constructive interference at $k = 0$ but to destructive at $k = \pi$. There is another effect of the local hopping term that is also due to the instructive interference at one hand and on the other hand because the dispersion at $k = 0$ is getting flatter with increasing coupling ratio (see Fig. 4.1). For bimodal disorder on the leg the local hopping term can lead to local maxima in the dynamic structure factor at $k = 0$ with regions of vanishing weights in between the energy interval of two such local maxima. Qualitatively this can be understood in analogy to Gerschgorin's circle theorem that was used in subsection 2.4.3 to show that strong bimodal rung disorder leads to band gaps when the leg coupling is small enough. Here the leg disorder induces local fluctuations that are similar to the effect of first order rung disorder. The flat dispersion shape at $k = 0$ can be seen as the analogy of the small leg couplings in subsection 2.4.3. However, it should be emphasized that this argument shall only be understood as a

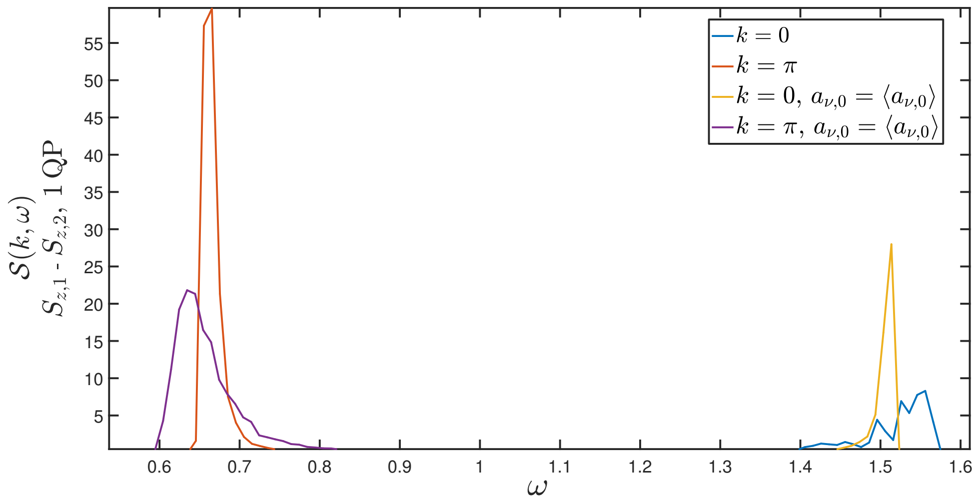

Fig. 4.4: The dynamic structure factor for the leg disorder configuration $P(J^{\|}=0.15)=0.2$ and $P(J^{\|}=0.5)=0.8$ is shown for a system size of $N=100$ and $R=500$ samples. The different behaviour at $k=0$ and $k=\pi$ depending on whether the local hopping term is frozen to its mean value or not is shown. One sees that a constant local hopping term widens the energy range at $k=\pi$ and shrinks it at $k=0$.

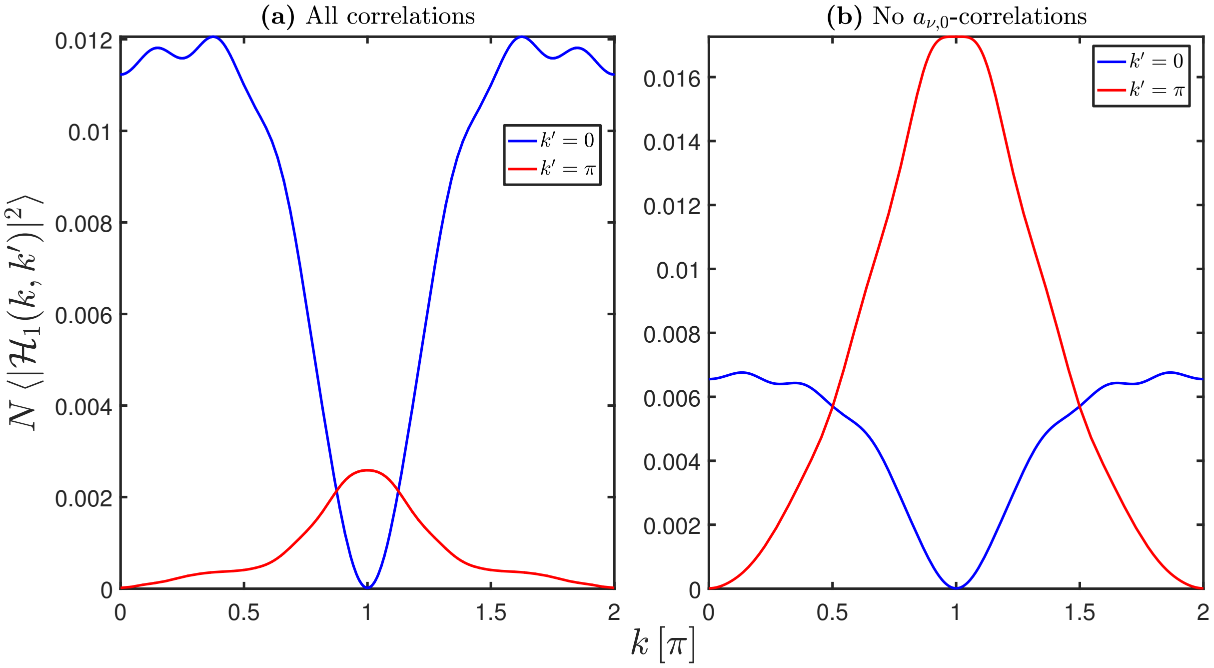
(a) All correlations

(b) No $a_{\nu,0}$-correlations

Fig. 4.5: The mean of the absolute squared effective one-triplon Hamiltonian in momentum space is shown for the leg disorder configuration $P(J^{\|}=0.15)=0.2$ and $P(J^{\|}=0.5)=0.8$. The covariances of the hopping elements were obtained with $R=500$ samples. System size was $N=100$. In (b) the terms belonging to the correlations between the local hopping term and all others are neglected. The values of the $k=0$ ($k=\pi$)-curve increase (decrease) due to these correlations.

qualitative one.
One important effect of rung disorder is a rescaling of the coupling ratio by changing the rung coupling strength. As a first approximation one can think of two different effective leg couplings of $J^{\parallel}/(1+\sigma(J_{\nu}^{\perp}))$ and $J^{\parallel}/(1-\sigma(J_{\nu}^{\perp}))$ that emerge due to the rung disorder. Another important effect for bimodal rung disorder or at least discrete rung disorder is that it can split the dynamic structure into two distinct parts with regions of forbidden energy in between if the rung disorder is strong enough. Gerschgorin's theorem provides a sufficient condition for that. Though, one can see this behaviour often for weaker conditions as Gerschgorin's theorem provides. To examine it in the bimodal disorder section a rung disorder of $P(J^{\perp}=1.175)=0.4$ and $P(J^{\perp}=0.875)=0.6$ is looked at for two different leg-couplings of $J^{\parallel}=0.5$ and $J^{\parallel}=0.15$. For the lower value of the leg coupling in first order Gerschgorin's theorem would predict a splitting into two bands. It is not clear if this remains true when higher order terms are also taken into account. In first order rung disorder only acts locally. Fig. 4.3 (d) and (e) show the just mentioned rung disorder for $J^{\parallel}=0.15$ and $J^{\parallel}=0.5$. For $J^{\parallel}=0.15$ the values are nearly constant no matter which momentum one looks at. One does not expect to see dispersive behaviour in the broadening of momentum states in that case. For $J^{\parallel}=0.5$ the behaviour gets slightly disperse but still one does not expect to see the huge disperse effects of leg disorder on the momentum state lifetime. The offset of the rung disorder, i.e. $\mathrm{Var}(J_{\nu}^{\perp})$, is just too big to allow strong fluctations within the curves. Nevertheless $\mathrm{Var}(\mathcal{H}_1(k,k))$ is at least about 1.4 times bigger at $k=0$ than at $k=\pi$. One can understand this by rung disorder induced fluctuations in the effective coupling ratio. For additional leg disorder $P(J^{\parallel}=0.15)=0.5$ and $P(J^{\parallel}=0.5)=0.5$ (c) the values of $\mathrm{Var}(\mathcal{H}_1(k,k))$ increase due to the added disorder on the leg. Even shorter momentum lifetimes are thus expected. The ratio of lifetimes at $k=0$ and $k=\pi$ however is expected to be not affected since $\mathrm{Var}(\mathcal{H}_1(k,k))$ is still about 1.4 times bigger at $k=0$ than at $k=\pi$.
What was not discussed yet is disorder on the rung and leg that is correlated, i.e. that the leg and rung values depend on each other. This is the case in BPCB$_x$C$_{1-x}$. As was already seen correlations between the local hopping terms and the others can be of great importance. Such correlations can be increased when rung and leg disorder is correlated. Thus, dispersive momentum state lifetimes can again become pronounced though rung disorder is present.

4.3. Bimodal disorder

Bimodal disorder on leg and rung couplings is a form of disorder that is very similar to the disorder present in doped materials. The effect of bimodal disorder on the dynamic structure factor shall be discussed in detail and differences between rung and leg disorder shall be pointed out.

4.3.1. Leg disorder

To examine bimodal leg disorder a disorder configuration of $P(J^{\parallel}=0.15)=x$ and $P(J^{\parallel}=0.5)=1-x$ was looked at. One should mention again that the convergence radius of the non-

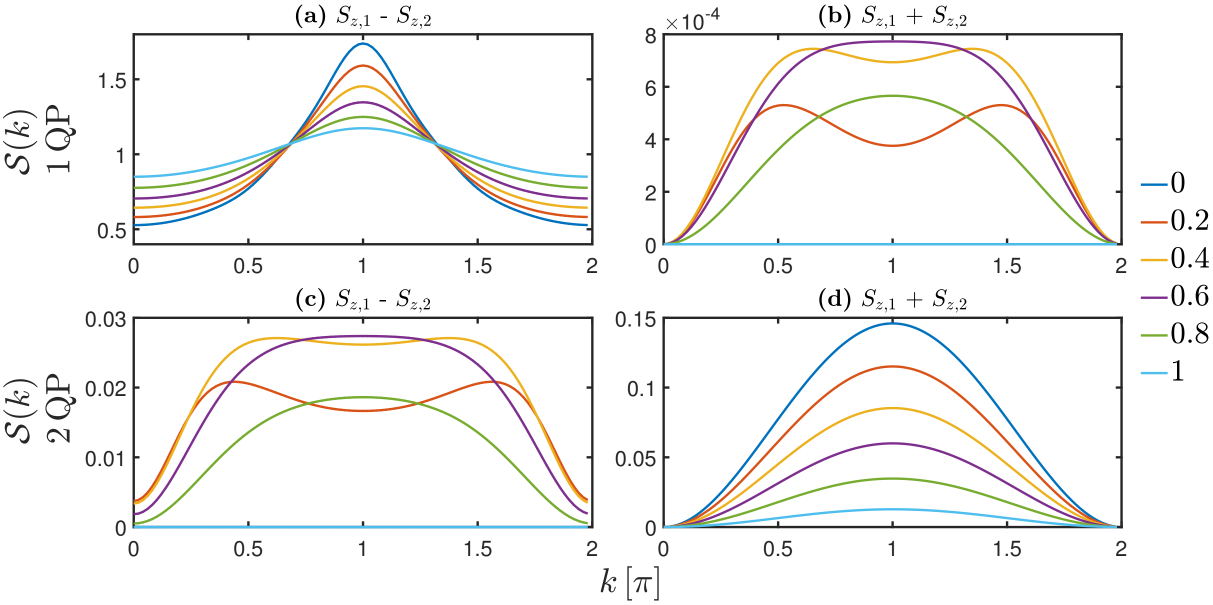

Fig. 4.6: The static structure factor is plotted for the leg disorder configuration $P(J^{\|} = 0.15) = x$ and $P(J^{\|} = 0.5) = 1 - x$ for the antisymmetric and the symmetric observable in the one-triplon ((a) and (b)) and two-triplon sector ((c) and (d)). System size was $N = 100$ and $R = 100$ samples were used.

disordered ladder is approximately 0.6 such that this disorder configuration stays within it [23]. At first the behaviour of the static structure factor is looked at. In Fig. 4.6 one can see plots of it for both observables in the one- and two-triplon sector and for $x = 0, 0.2, 0.4, 0.6, 0.8, 1$. The symmetric observable in the two-triplon as well as the antisymmetric in the one-triplon sector show a behaviour that is very close to the behaviour of $\left\langle J_{\nu}^{\|} \right\rangle$. For the symmetric observable in the one-triplon and the antisymmetric in the two-triplon sector - both only show weight when there is disorder - the situation is different and biggest weights are seen for $x = 0.4$ and $x = 0.6$. Their weight is thus rather going with $\sigma(J_{\nu}^{\|})$.
The dynamic structure factor at fixed momentum k was compared for all observables in the one-triplon channel in Fig. 4.7 and in the two-triplon channel in Fig. 4.8 for $x = 0, 0.2, 0.4, 0.6, 0.8, 1$. For all cases the total weight deviated only up to 0.1 % from 1. This shows that almost all weight is contained in the observables and that one is within the convergence radius of the perturbative expansion.
The symmetric observable always has zero weight at $k = 0$. The statistics of the symmetric observable in the one-triplon channel is not so good because less energy states contribute to it. Nevertheless it shows weight at $k = \pi/2$ and $k = \pi$ which is small but not zero and this effect is due to disorder only. The weight is distributed over a wide range of energies since the states that carry it have to have eigenfunctions localized on parts of the lattice where upper and lower leg coupling are different and $\mathcal{T}_{1,-1}$ processes can inject weight on the observable (see subsection 2.3). These eigenfunctions should be less k-dependent then because of their strong localization.
The antisymmetric observable is widest at $k = 0$ in the one-triplon channel and shows several

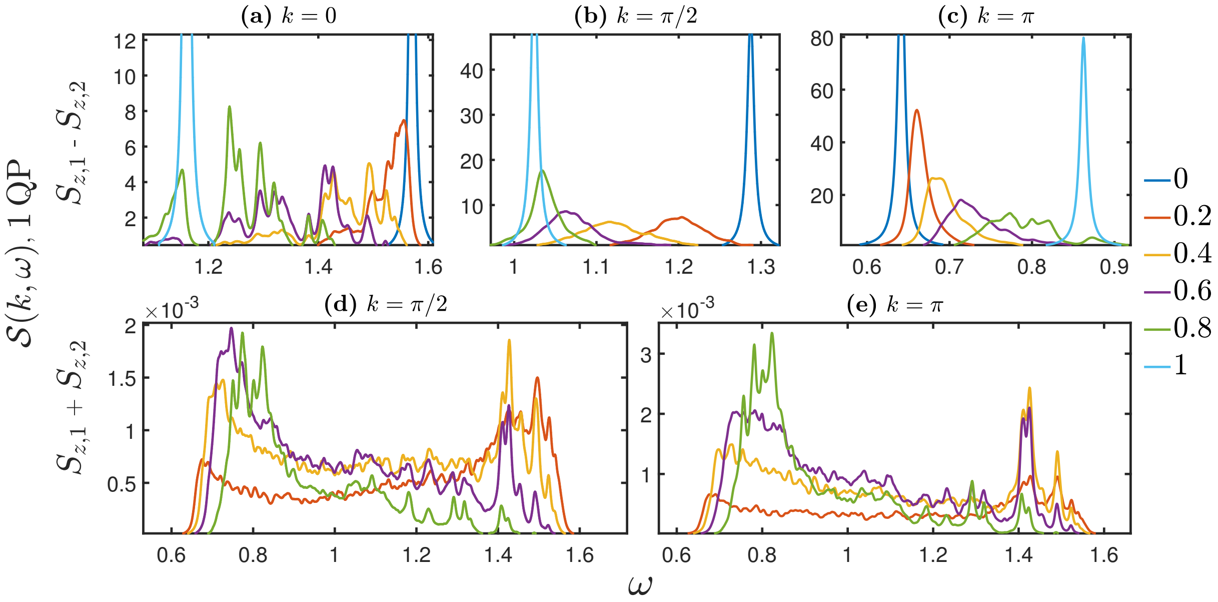

Fig. 4.7: The plot shows the dynamic structure factor of the symmetric and antisymmetric observable in the one-triplon channel for a leg disorder configuration of $P(J^{\parallel}=0.15)=x$, $P(J^{\parallel}=0.5)=1-x$ and $x=0,0.2,0.4,0.6,0.8,1$. It was broadened with a Lorentzian of FWHM of 0.01. System size was $N=100$ and $R=100$ samples were used for averaging.

peaks there. The big width is a higher order effect and can be understood from the values of $\langle \mathcal{H}_{\text{eff}}(k,k')^2\rangle$. A formula for it that covers higher order effects is given in appendix B and the main mechanisms were discussed in the last section. That one sees several peaks is because the bimodal disorder regarded leads to a local hopping terms that takes only a discrete amount of values. The dispersion at $k=0$ is flat and this local fluctuations tear the spectrum apart. The peaks belong to the discrete values the local hopping term can take. The width at $k=\pi/2$ depends strongly on the mean leg coupling $\left\langle J^{\parallel}_{\nu}\right\rangle$. It increases with it, i.e. gets bigger for decreasing x. This can also be explained by the behaviour of $\langle \mathcal{H}_{\text{eff}}(k,k')^2\rangle$ with higher order terms (see section 4.2). The behaviour at $k=\pi$ is the other way round. In the last section it was found that correlations between the local hopping and the other hopping processes lead to the decrease in width when x is decreased.

The two-triplon antisymmetric observable has zero weight in the non-disordered case. Fig. 4.8 shows it in the disordered case and one can see that the weight is small but not zero anymore. It shows at peak at exactly the same energy for the momenta $k=0,\pi/2,\pi$ and its intensity increases with $\sigma(J^{\parallel}_{\nu})/\left\langle J^{\parallel}_{\nu}\right\rangle$ for $k=\pi/2,\pi$. Only at $k=0$ the intensity of curves with high $\left\langle J^{\parallel}_{\nu}\right\rangle$ is bigger. The big width in energy for all three momenta is explained by the same effect as for the symmetric observable in the one-triplon channel: only states where upper and lower leg-coupling are different contribute. Localization lengths are thus very small and momentum-dependence of these energy states is small. That the peak is always at the same energy is surprising. One argument is that most weight of the observable is on two triplons that are neighbours. For them to have weight in the antisymmetric observable upper and lower

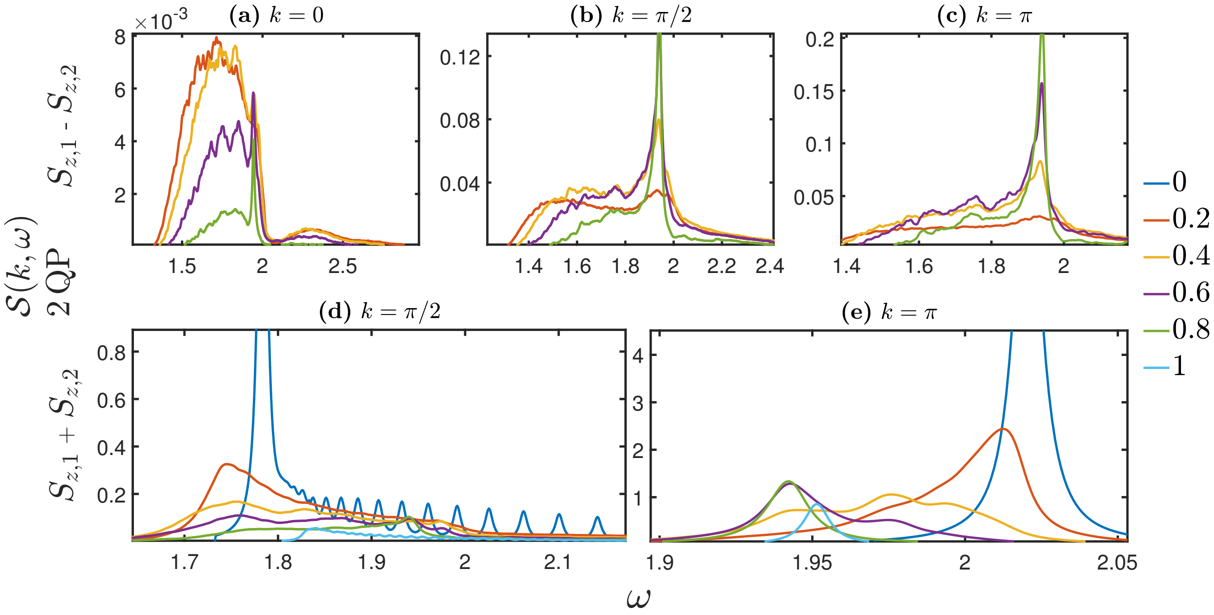

Fig. 4.8: The plot shows the dynamic structure factor of the symmetric and antisymmetric observable in the two-triplon channel for a leg disorder configuration of $P(J^{\parallel}=0.15)=x$, $P(J^{\parallel}=0.5)=1-x$ and $x=0,0.2,0.4,0.6,0.8,1$. It was broadened with a Lorentzian of FWHM of 0.01. System size was $N=100$ and $R=100$ samples were used for averaging.

leg couplings have to be different. Because so unlikely to occur the eigenstates that contribute are very local. Since for all x the possible couplings and hence also their difference is the same the two-triplon peak is always seen at the same energy. This bound state peak is broadened in momentum and good to see for $k=\pi,\pi/2$ for all x (see Fig. 4.8 (b) and (c)). At $k=0$ one only sees it for $x=0.8$ since in the other cases the mean leg coupling is too big and the continuum overlays it.

As the weight is always zero for the symmetric observable at $k=0$ it is also zero in the two-triplon channel of that momentum. At $k=\pi$ (Fig. 4.8 (e)) one can see that the weight of the $x=0.8$ case is bigger than that of the $x=1$ case and is shifted towards lower energies than both of the pure cases. This is surprising at first sight. The reason for the higher intensities is that the higher leg-couplings $J^{\parallel}=0.5$ contribute. The shift to lower-energies is not fully understood but could be due to localization-induced widening in energy or an offset-contribution of $\mathcal{T}_{1,-1}$ processes. For $x=0.6,0.4$ the curves get wider and wider which could be caused by a localization effect on bound states. The configurations of $x=0.8,0.6$ get much wider again for $k=\pi/2$. Stronger influence of the continuum and weaker bound state effects because of smaller mean leg-couplings are made responsible for that. For $x=0.2$ a shift to lower energies similar to that of $x=0.8$ at $k=\pi$ can be seen. In the non-disordered configuration $x=0$ oscillations can be seen at $k=\pi/2$. These are caused by finite-size effects. Due to localization finite-size effects are not present in the disordered cases anymore.

The effect of $\mathcal{H}_2$ on the dynamic structure factor can be seen in Fig. 4.9 for a leg disorder of $P(J^{\parallel}=0.15)=0.4$ and $P(J^{\parallel}=0.5)=0.6$. As in the non-disordered case weight is shifted to smaller energies and also to energies that were not taken before. This energies belonged

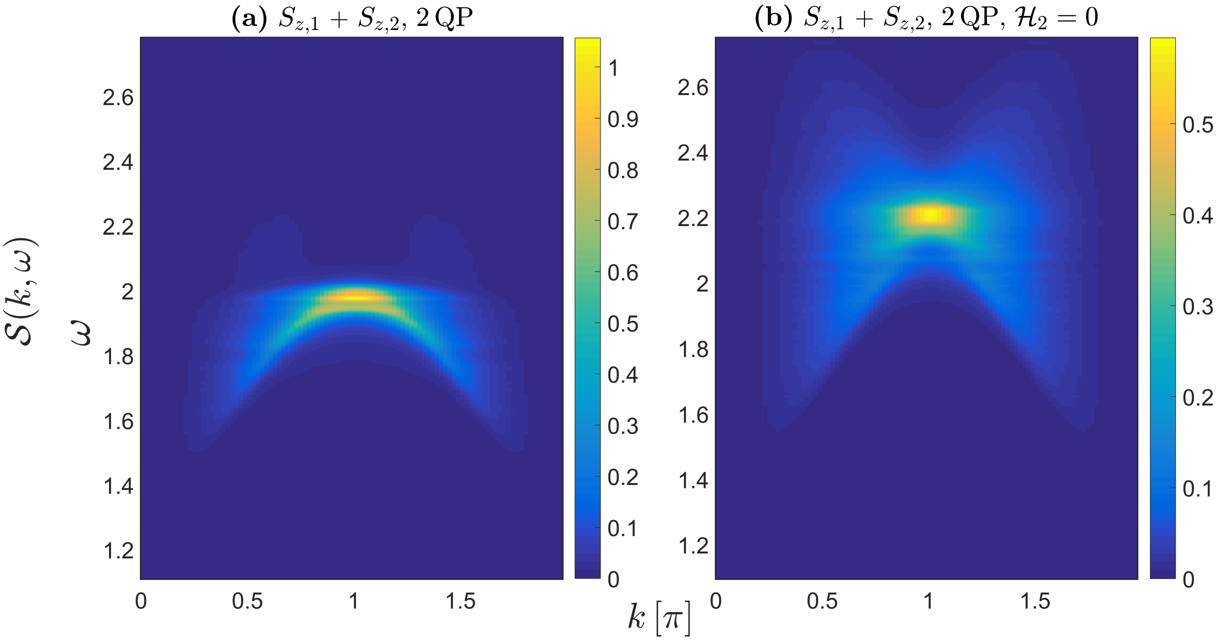

Fig. 4.9: The dynamic structure factor of the symmetric observable in the two-triplon sector is shown for a leg disorder of $P(J^{\parallel} = 0.15) = 0.4$ and $P(J^{\parallel} = 0.5) = 0.6$. In (b) the two-triplon interactions are switched off. System size was $N = 100$ and $R = 100$ samples were used.

to bound states in the non-disordered case. As a fate of these bound states the continuum is suppressed, the shape gets more dispersion like and the width in energy for fixed momenta gets decreased enormously.

Fig. 4.10 shows the dynamic structure of the leg disorder configuration $P(J^{\parallel} = 0.15) = 0.6$ and $P(J^{\parallel} = 0.5) = 0.4$ for fixed momenta. $\mathcal{T}_{1,-1}$ contributions arise due to the disorder and lead to weight in the symmetric one-triplon and the antisymmetric two-triplon channel. Here in this plot it was investigated how strong the effect of these $\mathcal{T}_{1,-1}$-terms is on the symmetric observable in the two-triplon and the antisymmetric in the one-triplon channel. For that it was compared with the result obtained without these terms. The figure clearly shows that for quantitative calculations these terms must not be neglected. They lead to significant measureable effects. Mean-field calculations like the one done in [12] can not deal with those terms however and thus lack the accuracy of the pCUT for this point. The plot also shows that the $\mathcal{T}_{1,-1}$-terms lead to a negative energy-offset. In Fig. 4.8 one saw that bound states had lower energies than both of the pure cases. It can be concluded that this could really be an effect of the $\mathcal{T}_{1,-1}$-terms.

4.3.2. Rung disorder

For rung disorder the static structure factor mainly behaves like the one of a non-disordered ladder with the same leg-coupling and $\left\langle J_{\nu}^{\perp} \right\rangle$ as rung coupling.

Bimodal rung disorder shall be investigated for two different leg-couplings. The rung disorder

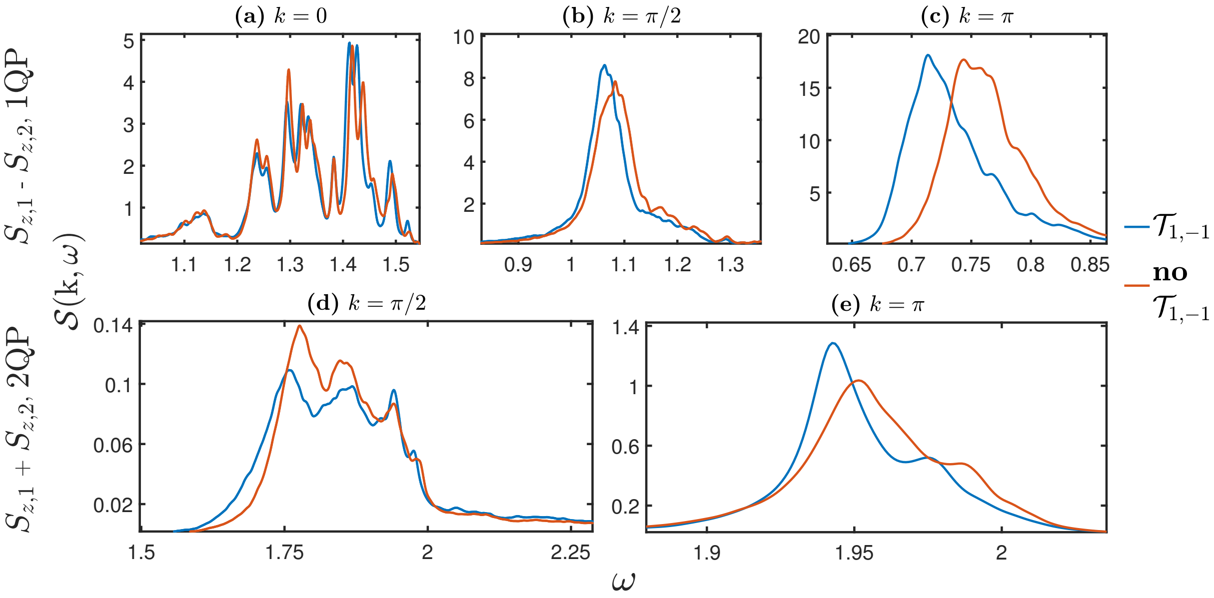

Fig. 4.10: Plot shows the dynamic structure factor for the antisymmetric observable in the one-triplon and the symmetric observable in the two-triplon channel. The system size was $N = 100$ and it was averaged over $R = 100$ samples. After that the result was broadened with a Lorentzian curve of FWHM of 0.01. The blue curves show a leg disorder configuration of $P(J^{\|} = 0.15) = 0.6$ and $P(J^{\|} = 0.5) = 0.4$. Due to the breaking of the exchange symmetry between upper and lower leg couplings $\mathcal{T}_{-1,1}$ processes exist in the Hamiltonian. The red curves show results where these processes were taken out.

choosen is $P(J^{\perp} = 1.175) = 0.4$ and $P(J^{\perp} = 0.875) = 0.6$. The two different leg-couplings are $J^{\|} = 0.5$ and $J^{\|} = 0.15$. For the smaller leg coupling Gerschgorin's theorem would predict that the dynamic structure factor splits into two band-like structures with a bandgap in between. One thing that shall be found out is if that remains true when also higher order terms are taken into account. Another point to find out is if rung disorder has a weaker localization effect when the leg coupling is increased and if the shape gets more dispersion-like again. For that these two different leg couplings were considered. A third comparison is made with a disorder configuration of the same rung disorder but an additional leg disorder of $P(J^{\|} = 0.5) = 0.6$ and $P(J^{\|} = 0.15) = 0.4$. Here the interplay of both leg and rung disorder is of interest. For the small leg coupling the deviation of the total weight of both observables to 1 was smaller than 0.01 %. For the leg coupling of 0.5 the total weight was 0.6 % to small indicating that either weight of higher particle channels is missing or that there are small deviations because the perturbative expansion is not fully converging anymore. The latter has to be true for the case of additional leg disorder where the total weight was 0.4 % too big. Fig. 4.11 shows contour plots of the symmetric two-triplon and the antisymmetric one-triplon dynamic structure factor for these three disorder configurations. One general difference between pure leg or rung disorder is that no $\mathcal{T}_{1,-1}$ terms are present for rung disorder only and thus no weight is in the symmetric one-triplon and the antisymmetric two-triplon channel. In Fig. 4.11 (a) a splitting into two bands can be seen. This can be explained with Gerschgorin's circle theorem when one considers only first order perturbation therory as described in subsection 2.4.3. Higher-order terms are not seen to change that in the plot. In the lower band the effective ratio of leg and rung coupling is increased. This leads to weaker localization effects and a more dispersion-like shape. Also stronger higher order effects are persistent leading to a stronger intensity at $k = \pi$ and also a second intensity peak can be seen around $k = \pi/2$ due to weaker localization there analogous to the one for leg disorder with small mean coupling ratio. The upper band is flater because the effective ratio of leg and rung coupling is decreased and because $P(J^{\perp} = 1.175) = 0.4$ and so chains of consecutive $J^{\perp} = 1.175$-couplings are less likely. In Fig. 4.11 (b) the one-triplon dynamic structure factor for $J^{\|} = 0.5$ shows only a minor splitting into two bands. The shape looks like a broadened dispersion curve. Fig. E.4 compares the inverse participation ratio of both configurations. For the coupling ratio of 0.5 the IPR goes down. This and the less flat shape are both effects of longer localization lengths. The main effect of the rung disorder - that is of the same form - on $\langle|\mathcal{H}_1(k,k')|^2\rangle$ in both cases is an offset of the non-diagonal scattering terms in the magnitude of the variance of the rung disorder. Since the bandwidth of the mean dispersion in the 0.5 is much bigger the effect of these scattering terms is smaller. This way the shape in Fig. 4.11 (b) has a more dispersion-like shape. The bigger leg coupling in Fig. 4.11 (b) also enhances the effect of higher order terms. Those lead to a bigger width and more local maxima at $k = 0$. The local maxima are caused by fluctuations of the local hopping term around the two values it already fluctuates about because of the rung disorder only. This is analogous to the way they arouse for leg disorder. They can also be seen for the smaller leg coupling 0.15 in plot (a). Fig. 4.11 (c) shows the one-triplon dynamic structure factor for the rung- and leg disorder configuration. It appears like a superposition of the dynamic structure factor in Fig. 4.11 (a) and (b) and shows features of both. All in all the effects of rung disorder in the one-triplon sector are similar to those in

the dimerized chain (subsection A.2)
In the two-triplon channel there are big differences to the dimerized chain dynamic structure factor in the presence of rung disorder (see subsection A.2). Generally for the pure cases the bound states are more pronounced for the two-leg ladder and the influence of the continuum is smaller. This transfers to the disordered case where we see more pronounced bound state structures in Fig. 4.11 (d) and (e). The splitting into three bands in (d) is similar to that in the dimerized chain. In (e) we see a temple-like shape caused by higher order effects. This is different to the dimerized chain where the weight of the continuum was so high that it was not possible to resolve such fine structures. The effective ratio of $J^{\|}$ and $J^{\perp}$ is again decisive for the weight of the bound state. E.g. this weight is biggest in the lowest band of plot (d). The shape of the lowest band approaches a dispersion-like shape from (d) to (e). The reason lies in the increasing localization length that can be nicely seen in Fig. E.5 which shows the IPR_2 and the dynamic structure factor at $k = \pi$ for both configurations. For the rung- and leg disorder configuration in (f) bound states become hard to resolve since the additional leg disorder decreases localization length further and smears the DOS. A separation of the lowest band like in (e) and (d) seems not possible anymore. The peaks for fixed momenta are least sharp in (f).

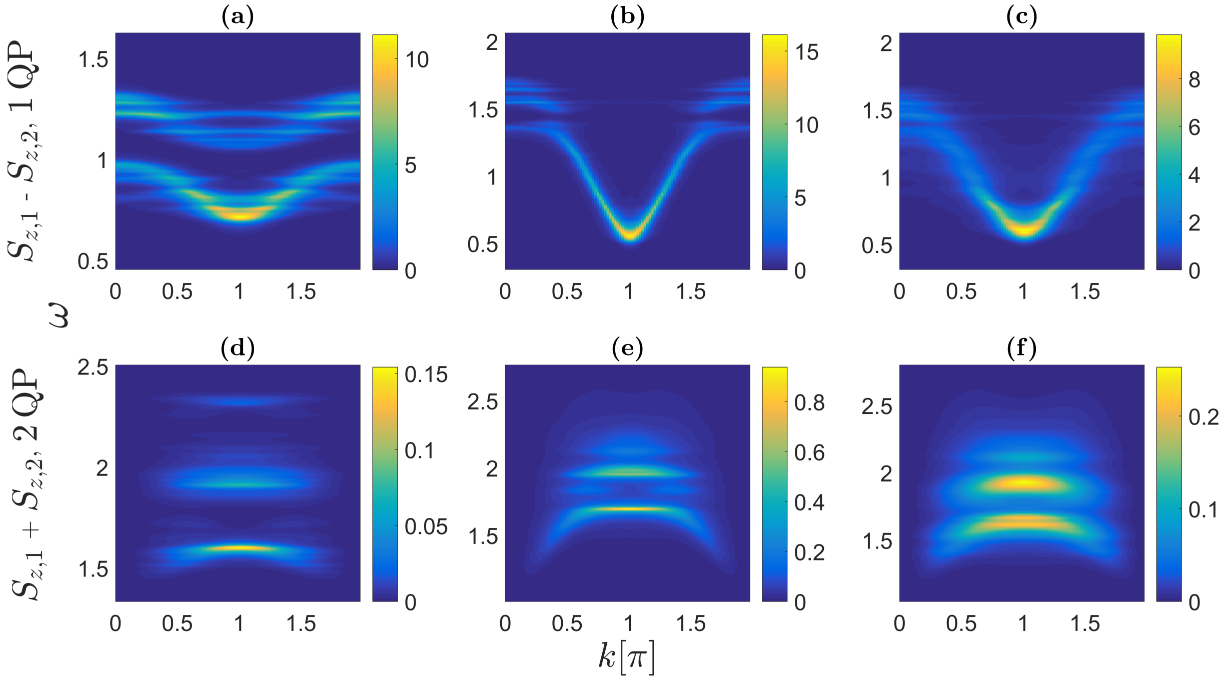

Fig. 4.11: One can see the dynamic structure factor of the antisymmetric observable in the one- and the symmetric observable in the two-triplon channel for a bimodal rung disorder of $P(J^{\perp} = 1.175) = 0.4$, $P(J^{\perp} = 0.875) = 0.6$ and $J^{\|} = 0.15$ in (a) and (d), $P(J^{\perp} = 1.175) = 0.4$, $P(J^{\perp} = 0.825) = 0.6$ and $J^{\|} = 0.5$ in (b) and (e) and a rung and leg disorder configuration of $P(J^{\perp} = 1.175) = 0.4$, $P(J^{\perp} = 0.875) = 0.6$, $P(J^{\|} = 0.5) = 0.6$ and $P(J^{\|} = 0.15) = 0.4$ in (c) and (f). The structure factor was broadened by a Lorentzian of FWHM of 0.02. System size was $N = 100$ and sample size also $R = 100$.

4.3.3. Optimised perturbation theory

Robust extrapolation schemes are called for when dealing with a disorderd problem. DlogPadé extrapolations can be used for accurate and reliable extrapolations but they have the problem of singularities due to poles and this makes it hard to use them in the case many series have to be dealt with. An extrapolation method that is easy to automatize is the so called optimised perturbation theory (OPT) [22, 37, 23]. It is introduced in more detail in appendix C.
For values of the perturbation parameters that lie outside the convergence radius of approximately 0.6 [23] those series start to diverge. Extrapolation techniques can help to go beyond the convergence radius. For comparing the OPT result with the raw series result a disorder configuration of $P(J^{\perp} = 11/7) = 0.5$, $P(J^{\perp} = 3/7) = 0.5$, $P(J^{\parallel} = 1/7) = 0.5$ and $P(J^{\parallel} = 3/7) = 0.5$ was chosen. The choice of this configuration is motivated by the fact that it is very similar to a modelling of leg and rung couplings that can either take the value of BPCB or BPCC with a certain probability. For the raw series the total weight of the antisymmetric and symmetric observable was ≈ 1.46. One can show that the total weight is always 1 on the other hand. This shows that the observable for this configuration already diverges strongly. This is mainly caused by the antisymmetric observable in the two-triplon channel and thus comes from $\mathcal{T}_{1,-1}$ processes. For the dimerized chain the raw series results also diverge earlier [23] and it is argued that physics of the dimerized chain leads to singularities in the raw series of this disorder configuration. In principal one would want the OPT to be optimised with a parameter for every supersite of the lattice. This is possible but the problem is finding a suitable criterion. Here it has been used instead the linearity of the OPT and the splitting parameter a of the OPT was chosen such that for the gap of the disorder configuration $J^{\perp} = 3/7$ and $J^{\parallel} = 3/7$ the OPT result agrees with results taken from the literature (for those results see e.g. [23]). These values are taken consecutively for rung and leg couplings only with a very small probability. For these regions the ladder reaches the isotropic point where leg and rung couplings equal. Since the original series diverges for those cases they were used to optimize with the OPT. Actually it is very unlikely that those couplings are taken for a longer ladder segment. Also other coupling configurations can lead to disorder and especially those where upper and lower leg coupling are different and $\mathcal{T}_{1,-1}$ processes contribute are believed to be most important. The isotropic point was chosen because the proper values for the gap are known there. It is clear that this is not the best possible solution. Though, also the parameter a of the OPT would be increased when one tries to optimize rare configurations with different upper and lower leg coupling and the value used here lies somewhere in between the one needed to regularize such $\mathcal{T}_{1,-1}$-induced quantities and zero. Configurations with mostly small coupling ratios and the quantities that belong to them on the other hand will be hardly affected by the OPT. The comparison of the OPT result and the raw series can be seen in Fig. 4.13. The divergent behaviour of the antisymmetric observable in the two-triplon and the symmetric observable in the one-triplon sector is gone. The total weight of both observables is decreased to approximately 1.03. It is not clear if the so obtained results are correcting the raw series exactly in the right way but it is clear that the results are more realistic since the diverging behaviour is gone.

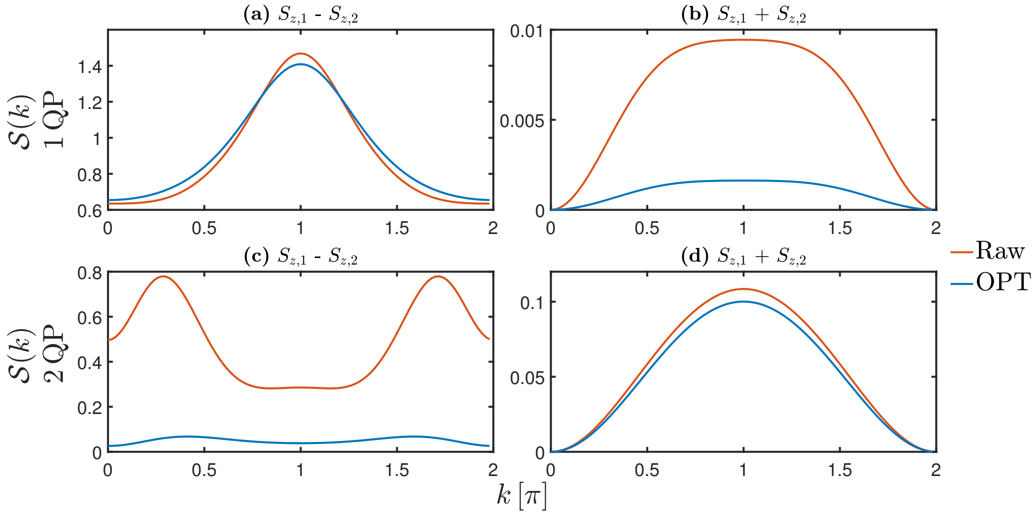

Fig. 4.12: The static structure factor of the bimodal disorder configuration $P(J^{\perp} = 11/7) = 0.5$, $P(J^{\perp} = 3/7) = 0.5$, $P(J^{\parallel} = 1/7) = 0.5$ and $P(J^{\parallel} = 3/7) = 0.5$ is plotted. In blue the OPT results are shown. The weight is decreased especially in the symmetric one triplon-sector (b) and the antisymmetric two-triplon sector (c). System size was $N = 100$ and $R = 100$ samples were used.

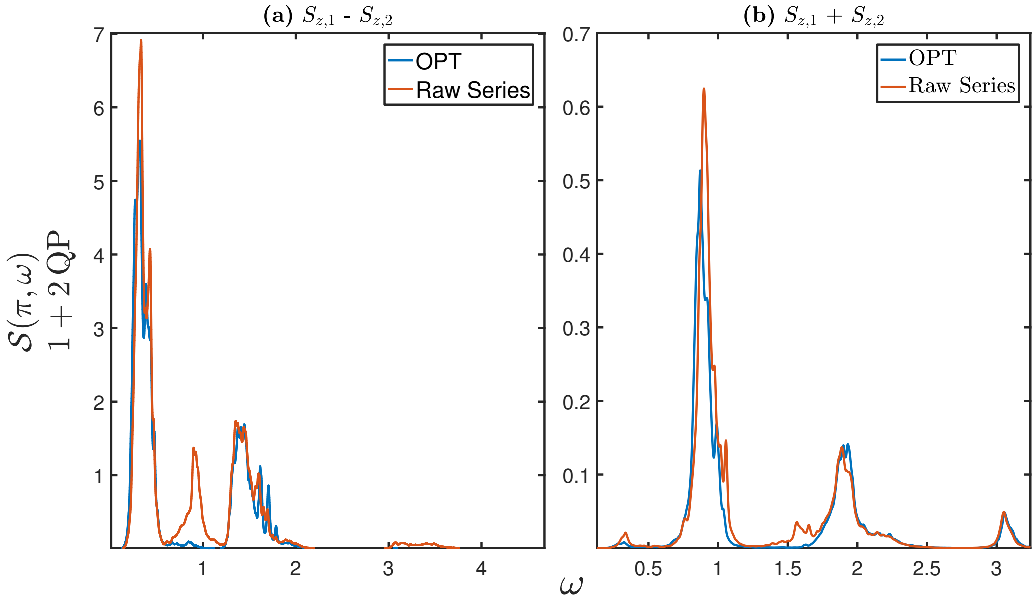

Fig. 4.13: The dynamic structur factor for the antisymmetric (left plot, (a)) and symmetric (right plot, (b)) observable is plotted as the sum of one- and two-triplon contributions. This was done by averaging $R = 100$ samples of system size $N = 100$ and broadening the result with a Lorentzian curve of FWHM of 0.02. The bimodal rung and leg disorder configuration was $P(J^{\perp} = 11/7) = 0.5$, $P(J^{\perp} = 3/7) = 0.5$, $P(J^{\parallel} = 1/7) = 0.5$ and $P(J^{\parallel} = 3/7) = 0.5$. In blue the result of the OPT extrapolation scheme is displayed. The red curve shows the raw series result.

4.4. Comparison with continuous disorder

So far only bimodal disorder was investigated. Any kind of disorder can be modelled with the pCUT method. In this section bimodal disorder shall be compared with a Gaussian disorder of the same mean and variance on either the rungs and the legs. The Gaussian disorder distribution is unbounded in contrast to the bimodal disorder. The mean leg value of both was chosen as $\left\langle J_\nu^{\|} \right\rangle = 0.3$ to allow higher order effects. In subsection 2.4 it was already found for small couplings that rung disorder shows different behaviour when one compares the bimodal and Gaussian distribution. The effect of higher-order terms and the differences between both in the two-triplon sector are looked at. Localization properties in the one- and two-triplon sector will be analysed with the inverse participation ratio. The question arises how big the influence of higher moments than two is on it and can be investigated by considering those two distributions. In subsection 2.4.3 it was found that the DOS is not smooth when dealing with rung disorder. Here the DOS will be calculated for the bimodal and the Gaussian distribution. The possible influence of higher order terms on the DOS of the bimodal distribution and the differences it shows when one compares a continuous with a discrete distribution are of special interest. Also for that question a distribution that is bounded and of similar shape as the bimodal distribution was chosen as a third one to be looked at here. The bounds of it are given by the values of the bimodal distribution. For leg disorder the distribution takes leg values with the probability $P(J^{\|}) \propto (J^{\|} - 0.3)^{10}$. In an analogous way such a distribution was chosen and considered for rung disorder. Those polynom of order 10 distributions have the same mean and almost the same variance as the bimodal and the Gaussian distributions that are examined. The static structure factor does not show significant differences between these three disorder configurations as it mostly depends on the mean of the leg coupling. Good statistics of $R = 500$ samples and system sizes of $N = 500$ were used for both leg and rung disorder in the one-triplon sector to minimize the impact of statistical fluctuations.

4.4.1. Leg disorder

The Gaussian and the bimodal disorder both have a mean leg coupling value of $\left\langle J_\nu^{\|} \right\rangle = 0.3$ and a variance in the leg coupling of $\mathrm{Var}(J_\nu^{\|}) = 0.2^2$. The bimodal distribution is chosen to have vanishing skewness and explicitly can be given by $P(J^{\|} = 0.5) = 0.5$ and $P(J^{\|} = 0.1) = 0.5$. The polynomial distribution is given by the bounds $J_{\mathrm{max}}^{\|} = 0.5$, $J_{\mathrm{min}}^{\|} = 0.1$ and the probability distribution $P(J^{\|}) \propto (J^{\|} - 0.3)^{10}$.

Fig. 4.14 shows the density of states in the one- and two-triplon channels. In the one-triplon part one sees that the Gaussian DOS is smooth and has a tail caused by it being not bounded. The polynomial distribution follows the shape of the Gaussian distribution but has no tail which is obvious since it is bounded. It shows small local maxima at points where the bimodal distribution has high peaks. The bimodal distribution is also mostly smooth but starts to show more and more peaks as the energies get higher than $\omega = 1.2$. One reason for that are higher order effects that play a bigger role for states with most weight on momentum $k = 0$

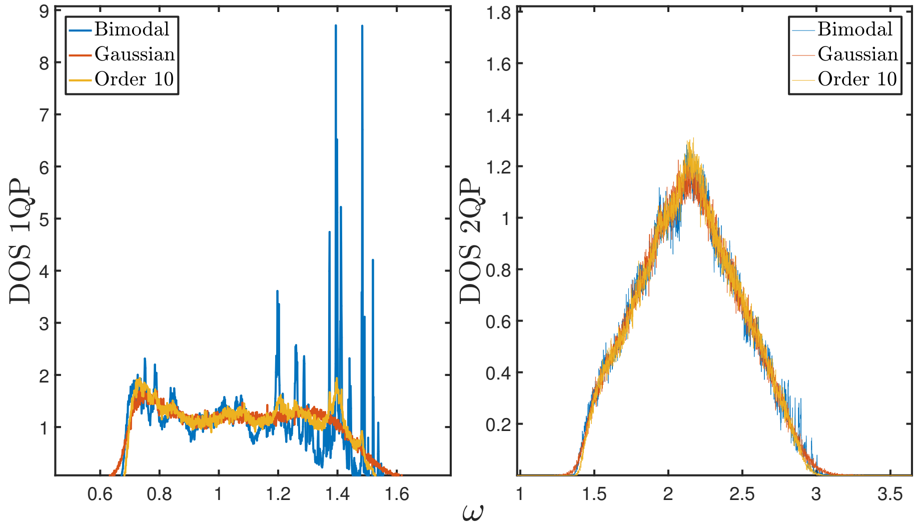

Fig. 4.14: Gaussian leg disorder of $\mathrm{Var}(J_\nu^{\|}) = 0.2^2$ and $\left\langle J_\nu^{\|} \right\rangle = 0.3$ (red curves), a polynomial leg disorder configuration of $J_{\mathrm{max}}^{\|} = 0.5$, $J_{\mathrm{min}}^{\|} = 0.1$ and $P(J^{\|}) \propto (J^{\|} - 0.3)^{10}$ (yellow curves) and a bimodal leg disorder of $P(J^{\|} = 0.5) = 0.5$, $P(J^{\|} = 0.1) = 0.5$ (blue curves) are shown. They hence have the same mean and almost the same variance in the rung distribution (the one of the polynomial distribution is slightly smaller). The left plot shows the DOS for the one triplon energies and was obtained for a system size of $N = 500$, $R = 500$ samples and an energy bin width of $\Delta\omega = 1/1000$.

as was explained in subsection 4.2 and seen in the dynamic structure factor in subsection 4.3.1. Interference effects are stronger in $\mathrm{H}_{\mathrm{eff}}(k, k')$ for the bimodal distribution because phase correlations have to be stronger as only a finite set of values is allowed for the Fourier transform that brings the values of $\mathrm{H}_{\mathrm{eff}}(k, k')$ back to $\mathrm{H}_{\mathrm{eff}}(\nu, \nu')$. A second explanation is that scatterings of the mean dispersion with $\mathrm{H}_{\mathrm{eff}}(k, k')$ thus lead to more local minima and maxima and that this explains the appearance of the peaks in the bimodal case. That the peaks in the DOS of the bimodal configuration are only statistical artefacts can be excluded. A system size of $N = 500$ and $R = 500$ samples were used for the DOS. The energy bin width was $1/1000$. In the two-triplon channel the density of states looks very similar for all three distributions. One can see that the Gaussian still shows a short tail and the bimodal distribution still displays biggest fluctuations. Still, compared to the one-triplon DOS these differences are small. The large amount of states seems to average out the peak structure of the bimodal distribution.

For the same leg disorder configurations the IPR and the IPR_2 were calculated. In the one-triplon case the IPR of the Gaussian distribution is smooth and takes its highest values for highest and lowest energies. These belong to rare values of the Gaussian distribution and thus have most strongly localized eigenfunctions. For all distributions the IPR increases to higher energies. These have biggest weight on momentum $k = 0$. Higher order effects lead to strongest broadening for $k = 0$ and this again explains why the IPR grows towards higher energies. On the other hand the minimum energy and the absolute maximum energy show a decrease in the IPR for the bimodal and the polynomial distribution. Long chains of one value

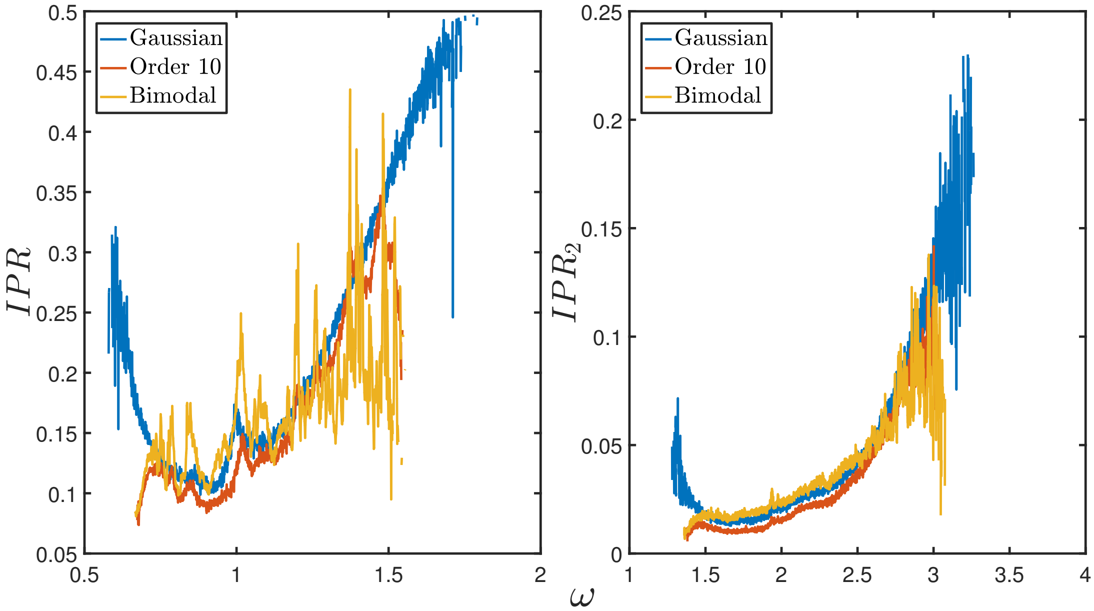

Fig. 4.15: The plots show Gaussian leg disorder of $\mathrm{Var}(J^{\|}_{\nu}) = 0.2^2$ and $\left\langle J^{\|}_{\nu} \right\rangle = 0.3$ (blue curves), a polynomial leg disorder configuration of $J^{\|}_{\mathrm{max}} = 0.5$, $J^{\|}_{\mathrm{min}} = 0.1$, $P(J^{\|}) \propto (J^{\|} - 0.3)^{10}$ and $\left\langle J^{\|}_{\nu} \right\rangle = 0.3$ (red curves) and a bimodal leg disorder of $P(J^{\|} = 0.5) = 0.5$, $P(J^{\|} = 0.1) = 0.5$ (yellow curves). The left plot shows the IPR of the one triplon energy eigenstates and was obtained for a system size of $N = 500$, $R = 500$ samples and an energy bin width of $\Delta\omega = 1/1000$. The right plot shows the generalized inverse participation ratio IPR_2 of the two-triplon energy eigenstates for a system size of $N = 100$, $R = 100$ samples and an energy bin width of $\Delta\omega = 1/1000$. Interestingly it shows a similar behaviour as the IPR.

lead to one of these extreme values and the longer such a chain of consecutive constant values is the lower is the IPR. Another point of small IPR is within the middle of the band close to $\omega = 1$. The IPR varies strongest for the bimodal distribution.

The IPR_2 shows essentially the same features as the IPR. One main difference is that the IPR_2 varies less strongly than the IPR for the bimodal distribution. This is analogous to the behaviour of the one- and two-triplon DOS of the bimodal distribution.

The dynamic structure factor for the three leg disorder configurations is shown in Fig. 4.16. Deviations of the total weight to 1 were smaller than 0.1 % for all disorder configurations. The differences between the three distributions are not small when the dynamic structure factor is convolved with a Lorentzian curve of FWHM of 0.02 as can be seen in Fig. E.6. In Fig. 4.16 one sees the same data but now binning with a width of $1/1000$ is used. Unsurprisingly in the plot with binning the differences are bigger since fluctuations of the DOS of the bimodal distribution remain persistent. They are largest at $k = 0$. As already mentioned higher order effects are responsible for that. There are also differences between the bimodal and the polynomial distribution. These are also strongest at $k = 0$ where only for the bimodal disorder regions of vanishing DOS are visible.

In the two-triplon channel one difference is that the shadow of the continua has a different shape. The disorder widened bound state splits into two stripes at $k = \pi$ for the bimodal case. This can not be seen for the two other distributions. Differences between the convolved dynamic structure factor (Fig. E.6) and the one with binning (Fig. 4.16) are smaller than in the two-triplon sector. On the one hand one can explain that with the smooth DOS all three distributions show in the two-triplon sector. On the other hand it is more important how smooth the density of states of bound states is and one can propose that this density does not have points of vanishing DOS because differences between binned and convolved structure factor are small.

The conclusion is that leg disorder of the same mean and variance and with vanishing skewness does not seem to depend strongly on higher moments of the probability distribution. There are big differences in the one-triplon density of states, especially between the Gaussian and the bimodal distribution. The polynomial distribution shows some of the features of the bimodal distribution but is behaves smooth for quantities like the IPR and the DOS. Still, when the dynamic structure factor gets convolved like in an experiment these differences become less substantial and the shape is qualitatively similar for all three distributions.

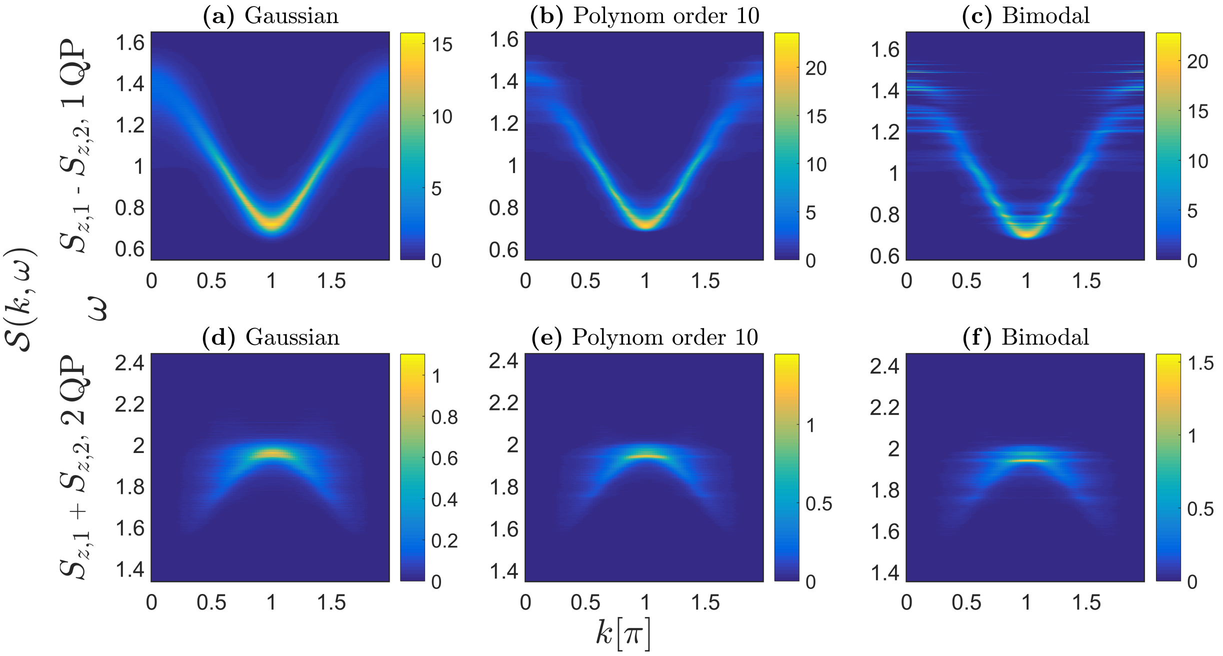

Fig. 4.16: All plots were obtained by system sizes of $N = 100$, $R = 100$ samples and bin width of $1/1000$ and show the dynamic structure factor of the antisymmetric observable in the one-triplon and the symmetric observable in the two-triplon sector.

(a) and (d): Gaussian leg disorder of $\mathrm{Var}(J^{\|}_{\nu}) = 0.2^2$ and $\left\langle J^{\|}_{\nu} \right\rangle = 0.3$.

(b) and (e): Polynomial leg disorder of $J^{\|}_{\max} = 0.5$, $J^{\|}_{\min} = 0.1$, $P(J^{\|}) \propto (J^{\|} - 0.3)^{10}$ and $\left\langle J^{\|}_{\nu} \right\rangle = 0.3$.

(c) and (f): Bimodal leg disorder of $P(J^{\|} = 0.5) = 0.5$, $P(J^{\|} = 0.1) = 0.5$.

4.4.2. Rung disorder

Next continuous rung disorder shall be compared to bimodal rung disorder. The Gaussian disorder is chosen as $\mathrm{Var}(J^{\perp}_{\nu}) = 0.2^2$, $\langle J_{\perp} \rangle = 1$ and $J_{\parallel} = 0.3$. Consequently the bimodal disorder that is compared with is of the form $P(J^{\perp} = 1.2) = 0.5$, $P(J^{\perp} = 0.8) = 0.5$ and $J^{\parallel} = 0.3$ and the polynomial disorder follows $P(J^{\perp}) \propto J^{\perp 10}$, has a leg coupling of $J^{\parallel} = 0.3$ and is bounded by $J^{\perp}_{\mathrm{max}} = 1.2$ and $J^{\perp}_{\mathrm{min}} = 0.8$.

In Fig. 4.17 the DOS for the one- and two-triplon channel is plotted for these three distributions. In the one triplon channel the DOS of the Gaussian distribution is smooth like in the leg case. Also the DOS of the polynomial distribution looks similar. It still shows local maxima when the bimodal distribution shows big peaks. A big change to the leg case can be seen for the bimodal distribution. One can make out four regions of vanishing DOS. The fluctuations of the bimodal DOS are much stronger than in the leg case. For the leg disorder case the difference between the polynomial and the bimodal distribution was not big but here the differences are immense. The DOS of the polynomial distribution looks more similar to that of the Gaussian. That the peaks in the DOS of the bimodal configuration are only statistical artefacts was ruled out by using $R = 500$ samples. System size was $N = 500$ and energy bin width $1/1000$.

The DOS for two-triplon states looks still remarkably similar for all three distributions. The Gaussian shows a longer tail and a smaller maximum value and the bimodal DOS is fluctuating stronger also in the two-triplon case. If these fluctuations will average out when more samples are used is unclear. Like in the leg case the behaviour of the one- and two-triplon DOS changes drastically from a distribution with many peaks to a nearly smooth curve.

The inverse participation ratio and the IPR_2 is plotted for all three rung disorder configurations in Fig. 4.18. The average IPR is bigger than in the leg disorder case. Hardly any energy dependence can be seen for the bimodal and the rung disorder. The IPR goes down at the edges of regions with vanishing DOS for the bimodal distribution and at the maximum and minimum value for both the bimodal and the polynomial distribution. This behaviour was already seen in the leg disorder case. The values of the polynomial and the bimodal distribution lie very close. One can see the same behaviour of the Gaussian distribution for smallest and highest energies as in the leg disorder case. The value of the IPR increases towards those energies. In the two-two triplon case the IPR_2 of the bimodal and polynomial distribution seems to be slightly smaller.

The dynamic structure factor of the symmetric observable in the two-triplon and the antisymmetric observable in the one-triplon channel is shown for the three rung disorder configurations in Fig. 4.19 with a binning of $1/1000$ and in Fig. E.7 with a Lorentzian broadening of FWHM of 0.02. Deviations of the total weight of both observables to 1 were around 0.1 %. Especially in the one-triplon sector the difference between the convolved and the binned plots is big since the DOS has many regions of vanishing DOS there for the bimodal disorder. For the Gaussian disorder however one can not see substantial differences. This is again caused by the DOS that is smooth in the Gaussian case. For both the convolved and the binned plots the behaviour of the Gaussian distribution is very different to that of the two others especially in the two-triplon sector. There one can not see any dispersion-like shape at all anymore but only a smeared

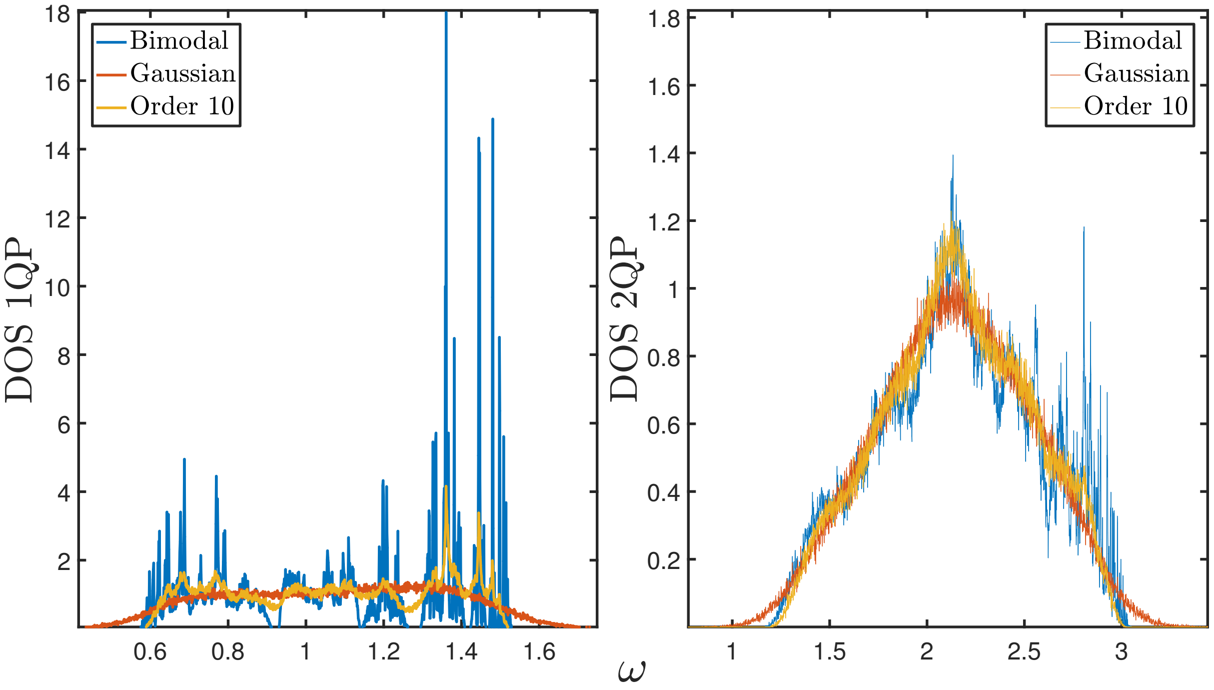

Fig. 4.17: The plots show Gaussian rung disorder of $\mathrm{Var}(J_\nu^\perp) = 0.2^2$, $\langle J_\perp \rangle = 1$ and $J_\| = 0.3$ (red curves), a disorder with a polynomial probability distribution for the rung $P(J^\perp) \propto J^{\perp\,10}$ and $J^\| = 0.3$ and $J^\perp_{\mathrm{max}} = 1.2$, $J^\perp_{\mathrm{min}} = 0.8$ (yellow curves) and a bimodal rung disorder of $P(J^\perp = 1.2) = 0.5$, $P(J^\perp = 0.8) = 0.5$ and $J^\| = 0.3$ (blue curves). The left plot shows the DOS for the one triplon energies and was obtained for a system size of $N = 500$, $R = 500$ samples and an energy bin width of $\Delta\omega = 1/1000$. The right plot shows the DOS for the two triplon energies and was obtained for a system size of $N = 100$, $R = 100$ samples and an energy bin width of $\Delta\omega = 1/1000$.

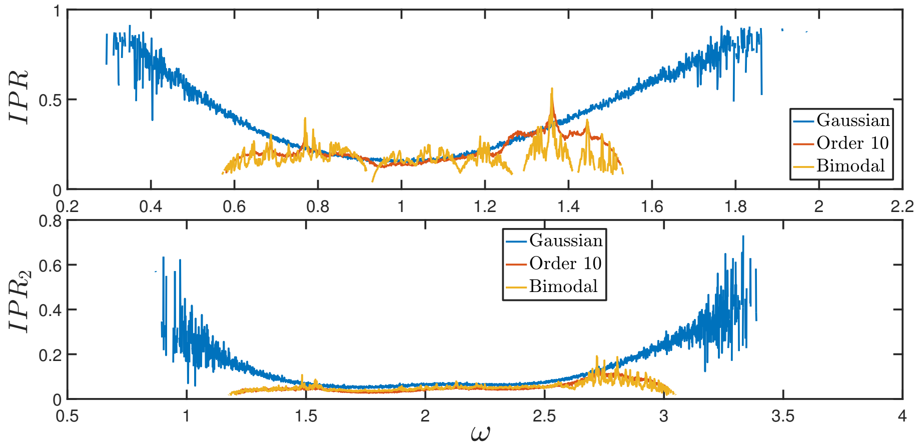

Fig. 4.18: The plots show Gaussian rung disorder of $\mathrm{Var}(J_\nu^\perp) = 0.2^2$, $\langle J_\perp \rangle = 1$ and $J_\parallel = 0.3$ (blue curves), a disorder with a polynomial probability distribution for the rung $P(J^\perp) \propto J^{\perp\,10}$ and $J^\parallel = 0.3$ and $J^\perp_{\mathrm{max}} = 1.2$, $J^\perp_{\mathrm{min}} = 0.8$ (red curves) and a bimodal rung disorder of $P(J^\perp = 1.2) = 0.5$, $P(J^\perp = 0.8) = 0.5$ and $J^\parallel = 0.3$ (yellow curves). The upper plot shows the IPR of the one triplon energy eigenstates and was obtained for a system size of $N = 500$, $R = 500$ samples and an energy bin width of $\Delta\omega = 1/1000$. The lower plot shows the generalized inverse participation ratio IPR_2 of the two-triplon energy eigenstates for a system size of $N = 100$, $R = 100$ samples and an energy bin width of $\Delta\omega = 1/1000$. It essentially shows the same features as the IPR but with smaller values.

blot with biggest intensity in the center. Differences in the polynomial and the bimodal case are also getting bigger (see Fig. 4.19 (b) and (c). Nevertheless their shapes are still much more similar than they are to the Gaussian distribution. The bimodal rung disorder leads to a finer structure with more fluctuations in the intensity for fixed momentum. This effect could already be seen in the DOS. Higher order effects together with the stronger phase correlations in $\mathrm{H_{eff}}(k, k')$ for the bimodal disorder case could be an explanation for that. The discreteness of the bimodal disorder is important for the strong intensity fluctuations and the regions of vanishing DOS and following from that vanishing dynamic structure factor weight. Deviations between the three distributions get even bigger as one looks at the two-triplon case. While the bimodal rung disorder leads to a splitting into at least two bands nothing tears apart in the polynomial disorder case (see Fig. 4.19 (d) and (e)). In the bimodal case the lower bound state is still separated and easy to see. For the polynomial disorder one can also see an intensity maximum at a similar energy but this intensity is distributed over a wider energy width.

The dynamic structure factor of the symmetric observable for Gaussian rung disorder in Fig. 4.19 (d) hardly shows any structure. The dispersion like structures of bound states in the two-triplon sector one often finds can not be seen anymore. This motivates to compare with a calculation where two-triplon interactions were set to zero since bound state signatures can not be resolved anymore anyway. In Fig. E.8 one finds the so obtained dynamic structure factor and indeed the shapes look quite similar. The biggest effect of the two-triplon interactions that can be identified is a negative energy-offset that shifts the whole structure to smaller energies. The conclusion here is that for rung disorder only taking into account the mean and variance

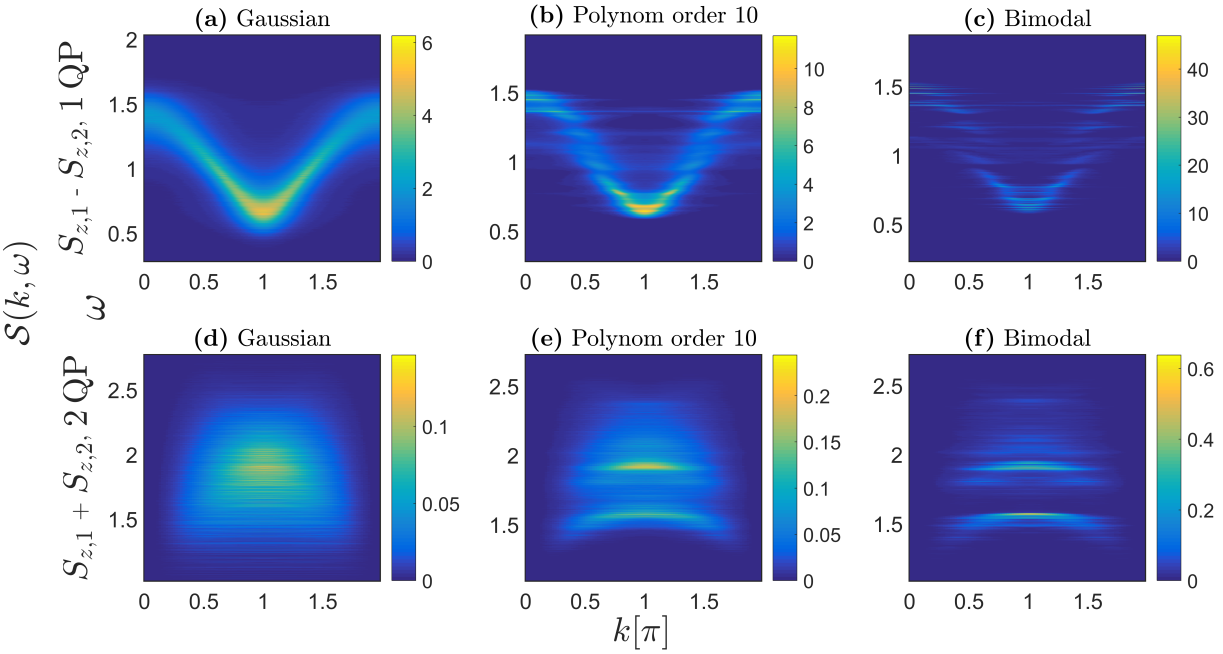

Fig. 4.19: All plots were obtained by system sizes of $N = 100$, $R = 100$ samples and energy bin width of $1/1000$ and show the dynamic structure factor of the antisymmetric observable in the one-triplon sector (upper row) and the symmetric observable in the two-triplon sector.
(a) and (d): Gaussian rung disorder of $\mathrm{Var}(J_\nu^\perp) = 0.2^2$, $\langle J_\perp \rangle = 1$ and $J_\| = 0.3$.
(b) and (e): Polynomial probability distribution for the rung $P(J^\perp) \propto J^{\perp\,10}$ and $J^\| = 0.3$ and $J^\perp_{\text{max}} = 1.2$, $J^\perp_{\text{min}} = 0.8$.
(c) and (f): Bimodal rung disorder of $P(J^\perp = 1.2) = 0.5$, $P(J^\perp = 0.8) = 0.5$ and $J^\| = 0.3$.

of it is not enough. The differences between the Gaussian rung disorder and the bimodal rung disorder are enormous even if one considers the dynamic structure factor convolved with the 0.02 FWHM Lorentzian. This a big difference to the leg disorder where we saw only minor differences for the convolved dynamic structure factor.

4.5. Correlated rung-leg disorder in BPCB$_x$C$_{1-x}$

The materials $(\mathrm{C_5D_{12}N})_2\mathrm{CuCl_4}$ (BPCC) and $(\mathrm{C_5D_{12}N})_2\mathrm{CuBr_4}$ (BPCB) can be very well modelled as quasi one-dimensional antiferromagnetic two-leg ladders. Starting with BPCC one can obtain the disordered material $(\mathrm{C_5D_{12}N})_2\mathrm{Cu}(\mathrm{Cl}_4^{1-x}\mathrm{Br}_4^x)$ via doping with bromine atoms. x is the total concentration of bromine atoms. The strength of rung and leg couplings depends on the spatial distribution of chlorine and bromine atoms in the lattice. The situation is illustrated in Fig. 4.20 which was taken from the PhD thesis of Simon Ward [13]. There are two exchange pathways between four halogens that determine the rung coupling and one exchange pathway between two halogens that determines the leg coupling strength. In Fig. 4.20 (b) the atoms are labelled by 1, 2 and 3 depending on what their effect on rung and leg coupling is. From

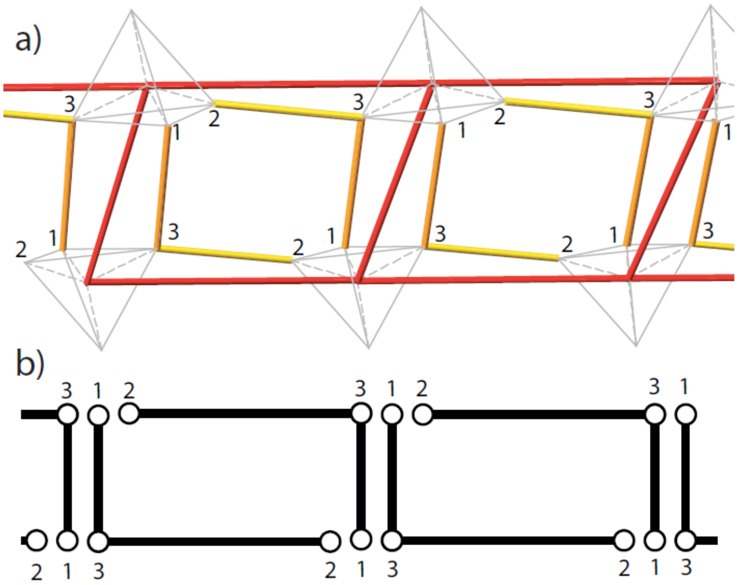

Fig. 4.20: The scheme is taken from the PhD of Simon Ward [13]. In (a) the four bromine or chlorine atoms of each site are shown and also on which of them leg and rung couplings depend on.

(b) The exchanges between different chlorine and/or bromine atoms of (a) are presented as bonds. The strength of the rung coupling depends on the four atoms labels by 1 and 3. The atoms labelled with a 2 solely affect the leg couplings. Leg and rung couplings are correlated by the fact that both depend on atoms labelled by 3.

Fig. 4.20 (a) one can see that only three of the four chlorine or bromine atoms of one molecule influence the couplings of a certain ladder segment. Atoms that are on a site labelled by 2 only have influence on the leg coupling. Those labelled by 3 have influence on both leg and rung couplings. Due to them there is correlation between $J^{\|}_{\nu}$ and $J^{\perp}_{\nu}$. Finally the ones labelled with a 1 only influence the rung couplings. In the following it is assumed that there is no chemically induced strain or crystal strain and the scaling of the total exchange is linear in the number of bromine atoms in the exchange pathways involved. Introducing the six Bernoulli processes

$$I^{1,2,3}_{\nu,(\mathrm{up},\mathrm{down})} \tag{4.2}$$

that either take the value 1 with probability x the concentration of chlorine atoms and the value 0 with the probability $1-x$ the leg and rung couplings can then be given as

$$\begin{aligned}
J^{\perp}_{\nu} &= \left(3.42 + 2.345\left(I^{1}_{\nu,\mathrm{up}} + I^{1}_{\nu,\mathrm{down}} + I^{3}_{\nu,\mathrm{up}} + I^{3}_{\nu,\mathrm{down}}\right)\right) \mathrm{k_B\,K} \\
J^{\|}_{\nu,1} &= \left(1.34 + 1.03\left(I^{2}_{\nu,\mathrm{up}} + I^{3}_{\nu+1,\mathrm{up}}\right)\right) \mathrm{k_B\,K} \\
J^{\|}_{\nu,2} &= \left(1.34 + 1.03\left(I^{3}_{\nu,\mathrm{up}} + I^{3}_{\nu+1,\mathrm{up}}\right)\right) \mathrm{k_B\,K}
\end{aligned} \tag{4.3}$$

[13]. It is important that rung and leg couplings are correlated. This makes it impossible that on one supersite the rung coupling of the pure chlorine and the leg coupling of the pure bromine are taken and thus limits the ratio of leg and rung couplings. With this modelling of the disordered material $(\mathrm{C_5D_{12}N})_2\mathrm{Cu}(\mathrm{Cl}_4^{1-x}\mathrm{Br}_4^{x})$ the dynamic structure factor is calculated for both the antisymmetric and symmetric observable in the one- and two-triplon sector. The deviation of the total weight of both observables to 1 was 1 % or less for all concentrations. It thus is much smaller than in the disorder configuration of subsection 4.3.3 because of the correlation between rung and leg couplings. The static structure factor for the concentrations of $x = 0, 0.2, 0.4, 0.6, 0.8, 1$ can be found in Fig. E.9. The weight of the antisymmetric observable in the one-triplon and the symmetric in the two-triplon sector at $k = \pi$ increases with the concentration of chlorine. It thus behaves the same way the mean effective coupling ratio would behave. For the disorder-induced observables, i.e. the symmetric in the one-triplon and the antisymmetric in the two-triplon sector, the weight increases similarly but the antisymmetric in the two-triplon sector shows bigger weight for $x = 0.4$ than for $x = 0.2$. Both their dispersive behaviours are quite flat with difference that the symmetric observable in the one-triplon sector goes down to zero at $k = 0$ due to it commuting with the Hamiltonian for that momentum (see subsection 2.3 for that).

4.5.1. One-triplon dynamic structure factor

Figure 4.21 shows the one-triplon dynamic structure factor of the symmetric and antisymmetric observable for bromine concentrations of $x = 0, 0.2, 0.4, 0.6, 0.8, 1$. One interesting effect for the antisymmetric observable at $k = 0$ is that for concentrations of $x = 0.2$ we see several peaks while for $x = 0.8$ there is only one wider peak. First it is not surprising to see many peaks for $x = 0.2$ since the rung coupling can take five different values. However, this is also true for $x = 0.8$. The difference is that the absolute value of the leg coupling is much bigger in the pure bromine case and also in the $x = 0.8$ case compared to the $x = 0.2$ case. The effect of the rung disorder - the increase due to an exchange of chlorine by bromine is constant - is thus stronger on the $x = 0.2$ case and leads to a stronger splitting. At $k = \pi/2$ we see a similar though less pronounced difference between the $x = 0.8$ and the $x = 0.2$ case. This is not surprising since such splitting tendencies are usually weaker at $k = \pi/2$. At momentum $k = \pi$ the situation is different to $k = 0$. The $x = 0.8$ system now shows several peaks and the $x = 0.2$ system has one pronounced peak. The change of the observable weight with the ratio of leg and rung coupling is made responsible for that. At momentum $k = \pi$ this ratio has the biggest influence on the observable weight and this ratio is bigger for the $x = 0.2$ material what could lead to a more pronounced peak.

As always the weight of the symmetric observable at $k = 0$ is also zero here in the one-triplon case. For $k = \pi/2$ and $k = \pi$ one can not detect a change in the shape of the symmetric observable. Only the weight changes slightly. The static structure factor of this observable is a quite flat curve (see Fig. E.9). Intensities are small but not zero. The weight increases from $x = 0.8$ to $x = 0.2$. This is related to the increase in the ratio of leg and rung couplings and the behaviour of the static structure with this increase (see again Fig. E.9). The decreasing intensity with x in Fig. 4.21 (d) and (e) can be explained by that. Fig. 4.22 shows contour

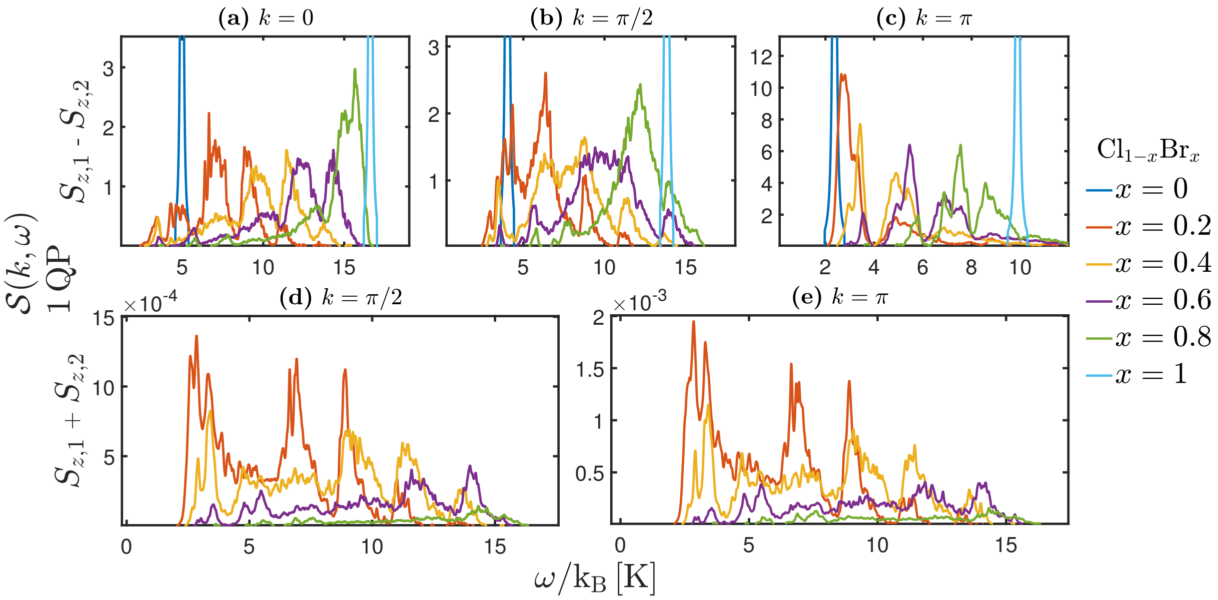

Fig. 4.21: Plots show the dynamic structure factor for the symmetric and antisymmetric observable in the one-triplon channel. For that $R = 100$ disorder samples of size $N = 100$ were averaged and after that broadened with a Lorentzian curve of FWHM of $0.08\,\mathrm{k_B K}$. The ratio of bromine atoms increases in steps of 20% from 0 to 1. The curves show several peaks belonging to different rung-rung combinations of bromine and chlorine atoms.

plots for the antisymmetric observable for $x = 0, 0.2, 0.4, 0.6, 0.8, 1$. In Fig. E.10 also a contour plot with the same colour scale for $x = 0.2, 0.4, 0.6, 0.8$ can be seen. The density of states of the one-triplon energies is shown in Fig. E.12. Interesting is that already small disorder widens the energy range immensely when compared to the pure cases. Also maxima for the different possible rung configurations appear. The more likely the rung configuration is the bigger the DOS is for the energies belonging to that rung configuration. Fig. E.13 shows the inverse participation ratio. The first thing to notice is that its value is quite high. Due to the strong disorder on the rungs the states are strongly localized for values of $x = 0.2$ or $x = 0.8$ already. The IPR increases towards the rarer rung configurations, e.g. for high chlorine concentrations towards rung configurations build out of mainly bromine. It also shows oscillating behaviour that could be caused by dispersive effects within one region of a particular rung configuration.

4.5.2. Two-triplon dynamic structure factor

In Fig. 4.23 the two-triplon dynamic structure factor is shown for different momenta and concentrations of $x = 0, 0.2, 0.4, 0.6, 0.8, 1$. The antisymmetric observable shows only small intensities but is not zero. The configurations of $x = 0.4$ and of $x = 0.2$ show the biggest weights and several peaks. These peaks belong to different rung configurations. The higher the concentration of bromine becomes the smaller the intensities get. The intensities shift to higher

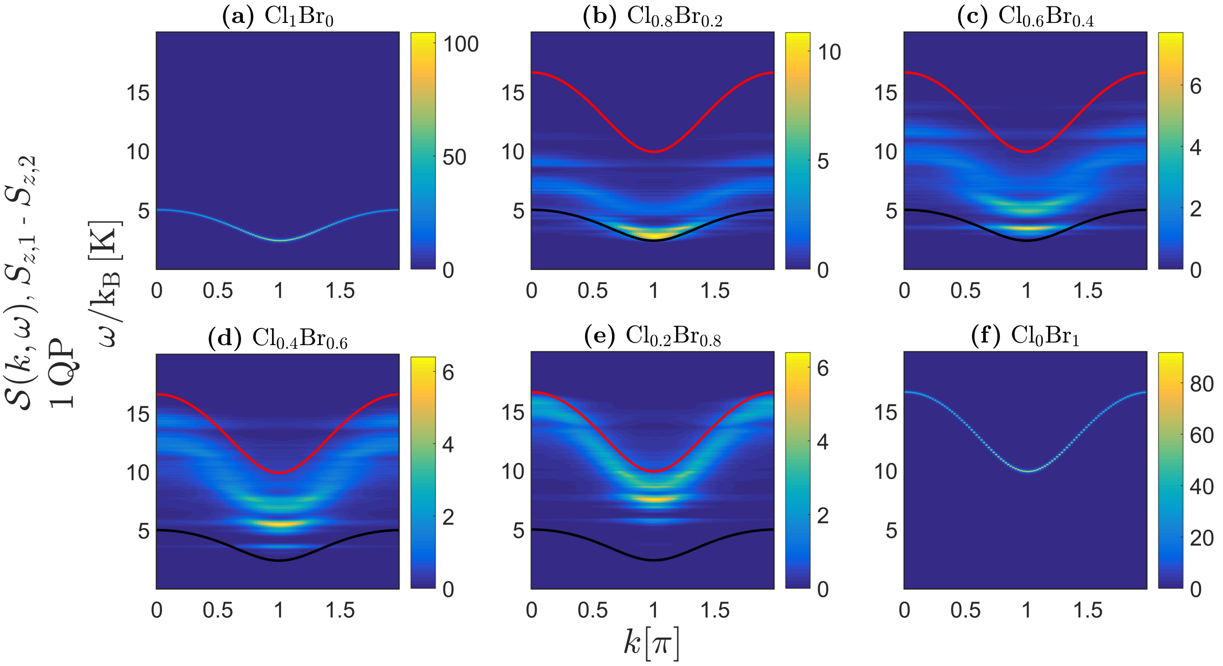

Fig. 4.22: All plots were obtained by system sizes of $N = 100$, $R = 100$ samples and FWHM of the Lorentzian broadening of $0.08\,\mathrm{k_B\,K}$ and show the dynamic structure factor of the antisymmetric observable in the one-triplon sector.
(a)-(f): The ratio of bromine atoms increases in steps of 20% from 0 to 1. The red curve shows the pure bromine dispersion and the black one the pure chlorine dispersion.

energies as k is increased to π. The change in behaviour with rising bromine concentrations could have its reason in the value of $\sigma(J_\nu^{\|})/\left\langle J_\nu^{\|}\right\rangle$. This value is bigger for $x = 0.2$ than for $x = 0.8$ because the absolute value of the chlorine leg coupling is more than twice as small as that of the pure bromine case. In contrast to the behaviour in the bimodal leg disorder subsection 4.3.1 the peaks here are at different energies for different momenta. This is an indicator for the observable to inject two triplons that are not next-neighbours with a substantially bigger amplitude. Indeed the static structure factor in Fig. E.9 (c) shows a more dispersive behaviour than the one for the bimodal leg disorder in Fig. 4.6 (c).
At momentum $k = \pi$ the symmetric observable shows two quite sharp bound state peaks for $x = 0.2$. For all concentrations several peaks can be seen which belong to different rung configurations. Because there are 5 different rung values 15 possible combinations of rung values can be taken of two rungs. This leads to a splitting like in the bimodal rung disorder case. For the splitting however it is only important what the sum of the two rung values is and so there are 9 different rung configurations that could lead to distinct two-triplon energy bands. The sum of the two rung couplings is equidistant in the number of bromine atoms of the two rungs. On the other hand the energy range increases with the number of bromine atoms. Thus those different rung configurations are less well separated or overlap for rung configurations with many bromine atoms. Biggest separation and sharpest peaks are expected for a rung configuration of 8 or 7 chlorine atoms. This peaks will only be seen if

such configurations occur often enough. Thus high concentrations of chlorine are needed, i.e. $x = 0.2, 0.4$. Consistent with that when the concentration of bromine gets increased peaks at $k = \pi$ broaden more and more. For $k = \pi/2$ two peaks with high intensity appear for $x = 0.2$. These are probably peaks from bound states and it seems that they can be distinguished easier from the continuum due to disorder. The other behaviour at $k = \pi/2$ is similar to that at $k = \pi$. That finite-size effects can be discarded in the disordered case was checked by considering the finite-size scaling of the inverse participation ratio. For the non-disordered case with only chlorine atoms one can still see oscillations caused by finite-size effects.

In Fig. E.12 the two-triplon DOS is also shown. One global maximum can be seen for each concentration. On the way to this global maximum small local maxima corresponding to different rung configurations can also be noticed. The energy range of the disordered materials is much wider than that of the pure cases and the DOS shifts from the pure chlorine energies to that of bromine as the concentration of bromine gets increased.

In Fig. E.13 also the generalized inverse participation ratio for two triplons is plotted. It displays the same features as the IPR for one-triplon states but is smoother. Remarkable are the quite high values of above 0.5 that are reached. The two-triplon dynamic structure factor of the symmetric observable is also shown as a contour plot in Fig. 4.24. In the lowest band of the concentration $x = 0.2$ - that is well separated from the other bands - one can see a bound state that has survived disorder. The separation of bands is stronger because as already mentioned changes in the values of $J_\nu^\perp$ are constant but the absolute value of $J_\nu^\parallel$ is smallest for only chlorine atoms. A two-triplon contour plot of the symmetric observable for $x = 0.2, 0.4, 0.6, 0.8$ with same colour scale for all concentrations can be seen in Fig. E.11.

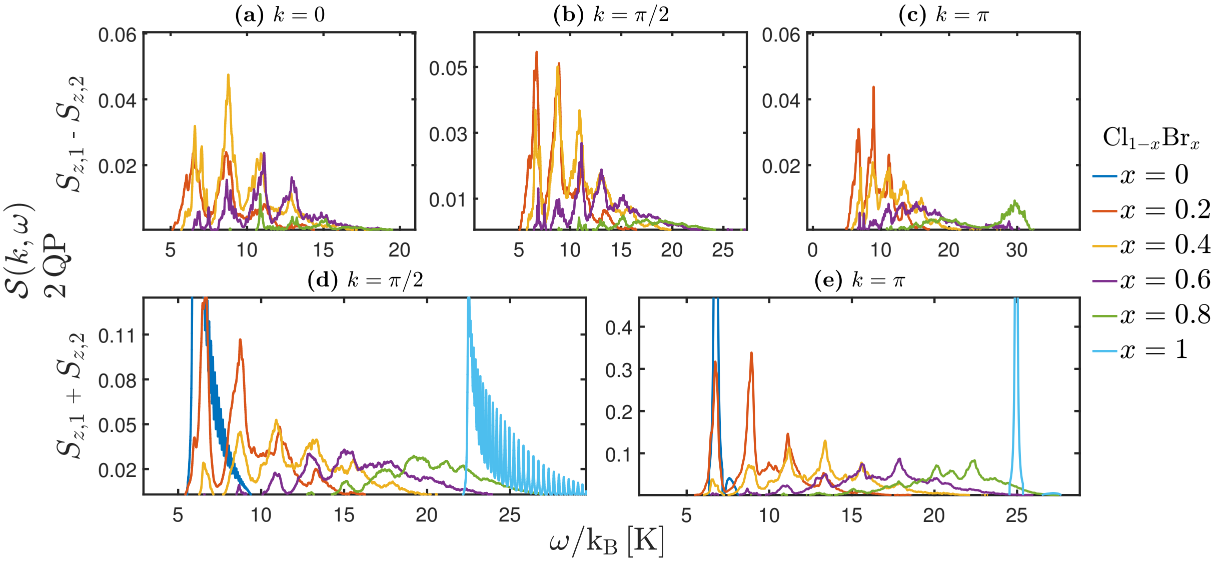

Fig. 4.23: Plots show the dynamic structure factor for the symmetric and antisymmetric observable in the two-triplon channel. For that $R = 100$ disorder samples of size $N = 100$ were averaged and after that broadened with a Lorentzian curve of FWHM of $0.08\,\mathrm{k_B K}$. The ratio of bromine atoms increases in steps of 20% from 0 to 1. Not only for the symmetric but also for the antisymmetric observable several peaks can be seen which belong to bound states.

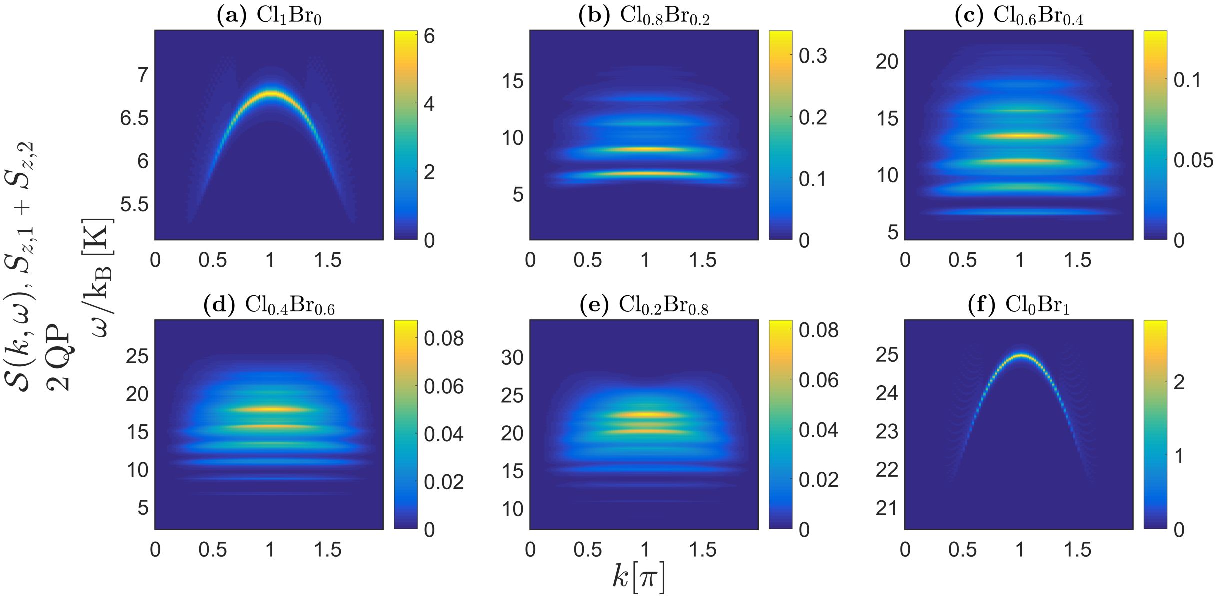

Fig. 4.24: All plots were obtained by system sizes of $N = 100$, $R = 100$ samples and FWHM of the Lorentzian broadening of $0.08\,\mathrm{k_B}\,\mathrm{K}$ and show the dynamic structure factor of the symmetric observable in the two-triplon sector.

4.5.3. Instrumental resolution convolved dynamic structure factor

The way BPCB$_x$C$_{1-x}$ is modelled here should lead to a dynamic structure factor that can be observed in experiment if doping does not induce chemical strain or crystal strain and the scaling of the total exchange is linear in the number of bromine atoms [13]. It is thus interesting to see how the dynamic structure factor would look like when convolved with instrumental resolution. It is not totally clear what the value of this resolution is. One of the data points in the PhD thesis of Simon Ward who did measurements on BPCB$_x$C$_{1-x}$ in the presence of a $15\ \mathrm{T}$ magnetic field showed one of $0.1\,\mathrm{meV} \approx 1.16\,\mathrm{k_B K}$. For the Lorentzian curve used to convolve the dynamic structure factor this value was used as FWHM. Due to the strong rung disorder the localization lengths in BPCB$_x$C$_{1-x}$ are very small. A system size of $N = 40$ showed hardly any finite-size effect anymore. This system size was used to obtain very good statistics of 11000 samples not only in the one- but also in the two-triplon sector. The plots of the so obtained dynamic structure factor can be seen in Fig. 4.25 for several concentrations of bromine. The standard deviation of these data can be assumed to be less than 1 %. The features are similar to the ones discussed before. Less details can be seen because the width of the Lorentzian is more than 10 times bigger. Quite remarkable is that despite this low instrumental resolution one can still see clear signatures of two-triplon bound state peaks for the symmetric observable in the two-triplon channel if the concentration of bromine is not too big. For $x = 0.2$ two sharp peaks are there for the three momenta $k = \pi/4, \pi/2, \pi$. They belong to the two-triplon rung configurations of either eight or seven chlorine exchange atoms. This is remarkable since it not only shows that bound states remain to be very important in the presence of disorder but also because this is something easy to identify in an experiment.

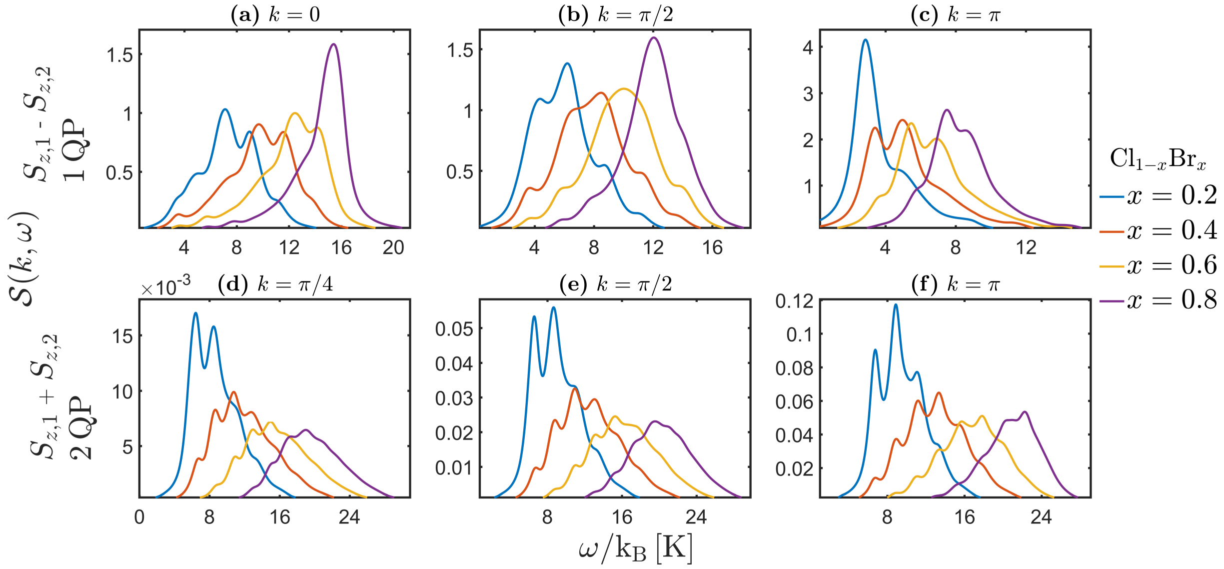

Fig. 4.25: The plot shows the dynamic structure factor of the antisymmetric observable for different concentrations x of bromine in BPCB$_x$C$_1-x$ in the one-triplon and of the symmetric observable in the two-triplon sector. Making use of the short localization lengths a system size of only $N=40$ was enough to discard finite-size effects. $R=11000$ samples were taken to obtain an accuracy of 1 % for the dynamic structure factor when folded with a Lorentian of FWHM of $0.1\mathrm{meV}\approx1.16\,\mathrm{k_B K}$ as is seen in the figure.

5. Conclusions and outlook

A general framework for calculating the dynamic structure factor of the dimerized spin-$1/2$ chain and the Heisenberg spin-$1/2$ two-leg ladder in the presence of disorder was given. For that the pCUT method and so-called white graph expansions were used [34]. This way numerical high-precision results can be obtained for large finite systems if the strength of the perturbation lies within the convergence radius of the perturbative expansion. All sorts of disorder can be treated within the framework. One- and two-triplon properties were examined. This goes beyond all other calculations of dynamical correlations done so far in the disordered case since two quasi-particle calculations did not exist so far. Apart from dynamical correlations of inelastic neutron scattering observables also the density of states and the inverse participation ratio was calculated. This can also be done with high precision using the pCUT method. All states were found to be localized in the presence of disorder. The inverse participation ratio that scales with the inverse localization length shows larger values for rung disorder and grows with the disorder strength. Two-triplon states are found to be localized in the sense that almost all the weight of their eigenfunctions sits on a finite number of two-triplon position states. The mean of the absolute squared effective Hamiltonian in momentum space could be derived analytically by means of the cross-correlation theorem. Its values have proven useful for a qualitative analysis of the lifetime of momentum modes in dependence of disorder using the Born approximation of the self-energy. Bimodal leg and rung disorder were compared numerically and showed the same qualitative behaviour of lifetimes as expected theoretically. The bimodal disorder configurations were compared with a Gaussian disorder on leg and rung. While for the Lorentzian convolved dynamic structure factor Gaussian disorder on the leg showed similar features as bimodal disorder for Gaussian rung disorder the dynamic structure factor is very different especially for two-triplon weights. The density of states of bimodal rung disorder and also of strong enough bimodal leg disorder configurations was found not to converge to a smooth distribution in the one-triplon sector. This is in agreement with analytic first-order degenerate perturbation theory calculations that have also been performed. In contrast to that Gaussian disorder always shows a smooth density of states. Sharp two-triplon bound states were found to get a finite lifetime but can still be separated as peaks from the continuum for some sorts of disorder. Due to momentum broadening of the bound states they form peaks that lie within the continuum for some momenta.

The dynamic structure factor calculations are relevant for material classes like $\mathrm{BPCB}_x\mathrm{C}_{1-x}$ that are modelled by a disordered Heisenberg two-leg ladder as the one investigated. Quantitatively trustful calculations with the couplings of that material were done and it was found that two-triplon bound states might survive not to big concentrations of bromine atoms. It is looked forward to a comparison of this data with inelastic neutron measurements on the material. Another interesting task for the future could be to calculate spectral densities of other than inelastic neutron scattering observables, e.g. observables relevant for Raman scattering. The effect of disorder on those observables for the here discussed models is not known in detail yet but easy to calculate within the scheme developed in this thesis and could be of experimental relevance. Pyrazine-base compounds are potential candidates for zig-zag ladders [13]. Randomness in such materials would combine disorder with frustration. Calculations thereof are called for since the consequences of the interplay of disorder and frustration are not only interesting from a theoretical viewpoint but can become experimentally accessible in the future.

As extrapolation scheme here optimised perturbation theory was used. It was implemented in such a way that an OPT parameter can be assigned to every local site. With a global OPT parameter chosen by comparison with extrapolants of mean expressions singularities could already be regulated. More desirable would be local OPT parameters for every site. No criterion was found for the best way of choosing them however. Finding an appropriate local criterion for extrapolation could thus be another future goal. Several ground state averages were calculated. For the future one interesting question is what these averages can tell about the nature of a quantum phase transition in the presence of disorder. As long as the disorder is strong enough in one dimension finite-size effects are not a big problem. When going to higher dimensions this could change dramatically In one dimension almost all states are localized in a disordered lattice. This is not true anymore for two and three dimensions. It seems likely that finite-size effects become more important when dealing with extended states. For leading order calculations here already results in the thermodynamic limit could be achieved. A hard but interesting objective could be to generalize the self-consistent methods for the Green's functions so that the higher-order terms of the pCUT can be incorporated. Generally calculations that are done directly in momentum space would be desirable.

Appendices

A. Disordered dimerized chain

Here the effect of bimodal disorder on the dynamic structure factor of the dimerized chain in the one- and two-triplon sector is investigated. At first the results for the non-disordered dimerized chain are summarized in short. Fig. A.1 shows the dispersion curves for the two coupling ratios 0.15 and 0.4. The values of the maxima (minima) increase (decrease) with rising coupling ratio. The static structure factor for these ratios and disordered configurations is shown in Fig. A.3. The one-triplon weights only change slightly. The two-triplon weights increase with the mean coupling ratio.

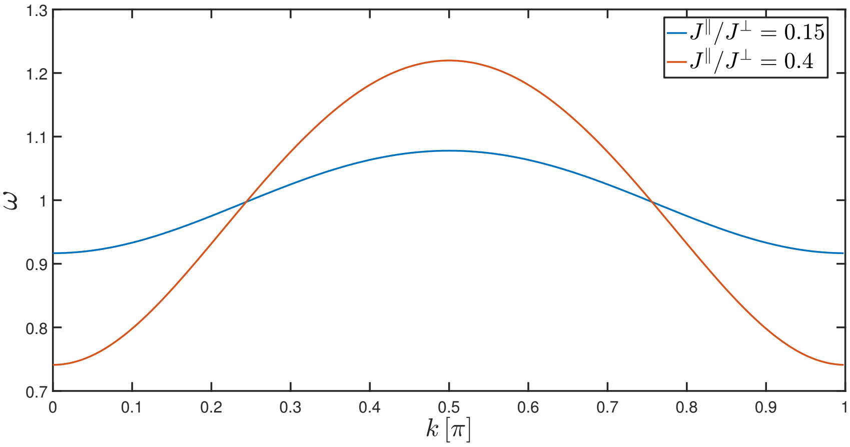

Fig. A.1: Dispersion curves of the dimerized chain for the two different coupling ratios $J^{\|}/J^{\perp} = 0.15$ (blue) and $J^{\|}/J^{\perp} = 0.4$ (red) are shown.

The influence of $\mathcal{H}_2$ on two-triplon properties is smaller for the dimerized chain when one compares with the two-leg ladder. This can be seen in Fig. A.2. There appear bound states but they carry only a small part of the weight. The continuum remains to be the dominant contribution. $\mathcal{H}_2$ shifts the weight in the continuum to smaller energies. The biggest difference is that more weight is contained in the two-triplon sector for $J^{\|}/J^{\perp} = 0.4$ and that the lower band edge is found for smaller energies. Bound states show biggest weight at around $k = \pi/2$ and their weight increases with the coupling ratio. This increase is however not expected to be significantly stronger than the increase of the static structure factor. Qualitative differences between the $J^{\|}/J^{\perp} = 0.15$-case and the $J^{\|}/J^{\perp} = 0.4$-case are small.

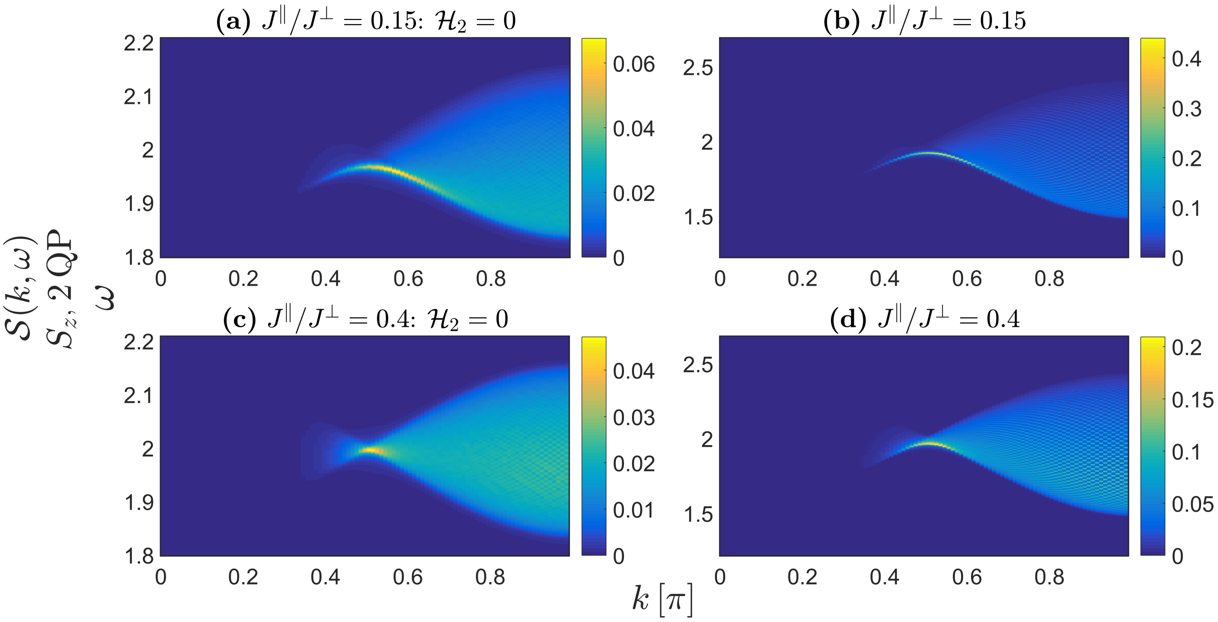

Fig. A.2: The dynamic structure factor of the dimerized chain is shown in the two-triplon sector for the coupling ratios of 0.15 and 0.4. In (a) and (c) the two triplon interactions are switched off. System size was $N = 100$.

A.1. Bimodal leg disorder

We start with investigating the effect of disorder on the legs of the dimerized chain. The static structure factor in the disordered case approximately behaves like the mean coupling ratio. It is shown in Fig. A.3. The total weight of the dimerized chain in all triplon sectors has to be 1. For the non-disordered case with coupling ratio 0.4 the deviation to that value was approximately 5.5 % and for the coupling ratio 0.15 it was 2 %. For the disordered cases it was in between these two values. That the deviations are bigger compared to the two-leg ladder is expected [23]. Despite the bigger deviations one can still expect that the results show the qualitatively right behaviour. The bimodal leg disorder that was chosen takes either the leg couplings $J^{\|} = 0.15$ or $J^{\|} = 0.4$. In Fig. A.4 one sees a plot of the dynamic structure factor for the one-triplon and two-triplon channel. The probability for the smaller leg coupling was $P(J^{\|} = 0.15) = 0.6$. Normally the dimerized chain has highest intensities at $k = \pi$ in the one-triplon channel. In Fig. A.4 one sees another part of high intensity at around $k = 3\pi/4$. This comes from the interplay of two effects: the weight of the observable gets bigger towards $k = \pi$ but the localization length and related the inverse width in k-space rises and takes its biggest value at around $k = 3\pi/4$. At $k = \pi$ the width of energies is wider due to stronger localization effects at band edges. One sees two different parts of intensity maxima. This is probably due to higher order effects in the scattering of the mean dispersion Hamiltonian with a disorder potential (compare with leading order calculations in momentum space in subsection 2.4). The same feature can be seen at $k = \pi/2$ and is proposed to have its origin also in higher order scattering terms. With respect to the whole plot one can say that the temple-like

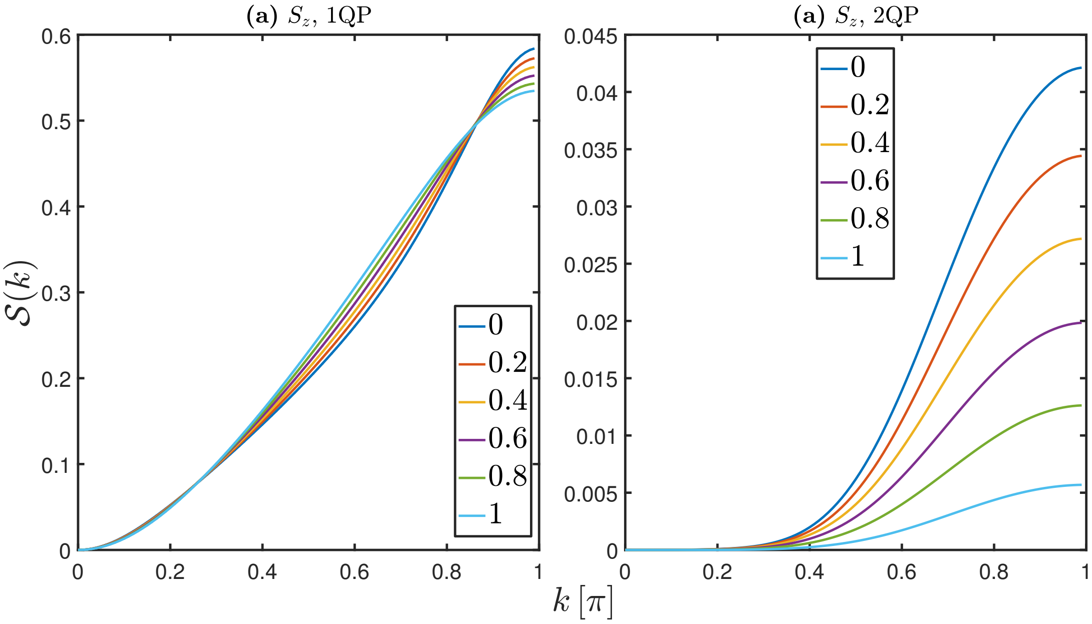

Fig. A.3: One can see the static structure factor of the dimerized chain for the leg disorder of $P(J^{\|}=0.15)=x$ and $P(J^{\|}=0.4)=1-x$ in the one- (a) and two-triplon sector (b). System size was $N=100$ and $R=100$ samples were used.

structure above the mean dispersion at $k=\pi/2$ and the parts below the mean dispersion at $k=\pi$ are a legacy of the dispersion curve of the pure $J^{\|}=0.4$-couplings.

Fig. A.5 shows the dynamic structure factor in the two-triplon channel for the leg disorder $P(J^{\|}=0.15)=0.6$ and $P(J^{\|}=0.4)=0.4$ and with two-triplon interactions switched off. The differences to the dynamic structure factor with those interactions in Fig. A.4 (b) are only small. This is in big contrast to the two-leg ladder but not surprising since the effect in the non-disordered cases was also only small. One difference is that the two-triplon interactions shift the yellow stripe in the middle of the dynamic structure factor to smaller energies and that the stripe is wider in energy such that the maximum intensities are smaller. Also more weight is contained in the part below the yellow stripe when two-triplon interactions are present. The yellow stripe can be explained by considering the dynamic structure factor in the non-disordered cases in Fig. A.2. There highest intensity is found at $k=\pi/2$ for both the cases with two-triplon interactions present and not. Disorder localizes the two-triplon states and the region of high intensity at $k=\pi/2$ gets distributed over a wider range of momenta leading to the stripe with high intensity.

Next the probability for for the lower leg coupling $P(J^{\|}=0.15)=x$ was scanned through for values of $x=0,0.2,0.4,0.6,0.8,1$ and the dynamic structure factor was calculated in the one- and two-triplon sector for different momenta. This is shown in Fig. A.6. No data of $k=\pi$ but only for $k=0.9\pi$ is shown because for a system size of $N=100$ only the momentum $k=\pi-1/200$ is reached. Although the intensity of the peak at $k=\pi/2$ is bigger for $x=1$ than for $x=0$ the peak of $x=0.2$ is higher than the one for $x=0.8$. The reason for that are stronger disorder effects due to a bigger value of $\sigma(J^{\|}_{\nu})/\left\langle J^{\|}_{\nu}\right\rangle$ that lead to a splitting of the

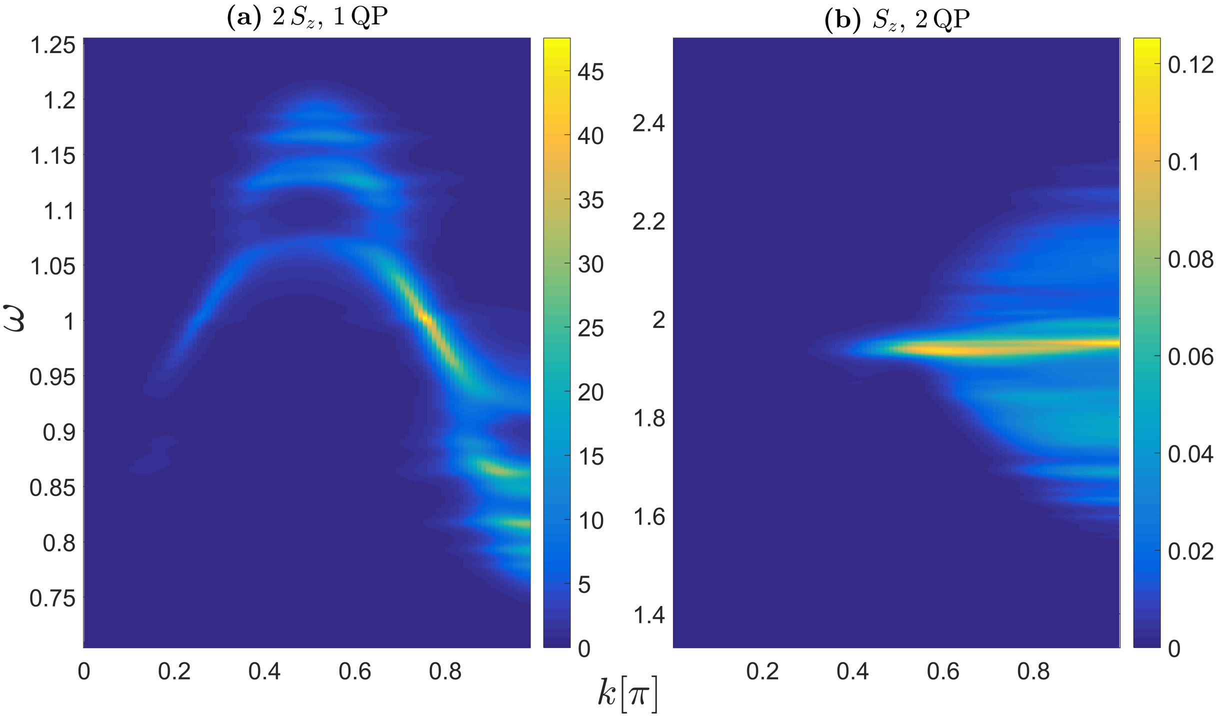

Fig. A.4: (a) The plot shows the one-triplon dynamic structure factor for a bimodal leg disorder configuration of $P(J^{\|} = 0.15) = 0.6$ and $P(J^{\|} = 0.4) = 0.4$. The structure factor was broadened by a Lorentzian of FWHM of 0.01. System size was $N = 100$ and sample size also $R = 100$.
(b) The plot shows the dynamic structure factor for the same disorder configuration and same broadening in the two-triplon channel.

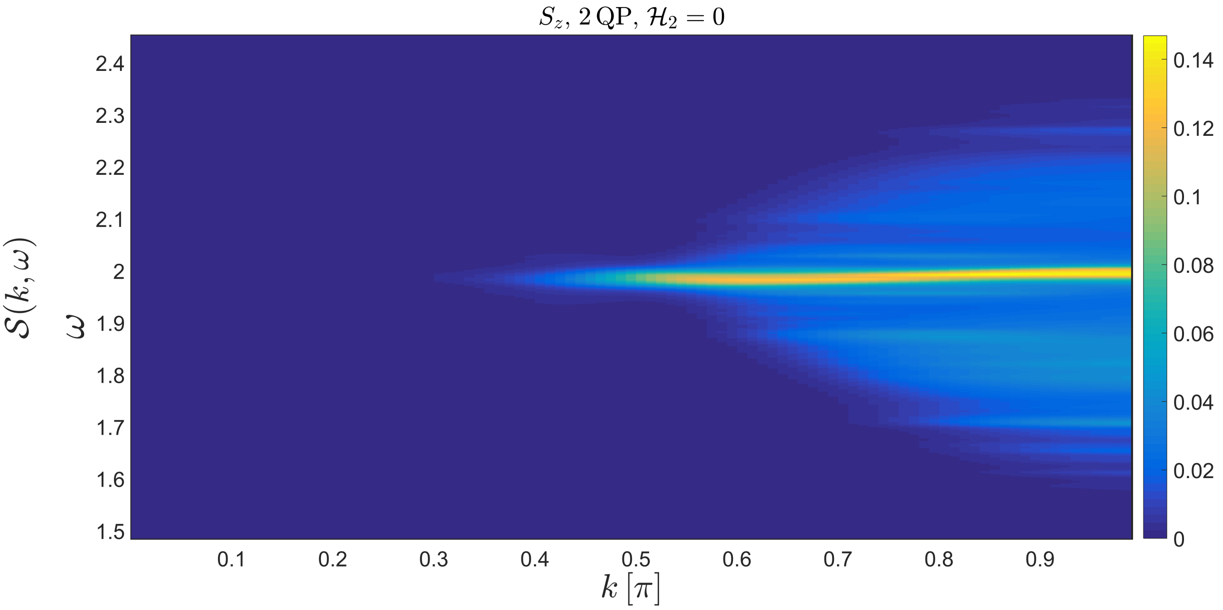

Fig. A.5: One can see the dynamic structure factor for the bimodal disorder $P(J^{\parallel} = 0.15) = 0.6$ and $P(J^{\parallel} = 0.4) = 0.4$. Two-particle interactions were switched off. Because two-triplon interactions play a less big role in the dimerized chain the difference to the plot with two-particle interactions is smaller than it is in the two-leg ladder.

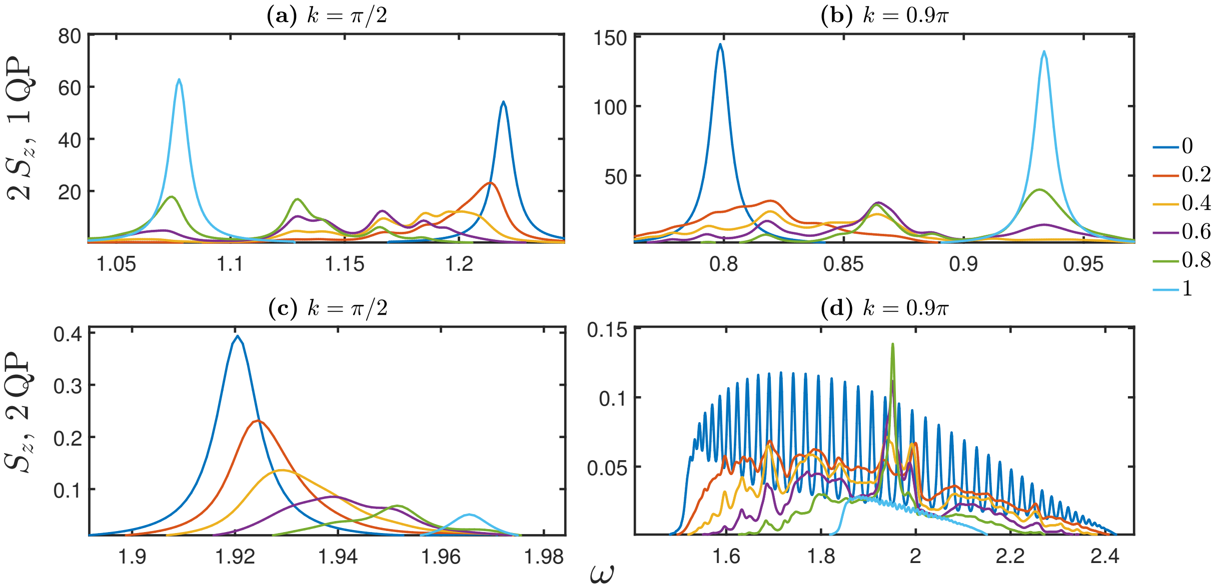

Fig. A.6: The plot shows the dynamic structure factor in the one- and two-triplon channel for a leg disorder configuration of $P(J^{\parallel} = 0.15) = x$, $P(J^{\parallel} = 0.4) = 1 - x$ and $x = 0, 0.2, 0.4, 0.6, 0.8, 1$. It was broadened with a Lorentzian of FWHM of 0.01. System size was $N = 100$ and $R = 100$ samples were used for averaging. One can see that the two-triplon weight is biggest at $k = \pi/2$ and the one-triplon weight close to $k = \pi$.

$x = 0.8$ case into two peaks. For $k = 0.9\pi$ the situation changes and the intensity of the peak for $x = 1$ is smaller. The peak in the $x = 0.2$ case has widened substantially compared to the pure $x = 0$-peak. Higher-order effects due to the bigger value of $\left\langle J_\nu^\perp \right\rangle$ are made responsible for that.

In the two-triplon case there is zero weight at momentum $k = 0$ which is a property of the dimerized chain dynamic structure factor. Disorder broadens the dynamic structure factor at $k = \pi/2$. Important for that is again the scaled disorder strength $\sigma(J_\nu^{||})/\left\langle J_\nu^{||} \right\rangle$. This leads to the interesting effect that there is a even higher peak of the $x = 0.8$ case at $k = 0.9\pi$ than the continuum of the $x = 0$ case although the mean value of the leg couplings is only 0.2 and so twice as small as 0.4. For $x = 0$ one sees oscillations at $k = 0.9\pi$ that are caused by finite-size effects. The disordered configurations show no finite-size scaling anymore.

A.2. Bimodal rung disorder

Next the effect of bimodal rung disorder shall be discussed. For that three disorder configurations were looked at. The first was one with constant small leg coupling $J^{||} = 0.15$ and a rung disorder of $P(J^\perp = 1.125) = 0.4$ and $P(J^\perp = 0.875) = 0.6$. The same rung disorder with a higher leg coupling of $J^{||} = 0.4$ was also looked at. The deviation of the total weight to 1 is 6% for the 0.4 leg-coupling and 1.7 % for the 0.15 leg-coupling. The last configuration had both rung and leg disorder. The rung disorder stayed the same but the leg couplings could now take both the values 0.4 and 0.15 with probabilities $P(J^{||} = 0.4) = 0.4$ and $P(J^{||} = 0.15) = 0.6$. Here the deviation of the total weight to 1 was 3.3 %.

In Fig. A.7 one sees plots of the dynamic structure factor in the one- and two-triplon channel for these three configurations. In plot (a) a splitting into two bands can be seen. This can be explained with Gerschgorin's circle theorem as described in subsection 2.4.3 when one considers only first order terms. The upper band contains 40% of the states in first order since $P(J^\perp = 1.125) = 0.4$. In the lower band the effective ratio of leg and rung coupling is increased. This leads to weaker localization effects and more dispersion-like shape. Also stronger higher order effects are persistent leading to a stronger intensity at $k = \pi$ and also a second intensity peak can be seen around $k = 3\pi/4$ due to weaker localization there and analogous to the one in the leg disorder case. The upper band is flater because the effective ratio of leg and rung coupling is decreased and because $P(J^\perp = 1.125) = 0.4$ and so chains of consecutive $J^\perp = 1.125$-couplings are less likely to occur.

In the two-triplon case (Fig. A.7 (d)) there is a splitting into three bands. They belong to the three different rung configurations one can build from two rung values for two triplons. One mainly sees the weight of the continuum in these three bands. The effective ratio of leg and rung coupling is biggest in the lowest band. One can argue that the stripe-like structure in the middle of the lowest band has biggest intensity because of that. In all three bands one sees those stripes. Their broadening in k-space is due to localization effects.

Fig. E.1 shows the inverse participation ratio for this disorder configuration and the one with $J^{||} = 0.4$. One clearly sees that it goes down with rising leg coupling.

In Fig. A.7 (b) the one-triplon dynamic structure factor for $J^{||} = 0.4$ shows only a minor split-

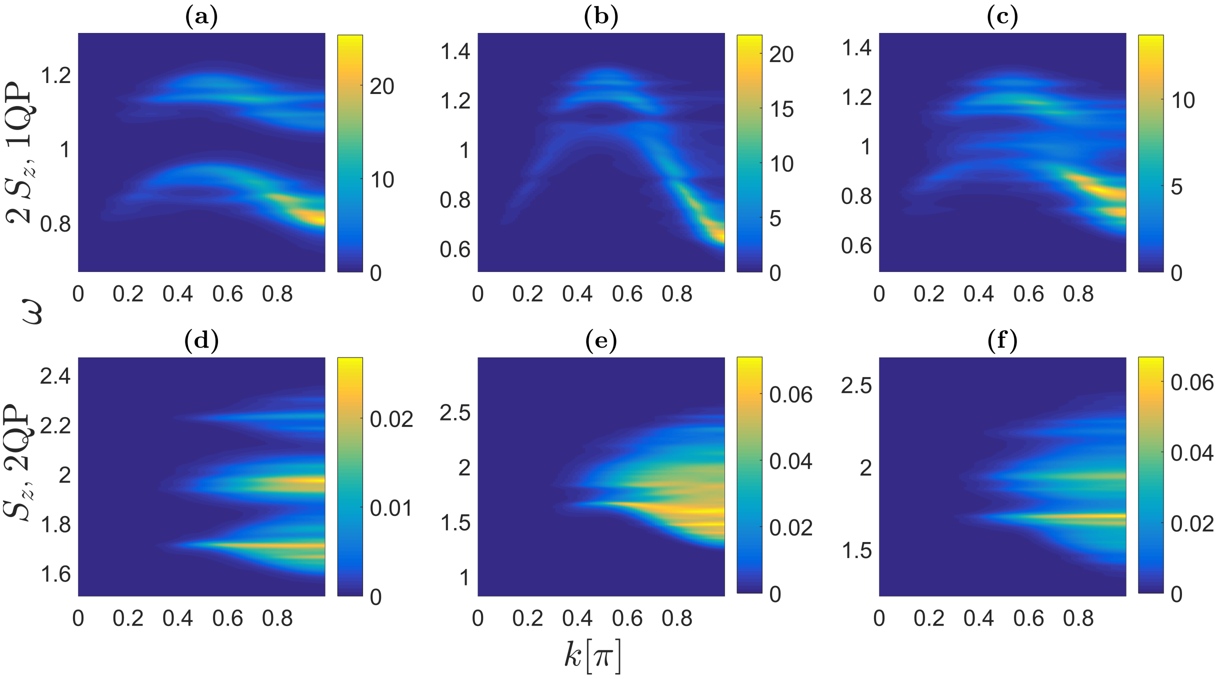

Fig. A.7: Plots show the one- and two-triplon dynamic structure factor for a bimodal rung disorder of $P(J^{\perp} = 1.125) = 0.4$, $P(J^{\perp} = 0.875) = 0.6$ and $J^{\|} = 0.15$ in (a) and (d), $P(J^{\perp} = 1.125) = 0.4$, $P(J^{\perp} = 0.875) = 0.6$ and $J^{\|} = 0.4$ in (b) and (e) and a rung and leg disorder configuration of $P(J^{\perp} = 1.125) = 0.4$, $P(J^{\perp} = 0.875) = 0.6$, $P(J^{\|} = 0.4) = 0.4$ and $P(J^{\|} = 0.15) = 0.6$ in (c) and (f). The dynamic structure factor was broadened by a Lorentzian curve of FWHM of 0.01. System size was $N = 100$ and $R = 100$ samples were used.

ting into two bands. The shape looks like a broadened dispersion curve. The lower IPR and the less flat shape are both effects of longer localization lengths. The leg coupling is bigger and stronger higher order effects lead to a bigger width and more local maxima at $k = \pi/2$. Fig. A.7 (e) shows the two-triplon dynamic structure factor of that configuration. Some stripes of high intensity are seen that overlap due to their big width in energy. Fig. A.7 (c) shows the one-triplon dynamic structure factor for the rung- and leg disorder configuration. It appears like a superposition of the dynamic structure factor in Fig. A.7 (a) and (b) and shows features of both.

Fig. E.2 shows the generalized inverse participation ratio IPR_2 and the dynamic structure factor at $k = 0.9\pi$ for all three configurations. One can see that the combination of rung and leg disorder shows a structure with more peaks than the $J^{\|} = 0.4$ case and has an overall bigger IPR_2 than the $J^{\|} = 0.15$ case. No finite-size scaling is found for the IPR_2 anymore. Thus the two-triplon eigenstates are localized in the two-triplon position basis. The dynamic structure factor of the rung- and leg disorder configuration for two triplons is shown in Fig. A.7 (f). Due to the stronger localization than in the $J^{\|} = 0.4$ case and the higher mean leg-coupling than in the $J^{\|} = 0.15$ case stripe-like structures with high intensity now appear again in the lowest band. With that the part discussing the disorder effects on the dimerized chain shall be concluded.

B. Momentum representation for correlated disorder

For correlated but stationary disorder, i.e. $\left\langle J^{\parallel}_{\nu} J^{\parallel}_{\nu+\delta}\right\rangle \neq 0$, $\left\langle J^{\perp}_{\nu} J^{\perp}_{\nu+\delta}\right\rangle \neq 0$ and $\left\langle J^{\parallel}_{\nu} J^{\perp}_{\nu+\delta}\right\rangle \neq 0$ but independent of ν, the mean absolute square of the Hamiltonian in the momentum basis can also be given using the cross-correlation theorem. Starting point is again the one-particle effective Hamiltonian transformed into the momentum basis.

$$\begin{aligned}\mathcal{H}_{1,k',k} =&\frac{1}{N}\left\langle \sum_{\nu'} e^{-i\nu' k'} \left|\nu'\right\rangle \right| \mathcal{H}_1 \left| \sum_{\nu} e^{-i\nu k} \left|\nu\right\rangle \right\rangle \\ =&\frac{1}{N}\delta_{k,k'} \sum_{\nu} \left(a_{\nu,0} + 2\sum_{t=1}^{ord} a_{\nu,t} \cos(tk) \right) \\ &+ \frac{1}{N}(1-\delta_{k,k'}) \sum_{\nu} e^{i\nu(-k+k')} \left(a_{\nu,0} + \sum_{t=1}^{ord} a_{\nu,t} (e^{itk'} + e^{-itk}) \right).\end{aligned} \tag{B.1}$$

All that has to be known to use the cross-correlation theorem is the covariance structure of the hopping element random processes. One obtains

$$\begin{aligned}&N\left\langle \left|\mathcal{H}_{1,k,k'}\right|^2 \right\rangle = 2\sum_{d} \sum_{\substack{t,t'=1 \\ t>t'}}^{ord} \mathrm{Cov}\left(a_{\nu,t} a_{\nu+d,t'}\right) \Big(\cos\left((t'-t)k + d(k-k')\right) \\ &+ \cos\left((t-t')k' + d(k-k')\right) + \cos\left(t'k + tk' + d(k-k')\right) + \cos\left(-t'k' - tk + d(k-k')\right) \Big) \\ &+ 2\sum_{d} \sum_{t=1}^{ord} \mathrm{Cov}\left(a_{\nu,0} a_{\nu+d,t}\right) \left(\cos\left(tk + d(k-k')\right) + \cos\left(-tk' + d(k-k')\right) \right) \\ &+ \sum_{d\geq 0} \sum_{t=0}^{ord} \left(2(1-\delta_{d,0}) \cos\left(d(k-k')\right) + \delta_{d,0}\right) \\ &\cdot \left(\delta_{t,0} \mathrm{Cov}\left(a_{\nu,0} a_{\nu+d,0}\right) + (1-\delta_{t,0}) \mathrm{Cov}\left(a_{\nu,t} a_{\nu+d,t}\right) 2(1+\cos\left(t(k+k')\right)\right)\right).\end{aligned} \tag{B.2}$$

C. Optimized perturbation theory

Optimized perturbation theory (OPT) was frequently used for the two-leg ladder to extrapolate one- and two-particle series results up to perturbations of $J^{\|}/J^{\perp} = 1$ [22, 23]. It is a quite robust extrapolation scheme in the sense that no spurious poles as for e.g. in Pade-extrapolations occur. Another advantage - especially for disordered problems - is its linearity [23]. The main idea behind the extrapolation is an optimized splitting in perturbed and unperturbed Hamiltonian. The original problem can be state as $H(x) = U + xV$. Introducing a new parameter a the splitting can be modified:

$$H(x; a) = (1 + a)U + xV - aU \tag{C.1}$$

This of course must not lead to a change of the Hamiltonians properties. Truncated series however will show a dependence on a which is unphysical. The original spirit of OPT was to demand that the dependence on the unphysical parameter a shall be minimal (principle of minimum sensitivity) [39]. The truncated series of effective Hamiltonian elements $\Omega_{\text{trunc}}(x; a; \mathcal{H}_{\text{eff}})$ and observables $\Omega_{\text{trunc}}(x; a; \mathcal{O}_{\text{eff}})$ depend on a and the original series as follows [22, 23]:

$$\begin{aligned}
\Omega_{\text{trunc}}(x; a; \mathcal{H}_{\text{eff}}) &= \left[\mathcal{T}\big|_{\lambda=0}^{ord} \ (1 + a(1-\lambda))\, \Omega_{\text{trunc}} \left(\frac{\lambda x}{1 + a(1-\lambda)}; \mathcal{H}_{\text{eff}} \right) \right]_{\lambda=1} \\
\Omega_{\text{trunc}}(x; a; \mathcal{O}_{\text{eff}}) &= \left[\mathcal{T}\big|_{\lambda=0}^{ord} \ \Omega_{\text{trunc}} \left(\frac{\lambda x}{1 + a(1-\lambda)}; \mathcal{O}_{\text{eff}} \right) \right]_{\lambda=1}
\end{aligned} \tag{C.2}$$

$\mathcal{T}\big|_{x=x_0}^{n}$ denotes a Taylor expansion of the variable x up to order n. In contrast to the principle of minimum sensitivity in [22, 23] model dependent quantities like the spin gap were compared with reliable DlogPadé extrapolants. Values for a were determined this way and used to calculate all other Hamiltonian elements. One thing that should be emphasised is that a will depend strongly on the order of the perturbative series. For multiple perturbation parameters a generalization of (C.2) is straightforward:

$$\begin{aligned}
\Omega_{\text{trunc}}(x_1, ..; a; \mathcal{H}_{\text{eff}}) &= \left[\mathcal{T}\big|_{\lambda=0}^{ord} \ (1 + a(1-\lambda))\, \Omega_{\text{trunc}} \left(\frac{\lambda x_1}{1 + a(1-\lambda)}, ...; \mathcal{H}_{\text{eff}} \right) \right]_{\lambda=1} \\
\Omega_{\text{trunc}}(x_1, ...; a; \mathcal{O}_{\text{eff}}) &= \left[\mathcal{T}\big|_{\lambda=0}^{ord} \ \Omega_{\text{trunc}} \left(\frac{\lambda x_1}{1 + a(1-\lambda)}, ...; \mathcal{O}_{\text{eff}} \right) \right]_{\lambda=1}
\end{aligned} \tag{C.3}$$

Every perturbation parameter gets scaled with $\frac{\lambda}{1+a(1-\lambda)}$ on the right hand site of equations (C.3). This way the a-dependent quantities can be obtained for every supersite on a lattice with arbitrary couplings and so also in the case of disorder. In principle a could be chosen differently for every supersite ν and every quantity looked at. However, no clearly defined criteria was found for choosing it this way. Instead the linearity of the OPT was used. The mean of an a-modified OPT quantity $G(a;\nu)$ equals the OPT of the mean of the quantity $G(\nu)$:

$$\langle G(a;\nu)\rangle = \mathrm{OPT}(\langle G(\nu)\rangle) \tag{C.4}$$

E.g. the mean gap, that is the mean value of $\mathcal{H}_1(\pi,\pi)$ - $\langle\mathcal{H}_1(\pi,\pi)\rangle$, can be obtained as a series and then be extrapolated with DlogPadé methods. The a-value of the OPT is afterwards chosen by comparing the OPT of the mean gap with that value and demanding it to equal. Finally, for the so obtained a the OPT Hamiltonian will have the same mean gap.

D. Mean expressions

Non-energy resolved ground state averages at $T = 0$ can be calculated by averaging the truncated series of the quantity over all disorder configurations. For the simple case that rung and leg couplings are pairwise stochastically independent the mean of such a series can be written as a series over the moments of $J_\nu^\perp$ and $J_\nu^\parallel$. Hereby the linearity of the mean and the decoupling of the mean of stochastically independent random variables is used. That is for two independent random variables x and y

$$\langle x^n y^m \rangle = \langle x^n \rangle \langle y^m \rangle \tag{D.1}$$

holds. Such series expansions of averaged quantities in the high-field limit are promising for understanding critical and Griffiths-McCoy singularities as was only recently shown by Singh and Young [40]. In the following such series are given for the ground state-energies, the mean of the one-particle effective Hamiltonian in momentum basis at (π, π) and the variance thereof for both dimerized chain and two-leg ladder. Also given is the total weight of the antisymmetric and symmetric spin observable of the two-leg ladder and the static structure factor of dimerized chain and two-leg ladder for one- and two-triplons. From the static structure factor spin-spin correlations between different supersites of the ladder $\langle \boldsymbol{S}_{\nu,..} \boldsymbol{S}_{\nu+\delta,..} \rangle$ can be written of as half the prefactors of $\cos(\delta k)$ and for the dimerized chain spin-spin correlations of the sites $\langle \boldsymbol{S}_{s,..} \boldsymbol{S}_{s+\delta,..} \rangle$ can also be extracted as half the prefactors of $\cos(\delta k)$. The term that does not contain cosine factors is the total weight of the observable in the corresponding particle channel. The series are truncated at a lower than the actually obtained order here because they would be too lengthy otherwise. The moments of leg and rung couplings are respectively denoted by

$$\left\langle J_\nu^{\parallel\, n} \right\rangle = p_n \tag{D.2}$$

and

$$\left\langle (J_\nu^\perp - 1)^n \right\rangle = v_n. \tag{D.3}$$

Higher order mean expressions can be requested from the author via mail: max.hoermann@fau.de

Average ground state energy per dimer of two-leg ladder in perturbation order 5 (available in order 8):

$$\begin{aligned}
&-\frac{3\,\mathrm{p_1}^2}{16}-\frac{3\,\mathrm{p_2}}{16}+\frac{3\,\mathrm{v_1}\,\mathrm{p_1}^2}{16}-\frac{9\,\mathrm{p_2}\,\mathrm{p_1}}{64}-\frac{3\,\mathrm{p_3}}{64}+\frac{3\,\mathrm{p_2}\,\mathrm{v_1}}{16}+\frac{7\,\mathrm{p_1}^4}{256}+\frac{3\,\mathrm{p_1}^2\,\mathrm{p_2}}{128}\\
&-\frac{3\,\mathrm{p_1}^2\,\mathrm{v_1}^2}{32}-\frac{3\,\mathrm{v_2}\,\mathrm{p_1}^2}{32}+\frac{9\,\mathrm{p_1}\,\mathrm{p_2}\,\mathrm{v_1}}{32}-\frac{3\,\mathrm{p_3}\,\mathrm{p_1}}{256}-\frac{13\,\mathrm{p_2}^2}{1024}-\frac{3\,\mathrm{p_2}\,\mathrm{v_1}^2}{32}\\
&-\frac{3\,\mathrm{v_2}\,\mathrm{p_2}}{32}+\frac{3\,\mathrm{p_3}\,\mathrm{v_1}}{32}-\frac{3\,\mathrm{p_4}}{1024}+\frac{15\,\mathrm{p_5}}{4096}+\frac{75\,\mathrm{p_1}\,\mathrm{p_4}}{4096}+\frac{203\,\mathrm{p_2}\,\mathrm{p_3}}{6144}\\
&+\frac{3\,\mathrm{p_2}\,\mathrm{v_3}}{64}-\frac{9\,\mathrm{p_3}\,\mathrm{v_2}}{128}+\frac{9\,\mathrm{p_4}\,\mathrm{v_1}}{1024}+\frac{79\,\mathrm{p_1}\,\mathrm{p_2}^2}{3072}+\frac{15\,\mathrm{p_1}^2\,\mathrm{p_3}}{1024}+\frac{247\,\mathrm{p_1}^3\,\mathrm{p_2}}{3072}\\
&+\frac{39\,\mathrm{p_2}^2\,\mathrm{v_1}}{1024}-\frac{9\,\mathrm{p_3}\,\mathrm{v_1}^2}{128}+\frac{3\,\mathrm{p_1}^2\,\mathrm{v_3}}{64}-\frac{21\,\mathrm{p_1}^4\,\mathrm{v_1}}{256}-\frac{27\,\mathrm{p_1}\,\mathrm{p_2}\,\mathrm{v_1}^2}{128}\\
&-\frac{9\,\mathrm{p_1}^2\,\mathrm{p_2}\,\mathrm{v_1}}{128}+\frac{9\,\mathrm{p_1}^2\,\mathrm{v_1}\,\mathrm{v_2}}{64}-\frac{27\,\mathrm{p_1}\,\mathrm{p_2}\,\mathrm{v_2}}{128}+\frac{9\,\mathrm{p_1}\,\mathrm{p_3}\,\mathrm{v_1}}{256}+\frac{9\,\mathrm{p_2}\,\mathrm{v_1}\,\mathrm{v_2}}{64}
\end{aligned}\tag{D.4}$$

Average ground state energy per dimer of dimerized chain in perturbation order 5 (available order 8):

$$\begin{aligned}
&-\frac{3\,\mathrm{p_2}}{32}+\frac{3\,\mathrm{p_2}\,\mathrm{v_1}}{32}-\frac{3\,\mathrm{p_3}}{128}-\frac{5\,\mathrm{p_2}^2}{1024}-\frac{3\,\mathrm{p_2}\,\mathrm{v_1}^2}{64}-\frac{3\,\mathrm{v_2}\,\mathrm{p_2}}{64}+\frac{3\,\mathrm{p_3}\,\mathrm{v_1}}{64}-\frac{3\,\mathrm{p_4}}{2048}+\frac{15\,\mathrm{p_5}}{8192}\\
&-\frac{67\,\mathrm{p_2}\,\mathrm{p_3}}{12288}+\frac{3\,\mathrm{p_2}\,\mathrm{v_3}}{128}-\frac{9\,\mathrm{p_3}\,\mathrm{v_2}}{256}+\frac{9\,\mathrm{p_4}\,\mathrm{v_1}}{2048}+\frac{15\,\mathrm{p_2}^2\,\mathrm{v_1}}{1024}-\frac{9\,\mathrm{p_3}\,\mathrm{v_1}^2}{256}+\frac{9\,\mathrm{p_2}\,\mathrm{v_1}\,\mathrm{v_2}}{128}
\end{aligned}\tag{D.5}$$

Mean gap of two-leg ladder in perturbation order 5 (available order 8):

$$\begin{aligned}
&1-\frac{\mathrm{p_1}}{2}+\frac{9\,\mathrm{p_1}^2}{8}-\frac{5\,\mathrm{p_2}}{8}-\frac{5\,\mathrm{p_1}^3}{8}-\frac{9\,\mathrm{v_1}\,\mathrm{p_1}^2}{8}+\frac{47\,\mathrm{p_2}\,\mathrm{p_1}}{64}+\frac{3\,\mathrm{p_3}}{32}+\frac{5\,\mathrm{p_2}\,\mathrm{v_1}}{8}\\
&+\frac{109\,\mathrm{p_1}^4}{384}+\frac{5\,\mathrm{p_1}^3\,\mathrm{v_1}}{4}-\frac{13\,\mathrm{p_1}^2\,\mathrm{p_2}}{24}+\frac{9\,\mathrm{p_1}^2\,\mathrm{v_1}^2}{32}+\frac{27\,\mathrm{v_2}\,\mathrm{p_1}^2}{32}-\frac{25\,\mathrm{p_1}\,\mathrm{p_2}\,\mathrm{v_1}}{16}\\
&-\frac{99\,\mathrm{p_3}\,\mathrm{p_1}}{128}+\frac{333\,\mathrm{p_2}^2}{512}-\frac{\mathrm{p_2}\,\mathrm{v_1}^2}{16}-\frac{9\,\mathrm{v_2}\,\mathrm{p_2}}{16}-\frac{3\,\mathrm{p_3}\,\mathrm{v_1}}{16}+\frac{131\,\mathrm{p_4}}{512}+\frac{17\,\mathrm{p_2}\,\mathrm{v_3}}{32}\\
&-\frac{7211\,\mathrm{p_1}\,\mathrm{p_4}}{24576}-\frac{2291\,\mathrm{p_2}\,\mathrm{p_3}}{6144}-\frac{15\,\mathrm{p_5}}{2048}+\frac{5\,\mathrm{p_3}\,\mathrm{v_2}}{64}-\frac{393\,\mathrm{p_4}\,\mathrm{v_1}}{512}-\frac{763\,\mathrm{p_1}\,\mathrm{p_2}^2}{73728}\\
&+\frac{23849\,\mathrm{p_1}^2\,\mathrm{p_3}}{18432}-\frac{6265\,\mathrm{p_1}^3\,\mathrm{p_2}}{18432}-\frac{999\,\mathrm{p_2}^2\,\mathrm{v_1}}{512}+\frac{13\,\mathrm{p_3}\,\mathrm{v_1}^2}{64}-\frac{87\,\mathrm{p_1}^2\,\mathrm{v_3}}{128}\\
&-\frac{857\,\mathrm{p_1}^3\,\mathrm{v_2}}{512}-\frac{109\,\mathrm{p_1}^4\,\mathrm{v_1}}{128}-\frac{65\,\mathrm{p_1}^5}{128}+\frac{3\,\mathrm{p_1}^2\,\mathrm{v_1}^3}{64}-\frac{103\,\mathrm{p_1}^3\,\mathrm{v_1}^2}{512}+\frac{147\,\mathrm{p_1}\,\mathrm{p_2}\,\mathrm{v_1}^2}{512}\\
&+\frac{13\,\mathrm{p_1}^2\,\mathrm{p_2}\,\mathrm{v_1}}{8}-\frac{63\,\mathrm{p_1}^2\,\mathrm{v_1}\,\mathrm{v_2}}{128}+\frac{1053\,\mathrm{p_1}\,\mathrm{p_2}\,\mathrm{v_2}}{512}+\frac{297\,\mathrm{p_1}\,\mathrm{p_3}\,\mathrm{v_1}}{128}+\frac{3\,\mathrm{p_2}\,\mathrm{v_1}\,\mathrm{v_2}}{32}
\end{aligned}\tag{D.6}$$

Variance of two-leg ladder mean gap in perturbation order 5 (available order 8):

$$\begin{aligned}
&2\,v_1 - p_1 + \frac{p_1^2}{2} - 2\,v_1\,p_1 + \frac{p_2}{4} + v_2 + \frac{p_1^3}{8} + \frac{9\,v_1\,p_1^2}{4} - \frac{27\,p_2\,p_1}{32} + \frac{5\,p_3}{16}\\
&- \frac{5\,p_2\,v_1}{4} - \frac{15\,p_1^4}{32} - \frac{11\,p_1^3\,v_1}{8} + \frac{23\,p_1^2\,p_2}{32} - \frac{3\,p_1^2\,v_1^2}{2} - \frac{3\,v_2\,p_1^2}{4}\\
&+ \frac{5\,p_1\,p_2\,v_1}{2} - \frac{35\,p_3\,p_1}{32} + \frac{127\,p_2^2}{256} + \frac{9\,p_2\,v_1^2}{8} + \frac{v_2\,p_2}{8} - \frac{p_3\,v_1}{8} + \frac{13\,p_4}{256}\\
&+ \frac{993\,p_1\,p_4}{4096} - \frac{161\,p_5}{1024} - \frac{13\,p_2\,p_3}{128} - \frac{p_2\,v_3}{16} - \frac{p_3\,v_2}{32} + \frac{105\,p_4\,v_1}{256} + \frac{10045\,p_1\,p_2^2}{12288}\\
&+ \frac{277\,p_1^2\,p_3}{512} - \frac{1131\,p_1^3\,p_2}{512} + \frac{79\,p_2^2\,v_1}{256} - \frac{p_3\,v_1^2}{32} + \frac{13\,p_1^2\,v_3}{32} + \frac{35\,p_1^3\,v_2}{128}\\
&+ \frac{289\,p_1^4\,v_1}{192} + \frac{743\,p_1^5}{768} - \frac{p_1^2\,v_1^3}{8} + \frac{301\,p_1^3\,v_1^2}{128} - \frac{369\,p_1\,p_2\,v_1^2}{128}\\
&- \frac{251\,p_1^2\,p_2\,v_1}{96} + \frac{63\,p_1^2\,v_1\,v_2}{32} - \frac{151\,p_1\,p_2\,v_2}{128} + \frac{41\,p_1\,p_3\,v_1}{64} - \frac{19\,p_2\,v_1\,v_2}{16}
\end{aligned} \tag{D.7}$$

Mean gap of dimerized chain in perturbation order 5 (available order 8):

$$\begin{aligned}
&1 - \frac{p_1^2}{16} - \frac{5\,p_2}{16} - \frac{p_1^3}{64} + \frac{v_1\,p_1^2}{16} + \frac{3\,p_3}{64} + \frac{23\,p_2\,v_1}{64} - \frac{5\,p_1^4}{1024} + \frac{p_1^3\,v_1}{32} - \frac{p_1^2\,p_2}{48}\\
&- \frac{5\,p_1^2\,v_1^2}{128} - \frac{3\,v_2\,p_1^2}{128} + \frac{3\,p_3\,p_1}{256} - \frac{65\,p_2^2}{512} - \frac{p_2\,v_1^2}{32} - \frac{9\,v_2\,p_2}{32} - \frac{3\,p_3\,v_1}{32}\\
&+ \frac{131\,p_4}{1024} + \frac{17\,p_2\,v_3}{64} - \frac{307\,p_1\,p_4}{12288} - \frac{881\,p_2\,p_3}{24576} - \frac{15\,p_5}{4096} + \frac{5\,p_3\,v_2}{128} - \frac{393\,p_4\,v_1}{1024}\\
&+ \frac{317\,p_1\,p_2^2}{24576} - \frac{25\,p_1^2\,p_3}{36864} - \frac{545\,p_1^3\,p_2}{73728} + \frac{195\,p_2^2\,v_1}{512} + \frac{13\,p_3\,v_1^2}{128} + \frac{5\,p_1^2\,v_3}{512}\\
&- \frac{31\,p_1^3\,v_2}{2048} + \frac{15\,p_1^4\,v_1}{1024} - \frac{7\,p_1^5}{4096} + \frac{3\,p_1^2\,v_1^3}{256} - \frac{65\,p_1^3\,v_1^2}{2048} - \frac{197\,p_1\,p_2\,v_1^2}{2048}\\
&+ \frac{p_1^2\,p_2\,v_1}{16} + \frac{21\,p_1^2\,v_1\,v_2}{512} + \frac{197\,p_1\,p_2\,v_2}{2048} - \frac{9\,p_1\,p_3\,v_1}{256} + \frac{3\,p_2\,v_1\,v_2}{64}
\end{aligned} \tag{D.8}$$

Variance of dimerized chain mean gap in perturbation order 5 (available order 8):

$$\begin{aligned}
&2\,\mathrm{v}_1 - \mathrm{p}_1 + \frac{\mathrm{p}_1{}^2}{8} - 1\,\mathrm{v}_1\,\mathrm{p}_1 + \frac{\mathrm{p}_2}{8} + \mathrm{v}_2 + \frac{\mathrm{p}_1{}^3}{32} - \frac{\mathrm{v}_1\,\mathrm{p}_1{}^2}{8} + \frac{3\,\mathrm{p}_2\,\mathrm{p}_1}{16}\\
&+ \frac{5\,\mathrm{p}_3}{32} - \frac{23\,\mathrm{p}_2\,\mathrm{v}_1}{32} + \frac{3\,\mathrm{p}_1{}^4}{512} - \frac{\mathrm{p}_1{}^3\,\mathrm{v}_1}{16} - \frac{\mathrm{p}_1{}^2\,\mathrm{p}_2}{256} + \frac{3\,\mathrm{p}_1{}^2\,\mathrm{v}_1{}^2}{32} + \frac{\mathrm{v}_2\,\mathrm{p}_1{}^2}{32}\\
&- \frac{3\,\mathrm{p}_1\,\mathrm{p}_2\,\mathrm{v}_1}{16} - \frac{\mathrm{p}_3\,\mathrm{p}_1}{256} - \frac{7\,\mathrm{p}_2{}^2}{128} + \frac{9\,\mathrm{p}_2\,\mathrm{v}_1{}^2}{16} + \frac{\mathrm{v}_2\,\mathrm{p}_2}{16} - \frac{\mathrm{p}_3\,\mathrm{v}_1}{16} + \frac{13\,\mathrm{p}_4}{512}\\
&+ \frac{185\,\mathrm{p}_2\,\mathrm{p}_3}{2048} - \frac{143\,\mathrm{p}_1\,\mathrm{p}_4}{2048} - \frac{161\,\mathrm{p}_5}{2048} - \frac{\mathrm{p}_2\,\mathrm{v}_3}{32} - \frac{\mathrm{p}_3\,\mathrm{v}_2}{64} + \frac{105\,\mathrm{p}_4\,\mathrm{v}_1}{512}\\
&+ \frac{1873\,\mathrm{p}_1\,\mathrm{p}_2{}^2}{36864} + \frac{9\,\mathrm{p}_1{}^2\,\mathrm{p}_3}{1024} + \frac{55\,\mathrm{p}_1{}^3\,\mathrm{p}_2}{6144} - \frac{59\,\mathrm{p}_2{}^2\,\mathrm{v}_1}{512} - \frac{\mathrm{p}_3\,\mathrm{v}_1{}^2}{64} - \frac{\mathrm{p}_1{}^2\,\mathrm{v}_3}{128}\\
&+ \frac{13\,\mathrm{p}_1{}^3\,\mathrm{v}_2}{512} - \frac{11\,\mathrm{p}_1{}^4\,\mathrm{v}_1}{512} + \frac{3\,\mathrm{p}_1{}^5}{2048} - \frac{\mathrm{p}_1{}^2\,\mathrm{v}_1{}^3}{32} + \frac{35\,\mathrm{p}_1{}^3\,\mathrm{v}_1{}^2}{512} + \frac{3\,\mathrm{p}_1\,\mathrm{p}_2\,\mathrm{v}_1{}^2}{512}\\
&- \frac{43\,\mathrm{p}_1{}^2\,\mathrm{p}_2\,\mathrm{v}_1}{1536} - \frac{11\,\mathrm{p}_1{}^2\,\mathrm{v}_1\,\mathrm{v}_2}{128} + \frac{93\,\mathrm{p}_1\,\mathrm{p}_2\,\mathrm{v}_2}{512} + \frac{\mathrm{p}_1\,\mathrm{p}_3\,\mathrm{v}_1}{32} - \frac{19\,\mathrm{p}_2\,\mathrm{v}_1\,\mathrm{v}_2}{32}
\end{aligned} \tag{D.9}$$

Total weight of the antisymmetric spin observable $S_{z,1} - S_{z,2}$ for the two-leg ladder up to perturbation order 5 (available order 7):

$$\begin{aligned}
&-\frac{\mathrm{p}_1{}^2}{8} - \frac{\mathrm{p}_2}{8} + \frac{\mathrm{v}_1\,\mathrm{p}_1{}^2}{4} - \frac{3\,\mathrm{p}_2\,\mathrm{p}_1}{16} - \frac{\mathrm{p}_3}{16} + \frac{\mathrm{p}_2\,\mathrm{v}_1}{4} + \frac{7\,\mathrm{p}_1{}^4}{128} + \frac{3\,\mathrm{p}_1{}^2\,\mathrm{p}_2}{64} - \frac{3\,\mathrm{p}_1{}^2\,\mathrm{v}_1{}^2}{16}\\
&- \frac{3\,\mathrm{v}_2\,\mathrm{p}_1{}^2}{16} + \frac{9\,\mathrm{p}_1\,\mathrm{p}_2\,\mathrm{v}_1}{16} - \frac{3\,\mathrm{p}_3\,\mathrm{p}_1}{128} - \frac{13\,\mathrm{p}_2{}^2}{512} - \frac{3\,\mathrm{p}_2\,\mathrm{v}_1{}^2}{16} - \frac{3\,\mathrm{v}_2\,\mathrm{p}_2}{16} + \frac{3\,\mathrm{p}_3\,\mathrm{v}_1}{16}\\
&- \frac{3\,\mathrm{p}_4}{512} + \frac{5\,\mathrm{p}_5}{512} + \frac{25\,\mathrm{p}_1\,\mathrm{p}_4}{512} + \frac{203\,\mathrm{p}_2\,\mathrm{p}_3}{2304} + \frac{\mathrm{p}_2\,\mathrm{v}_3}{8} - \frac{3\,\mathrm{p}_3\,\mathrm{v}_2}{16} + \frac{3\,\mathrm{p}_4\,\mathrm{v}_1}{128} + \frac{79\,\mathrm{p}_1\,\mathrm{p}_2{}^2}{1152}\\
&+ \frac{5\,\mathrm{p}_1{}^2\,\mathrm{p}_3}{128} + \frac{247\,\mathrm{p}_1{}^3\,\mathrm{p}_2}{1152} + \frac{13\,\mathrm{p}_2{}^2\,\mathrm{v}_1}{128} - \frac{3\,\mathrm{p}_3\,\mathrm{v}_1{}^2}{16} + \frac{\mathrm{p}_1{}^2\,\mathrm{v}_3}{8} - \frac{7\,\mathrm{p}_1{}^4\,\mathrm{v}_1}{32}\\
&- \frac{9\,\mathrm{p}_1\,\mathrm{p}_2\,\mathrm{v}_1{}^2}{16} - \frac{3\,\mathrm{p}_1{}^2\,\mathrm{p}_2\,\mathrm{v}_1}{16} + \frac{3\,\mathrm{p}_1{}^2\,\mathrm{v}_1\,\mathrm{v}_2}{8} - \frac{9\,\mathrm{p}_1\,\mathrm{p}_2\,\mathrm{v}_2}{16} + \frac{3\,\mathrm{p}_1\,\mathrm{p}_3\,\mathrm{v}_1}{32} + \frac{3\,\mathrm{p}_2\,\mathrm{v}_1\,\mathrm{v}_2}{8}
\end{aligned} \tag{D.10}$$

Total weight of the symmetric spin observable $S_{z,1} + S_{z,2}$ for the two-leg ladder up to perturbation order 5 (available order 7):

$$\begin{aligned}
&\frac{\mathrm{p}_1{}^2}{8} + \frac{\mathrm{p}_2}{8} - \frac{\mathrm{v}_1\,\mathrm{p}_1{}^2}{4} + \frac{3\,\mathrm{p}_2\,\mathrm{p}_1}{16} + \frac{\mathrm{p}_3}{16} - \frac{\mathrm{p}_2\,\mathrm{v}_1}{4} - \frac{7\,\mathrm{p}_1{}^4}{128} - \frac{3\,\mathrm{p}_1{}^2\,\mathrm{p}_2}{64} + \frac{3\,\mathrm{p}_1{}^2\,\mathrm{v}_1{}^2}{16}\\
&+ \frac{3\,\mathrm{v}_2\,\mathrm{p}_1{}^2}{16} - \frac{9\,\mathrm{p}_1\,\mathrm{p}_2\,\mathrm{v}_1}{16} + \frac{3\,\mathrm{p}_3\,\mathrm{p}_1}{128} + \frac{13\,\mathrm{p}_2{}^2}{512} + \frac{3\,\mathrm{p}_2\,\mathrm{v}_1{}^2}{16} + \frac{3\,\mathrm{v}_2\,\mathrm{p}_2}{16} - \frac{3\,\mathrm{p}_3\,\mathrm{v}_1}{16}\\
&+ \frac{3\,\mathrm{p}_4}{512} + \frac{3\,\mathrm{p}_3\,\mathrm{v}_2}{16} - \frac{25\,\mathrm{p}_1\,\mathrm{p}_4}{512} - \frac{203\,\mathrm{p}_2\,\mathrm{p}_3}{2304} - \frac{\mathrm{p}_2\,\mathrm{v}_3}{8} - \frac{5\,\mathrm{p}_5}{512} - \frac{3\,\mathrm{p}_4\,\mathrm{v}_1}{128} - \frac{79\,\mathrm{p}_1\,\mathrm{p}_2{}^2}{1152}\\
&- \frac{5\,\mathrm{p}_1{}^2\,\mathrm{p}_3}{128} - \frac{247\,\mathrm{p}_1{}^3\,\mathrm{p}_2}{1152} - \frac{13\,\mathrm{p}_2{}^2\,\mathrm{v}_1}{128} + \frac{3\,\mathrm{p}_3\,\mathrm{v}_1{}^2}{16} - \frac{\mathrm{p}_1{}^2\,\mathrm{v}_3}{8} + \frac{7\,\mathrm{p}_1{}^4\,\mathrm{v}_1}{32}\\
&+ \frac{9\,\mathrm{p}_1\,\mathrm{p}_2\,\mathrm{v}_1{}^2}{16} + \frac{3\,\mathrm{p}_1{}^2\,\mathrm{p}_2\,\mathrm{v}_1}{16} - \frac{3\,\mathrm{p}_1{}^2\,\mathrm{v}_1\,\mathrm{v}_2}{8} + \frac{9\,\mathrm{p}_1\,\mathrm{p}_2\,\mathrm{v}_2}{16} - \frac{3\,\mathrm{p}_1\,\mathrm{p}_3\,\mathrm{v}_1}{32} - \frac{3\,\mathrm{p}_2\,\mathrm{v}_1\,\mathrm{v}_2}{8}
\end{aligned} \tag{D.11}$$

Static structure factor of the spin observable S_z for the dimerized chain in the one-particle sector up to perturbation order 3 (available order 7):

$$
\begin{aligned}
&\left(\frac{\mathrm{p}_2}{4}-\frac{\mathrm{p}_1}{8}+\frac{23\,\mathrm{p}_3}{256}-\frac{7\,\mathrm{p}_1\,\mathrm{p}_2}{384}+\frac{\mathrm{p}_1\,\mathrm{v}_1}{8}-\frac{\mathrm{p}_1\,\mathrm{v}_2}{16}-\frac{\mathrm{p}_2\,\mathrm{v}_1}{2}-\frac{\mathrm{p}_1\,{\mathrm{v}_1}^2}{16}-\frac{1}{2}\right)\cos(k)\\
&+\left(\frac{\mathrm{p}_1}{4}-\frac{\mathrm{p}_2}{16}-\frac{5\,\mathrm{p}_3}{128}+\frac{5\,\mathrm{p}_1\,\mathrm{p}_2}{192}-\frac{\mathrm{p}_1\,\mathrm{v}_1}{4}+\frac{\mathrm{p}_1\,\mathrm{v}_2}{8}+\frac{\mathrm{p}_2\,\mathrm{v}_1}{8}+\frac{\mathrm{p}_1\,{\mathrm{v}_1}^2}{8}\right)\cos(2\,k)\\
&+\left(\frac{\mathrm{p}_1\,\mathrm{v}_1}{8}-\frac{\mathrm{p}_2}{32}-\frac{\mathrm{p}_3}{256}-\frac{5\,\mathrm{p}_1\,\mathrm{p}_2}{128}-\frac{\mathrm{p}_1}{8}-\frac{\mathrm{p}_1\,\mathrm{v}_2}{16}+\frac{\mathrm{p}_2\,\mathrm{v}_1}{16}-\frac{\mathrm{p}_1\,{\mathrm{v}_1}^2}{16}\right.\\
&\left.+\frac{3\,{\mathrm{p}_1}^2\,\mathrm{v}_1}{32}-\frac{3\,{\mathrm{p}_1}^2}{64}\right)\cos(3\,k)+\left(\frac{7\,\mathrm{p}_1\,\mathrm{p}_2}{96}-\frac{3\,{\mathrm{p}_1}^2\,\mathrm{v}_1}{16}+\frac{3\,{\mathrm{p}_1}^2}{32}\right)\cos(4\,k)\\
&+\left(\frac{3\,{\mathrm{p}_1}^2\,\mathrm{v}_1}{32}-\frac{\mathrm{p}_1\,\mathrm{p}_2}{24}-\frac{3\,{\mathrm{p}_1}^2}{64}-\frac{5\,{\mathrm{p}_1}^3}{256}\right)\cos(5\,k)+\frac{(5\,{\mathrm{p}_1}^3)}{128}\cos(6\,k)\\
&+-\frac{5\,{\mathrm{p}_1}^3}{256}\cos(7\,k)+\left(\frac{5\,\mathrm{p}_2\,\mathrm{v}_1}{16}-\frac{3\,\mathrm{p}_3}{64}-\frac{5\,\mathrm{p}_2}{32}+\frac{1}{2}\right)
\end{aligned}
\tag{D.12}
$$

Static structure factor of the antisymmetric spin observable $S_{z,1}-S_{z,2}$ for the two-leg ladder in the one-particle sector up to perturbation order 3 (available order 7):

$$
\begin{aligned}
&\left(\frac{\mathrm{p}_2}{4}-\mathrm{p}_1+\frac{5\,\mathrm{p}_3}{32}-\frac{31\,\mathrm{p}_1\,\mathrm{p}_2}{96}+\mathrm{p}_1\,\mathrm{v}_1-\frac{\mathrm{p}_1\,\mathrm{v}_2}{2}-\frac{\mathrm{p}_2\,\mathrm{v}_1}{2}-\frac{\mathrm{p}_1\,{\mathrm{v}_1}^2}{2}+\frac{3\,{\mathrm{p}_1}^2\,\mathrm{v}_1}{2}\right.\\
&\left.-\frac{3\,{\mathrm{p}_1}^2}{4}+\frac{13\,{\mathrm{p}_1}^3}{24}\right)\cos(k)+\left(\frac{2\,\mathrm{p}_1\,\mathrm{p}_2}{3}-\frac{3\,{\mathrm{p}_1}^2\,\mathrm{v}_1}{2}+\frac{3\,{\mathrm{p}_1}^2}{4}-\frac{{\mathrm{p}_1}^3}{6}\right)\cos(2\,k)+\\
&-\frac{5\,{\mathrm{p}_1}^3}{8}\cos(3\,k)+\left(\frac{5\,\mathrm{p}_2\,\mathrm{v}_1}{4}-\frac{3\,\mathrm{p}_3}{16}-\frac{\mathrm{p}_1\,\mathrm{p}_2}{16}-\frac{5\,\mathrm{p}_2}{8}-\frac{3\,{\mathrm{p}_1}^2\,\mathrm{v}_1}{4}+\frac{3\,{\mathrm{p}_1}^2}{8}+1\right)
\end{aligned}
\tag{D.13}
$$

Static structure factor of the symmetric spin observable $S_{z,1}+S_{z,2}$ for the two-leg ladder in the one-particle sector up to perturbation order 5 (available order 9):

$$
\begin{aligned}
&\left(\frac{5\,\mathrm{p}_2\,\mathrm{p}_3}{96}-\frac{\mathrm{p}_5}{64}-\frac{\mathrm{p}_1\,\mathrm{p}_4}{64}-\frac{\mathrm{p}_4}{32}+\frac{\mathrm{p}_4\,\mathrm{v}_1}{8}-\frac{\mathrm{p}_1\,{\mathrm{p}_2}^2}{48}+\frac{{\mathrm{p}_1}^2\,\mathrm{p}_3}{48}-\frac{{\mathrm{p}_1}^3\,\mathrm{p}_2}{48}\right.\\
&\left.-\frac{{\mathrm{p}_2}^2\,\mathrm{v}_1}{8}+\frac{{\mathrm{p}_2}^2}{32}\right)\cos(k)+\left(\frac{{\mathrm{p}_1}^3\,\mathrm{p}_2}{96}-\frac{\mathrm{p}_3\,{\mathrm{p}_1}^2}{96}+\frac{\mathrm{p}_1\,{\mathrm{p}_2}^2}{96}-\frac{\mathrm{p}_3\,\mathrm{p}_2}{96}\right)\cos(2\,k)\\
&+\left(\frac{\mathrm{p}_4}{32}+\frac{\mathrm{p}_5}{64}+\frac{\mathrm{p}_1\,\mathrm{p}_4}{64}-\frac{\mathrm{p}_2\,\mathrm{p}_3}{24}-\frac{\mathrm{p}_4\,\mathrm{v}_1}{8}+\frac{\mathrm{p}_1\,{\mathrm{p}_2}^2}{96}-\frac{{\mathrm{p}_1}^2\,\mathrm{p}_3}{96}+\frac{{\mathrm{p}_1}^3\,\mathrm{p}_2}{96}+\frac{{\mathrm{p}_2}^2\,\mathrm{v}_1}{8}-\frac{{\mathrm{p}_2}^2}{32}\right)
\end{aligned}
\tag{D.14}
$$

Static structure factor of the spin observable S_z for the dimerized chain in the two-particle sector up to perturbation order 3 (available order 5):

$$
\begin{aligned}
&\left(\frac{\mathrm{p}_1\,\mathrm{p}_2}{192}-\frac{\mathrm{p}_3}{16}-\frac{15\,\mathrm{p}_2}{64}+\frac{15\,\mathrm{p}_2\,\mathrm{v}_1}{32}\right)\cos(k)\\
&+\left(\frac{3\,\mathrm{p}_2}{32}+\frac{\mathrm{p}_3}{64}-\frac{\mathrm{p}_1\,\mathrm{p}_2}{48}-\frac{3\,\mathrm{p}_2\,\mathrm{v}_1}{16}\right)\cos(2\,k)+\left(\frac{\mathrm{p}_1\,\mathrm{p}_2}{32}-\frac{\mathrm{p}_2}{64}+\frac{\mathrm{p}_2\,\mathrm{v}_1}{32}\right)\cos(3\,k)\\
&+-\frac{\mathrm{p}_1\,\mathrm{p}_2}{48}\cos(4\,k)+\frac{(\mathrm{p}_1\,\mathrm{p}_2)}{192}\cos(5\,k)+\left(\frac{5\,\mathrm{p}_2}{32}+\frac{3\,\mathrm{p}_3}{64}-\frac{5\,\mathrm{p}_2\,\mathrm{v}_1}{16}\right)
\end{aligned}
\tag{D.15}
$$

Static structure factor of the symmetric spin observable $S_{z,1}+S_{z,2}$ for the two-leg ladder in the two-particle sector up to perturbation order 4 (available order 5):

$$
\begin{aligned}
&\left(\frac{13\,\mathrm{p}_4}{512}-\frac{\mathrm{p}_3}{16}-\frac{\mathrm{p}_2}{8}-\frac{3\,\mathrm{p}_1\,\mathrm{p}_2}{16}-\frac{3\,\mathrm{p}_1\,\mathrm{p}_3}{128}+\frac{\mathrm{p}_2\,\mathrm{v}_1}{4}-\frac{3\,\mathrm{p}_2\,\mathrm{v}_2}{16}+\frac{3\,\mathrm{p}_3\,\mathrm{v}_1}{16}\right.\\
&+\frac{5\,{\mathrm{p}_1}^2\,\mathrm{p}_2}{64}+\frac{{\mathrm{p}_1}^2\,\mathrm{v}_1}{4}-\frac{3\,\mathrm{p}_2\,{\mathrm{v}_1}^2}{16}-\frac{3\,{\mathrm{p}_1}^2\,\mathrm{v}_2}{16}-\frac{{\mathrm{p}_1}^2}{8}+\frac{17\,{\mathrm{p}_2}^2}{1536}+\frac{7\,{\mathrm{p}_1}^4}{384}-\frac{3\,{\mathrm{p}_1}^2\,{\mathrm{v}_1}^2}{16}\\
&\left.+\frac{9\,\mathrm{p}_1\,\mathrm{p}_2\,\mathrm{v}_1}{16}\right)\cos(k)+\left(-\frac{{\mathrm{p}_1}^4}{48}-\frac{{\mathrm{p}_1}^2\,\mathrm{p}_2}{32}-\frac{{\mathrm{p}_2}^2}{96}\right)\cos(2\,k)+\left(\frac{\mathrm{p}_2}{8}+\frac{\mathrm{p}_3}{16}\right.\\
&-\frac{13\,\mathrm{p}_4}{512}+\frac{3\,\mathrm{p}_1\,\mathrm{p}_2}{16}+\frac{3\,\mathrm{p}_1\,\mathrm{p}_3}{128}-\frac{\mathrm{p}_2\,\mathrm{v}_1}{4}+\frac{3\,\mathrm{p}_2\,\mathrm{v}_2}{16}-\frac{3\,\mathrm{p}_3\,\mathrm{v}_1}{16}-\frac{3\,{\mathrm{p}_1}^2\,\mathrm{p}_2}{64}-\frac{{\mathrm{p}_1}^2\,\mathrm{v}_1}{4}\\
&\left.+\frac{3\,\mathrm{p}_2\,{\mathrm{v}_1}^2}{16}+\frac{3\,{\mathrm{p}_1}^2\,\mathrm{v}_2}{16}+\frac{{\mathrm{p}_1}^2}{8}+\frac{23\,{\mathrm{p}_2}^2}{1536}-\frac{5\,{\mathrm{p}_1}^4}{384}+\frac{3\,{\mathrm{p}_1}^2\,{\mathrm{v}_1}^2}{16}-\frac{9\,\mathrm{p}_1\,\mathrm{p}_2\,\mathrm{v}_1}{16}\right)
\end{aligned}
\tag{D.16}
$$

Static structure factor of the antisymmetric spin observable $S_{z,1}-S_{z,2}$ for the two-leg ladder in the two-particle sector up to perturbation order 4 (available order 5):

$$
\begin{aligned}
&\left(\frac{23\,\mathrm{p}_4}{64}-\frac{\mathrm{p}_3}{8}-\frac{\mathrm{p}_2}{2}+\frac{11\,\mathrm{p}_1\,\mathrm{p}_2}{24}-\frac{47\,\mathrm{p}_1\,\mathrm{p}_3}{36}+\mathrm{p}_2\,\mathrm{v}_1-\mathrm{p}_2\,\mathrm{v}_2+\frac{3\,\mathrm{p}_3\,\mathrm{v}_1}{8}-\frac{209\,{\mathrm{p}_1}^2\,\mathrm{p}_2}{288}\right.\\
&-{\mathrm{p}_1}^2\,\mathrm{v}_1-\frac{\mathrm{p}_2\,{\mathrm{v}_1}^2}{2}+{\mathrm{p}_1}^2\,\mathrm{v}_2+{\mathrm{p}_1}^3\,\mathrm{v}_1+\frac{{\mathrm{p}_1}^2}{2}-\frac{{\mathrm{p}_1}^3}{3}+\frac{23\,{\mathrm{p}_2}^2}{18}+\frac{227\,{\mathrm{p}_1}^4}{576}\\
&\left.+\frac{{\mathrm{p}_1}^2\,{\mathrm{v}_1}^2}{2}-\frac{11\,\mathrm{p}_1\,\mathrm{p}_2\,\mathrm{v}_1}{8}\right)\cos(k)+\left(\frac{187\,{\mathrm{p}_1}^2\,\mathrm{p}_2}{288}-\frac{7\,\mathrm{p}_1\,\mathrm{p}_3}{36}-\frac{\mathrm{p}_1\,\mathrm{p}_2}{3}-{\mathrm{p}_1}^3\,\mathrm{v}_1\right.\\
&\left.+\frac{{\mathrm{p}_1}^3}{3}-\frac{5\,{\mathrm{p}_2}^2}{18}-\frac{17\,{\mathrm{p}_1}^4}{96}+\mathrm{p}_1\,\mathrm{p}_2\,\mathrm{v}_1\right)\cos(2\,k)+\left(\frac{{\mathrm{p}_1}^4}{6}-\frac{{\mathrm{p}_1}^2\,\mathrm{p}_2}{6}\right)\cos(3\,k)\\
&+\left(\frac{\mathrm{p}_2}{2}+\frac{\mathrm{p}_3}{8}-\frac{23\,\mathrm{p}_4}{64}-\frac{\mathrm{p}_1\,\mathrm{p}_2}{8}+\frac{3\,\mathrm{p}_1\,\mathrm{p}_3}{2}-\mathrm{p}_2\,\mathrm{v}_1+\frac{3\,\mathrm{p}_2\,\mathrm{v}_2}{2}-\frac{3\,\mathrm{p}_3\,\mathrm{v}_1}{8}\right.\\
&\left.+\frac{{\mathrm{p}_1}^2\,\mathrm{p}_2}{8}+{\mathrm{p}_1}^2\,\mathrm{v}_1-\frac{3\,{\mathrm{p}_1}^2\,\mathrm{v}_2}{2}-\frac{{\mathrm{p}_1}^2}{2}-\frac{163\,{\mathrm{p}_2}^2}{192}-\frac{5\,{\mathrm{p}_1}^4}{12}+\frac{3\,\mathrm{p}_1\,\mathrm{p}_2\,\mathrm{v}_1}{8}\right)
\end{aligned}
\tag{D.17}
$$

E. Figures

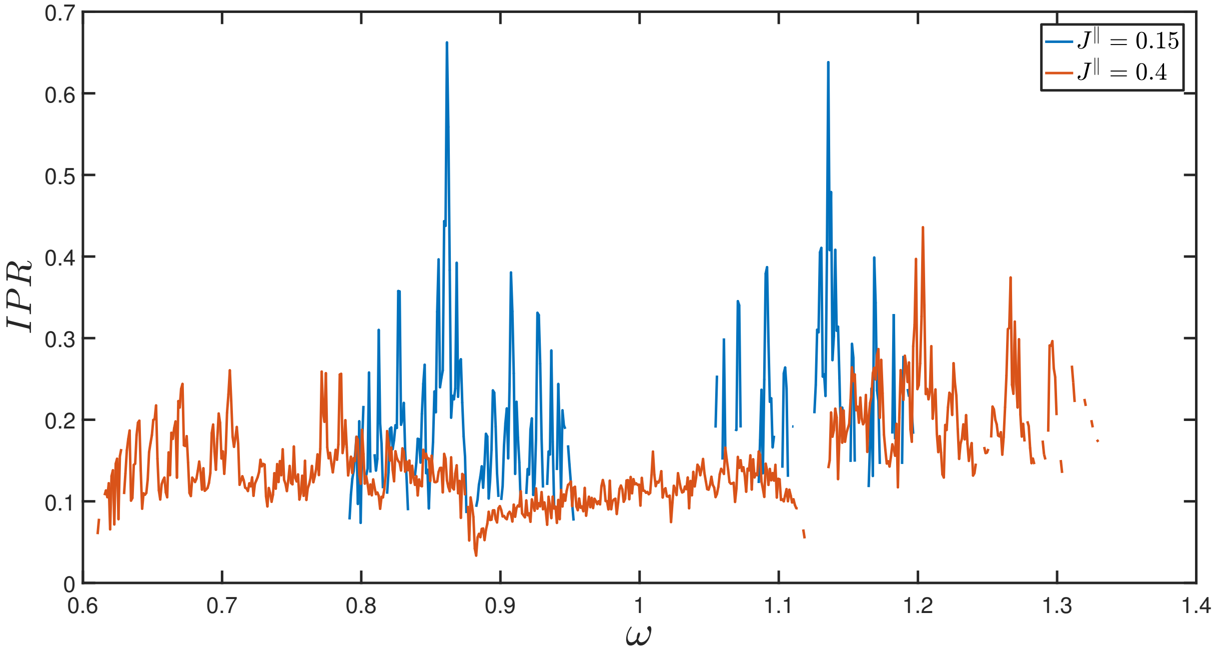

Fig. E.1: For a rung disorder of $P(J^{\perp} = 1.125) = 0.4$, $P(J^{\perp} = 0.875) = 0.6$ and two different leg couplings (blue curve $J^{\|} = 0.15$, red curve $P(J^{\perp} = 1.125) = 0.4$) the inverse participation ratio of the dimerized chain is plotted. The system size was $N = 100$, the energy bin width $\Delta\omega = 0.001$ and it was averaged over $R = 100$ samples. The plot clearly shows that stronger leg couplings damp the localization effect of rung disorder.

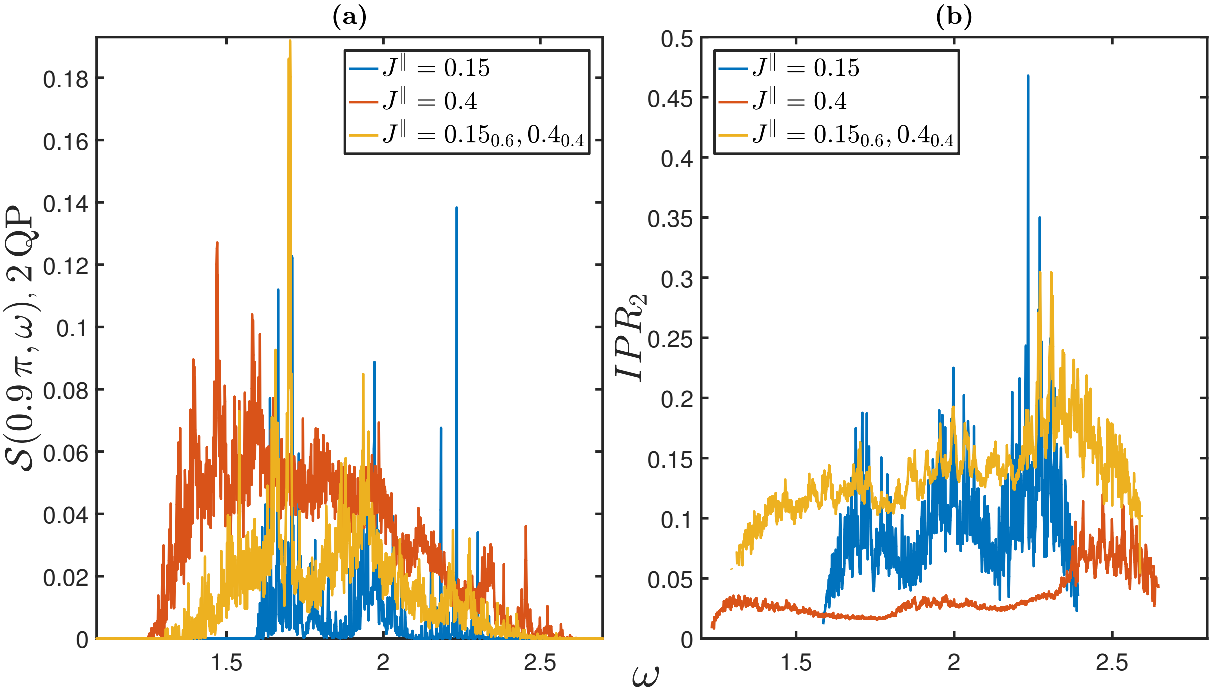

Fig. E.2: The two-triplon dynamic structure factor of the dimerized chain as well as its generalized inverse participation ratio is plotted for three different disorder configurations. System size was $N = 100$, energy bin width $\Delta\omega = 0.001$ and it was averaged over $R = 100$ samples. The blue curve belongs to a rung disorder configuration of $P(J^{\perp} = 1.125) = 0.4$, $P(J^{\perp} = 0.875) = 0.6$ and $J^{\|} = 0.15$. In red one sees a rung disorder configuration of $P(J^{\perp} = 1.125) = 0.4$, $P(J^{\perp} = 0.875) = 0.6$ and $J^{\|} = 0.4$ and in yellow a rung and leg disorder configuration of $P(J^{\perp} = 1.125) = 0.4$, $P(J^{\perp} = 0.875) = 0.6$, $P(J^{\|} = 0.4) = 0.4$ and $P(J^{\|} = 0.15) = 0.6$ is plotted. The IPR_2 shows no finite-size scaling anymore. The two-triplon states of the dimerized chain are thus localized in the two-triplon position basis for these disorder configurations.

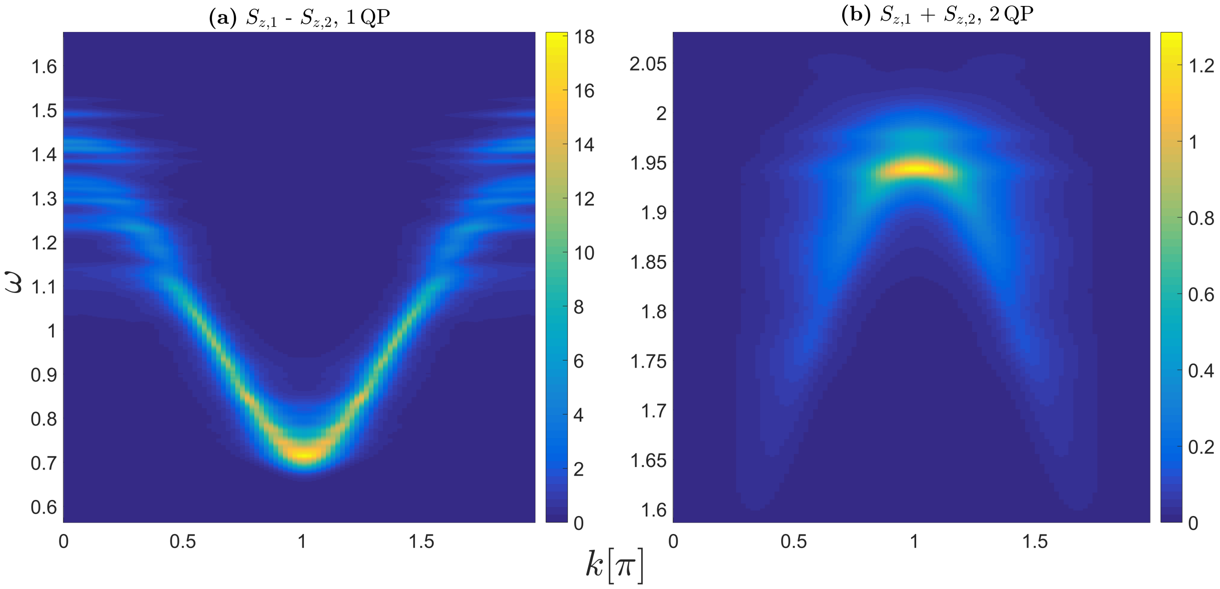

Fig. E.3: Dynamic structure factors of the ladder for the antisymmetric observable in the one-triplon (left plot) and the symmetric observable in the two-triplon channel (right plot) calculated by averaging $R = 100$ samples of system size $N = 100$ and after that broadening with a Lorentzian curve of FWHM of 0.01 are shown. The disorder was leg disorder of the form $P(J^{\|} = 0.15) = 0.6$ and $P(J^{\|} = 0.5) = 0.4$. The curve of the antisymmetric observable looks like it tears apart at energies of $\omega > 1.1$ and also shows points with nearly vanishing DOS in this energy range. In the two-triplon sector it looks like the bound states of the pure cases have widened due to disorder-driven localization of the energy eigenstates.

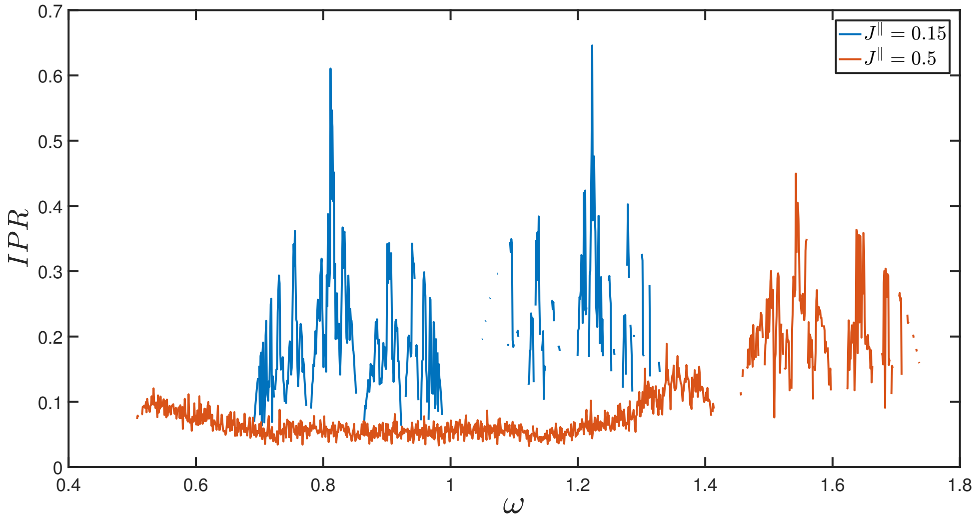

Fig. E.4: The inverse participation ratio of the ladder was calculated for the two different rung disorder configurations $P(J^{\perp} = 1.175) = 0.4$, $P(J^{\perp} = 0.875) = 0.6$ and $J^{\parallel} = 0.15$ (blue curve) and $P(J^{\perp} = 1.175) = 0.4$, $P(J^{\perp} = 0.825) = 0.6$ and $J^{\parallel} = 0.5$ (red curve) by averaging $R = 100$ samples of system size $N = 100$ with an energy bin width of $\Delta\omega = 1/1000$. One can clearly see that higher leg couplings lead to a decrease in the IPR although the rung disorder remains the same.

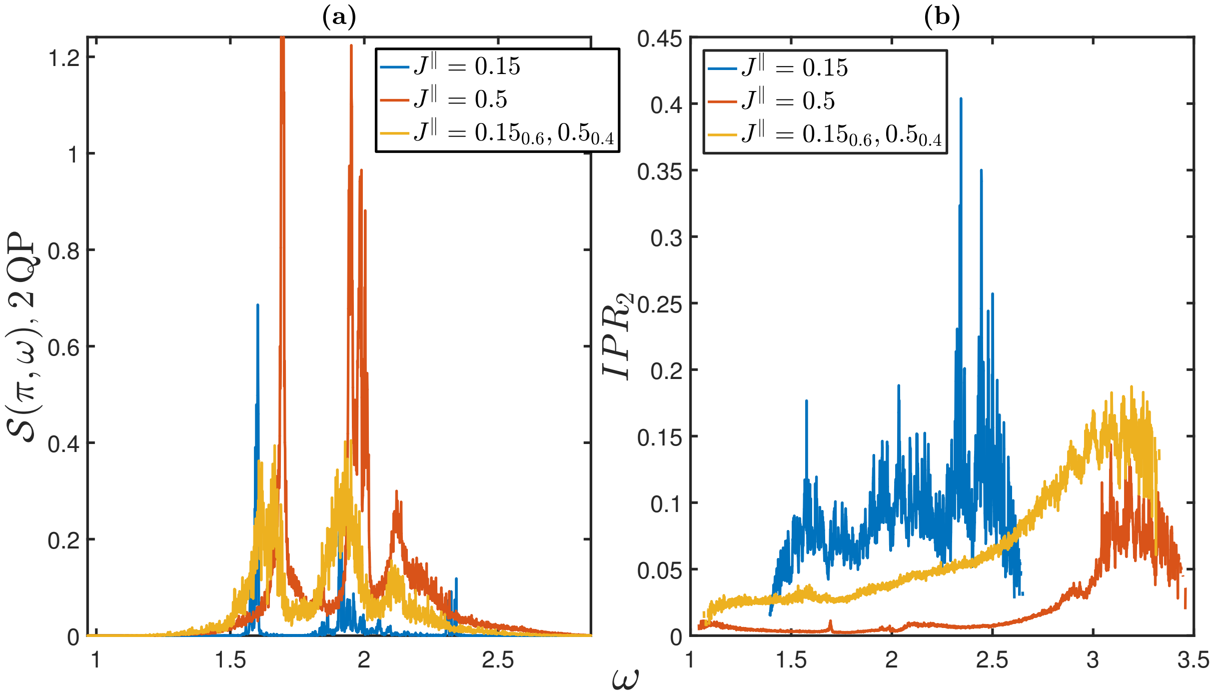

Fig. E.5: The two-triplon dynamic structure factor of the symmetric observable at $k = \pi$ as well as the generalized inverse participation ratio is plotted for three different rung disorder configurations. System size was $N = 100$, energy bin width $\Delta\omega = 0.001$ and it was averaged over $R = 100$ samples. The blue curve belongs to a rung disorder configuration of $P(J^{\perp} = 1.175) = 0.4$, $P(J^{\perp} = 0.875) = 0.6$ and $J^{\parallel} = 0.15$. In red one sees a rung disorder configuration of $P(J^{\perp} = 1.175) = 0.4$, $P(J^{\perp} = 0.825) = 0.6$ and $J^{\parallel} = 0.5$ and in yellow a rung and leg disorder configuration of $P(J^{\perp} = 1.175) = 0.4$, $P(J^{\perp} = 0.875) = 0.6$, $P(J^{\parallel} = 0.5) = 0.6$ and $P(J^{\parallel} = 0.15) = 0.4$ is plotted. The IPR_2 shows no finite-size scaling anymore. The two triplons of the dimerized chain are thus localized in the two-triplon position basis for these disorder configurations. Another interesting point is that the dynamic structure factor of the rung and leg disorder configuration appears smoother.

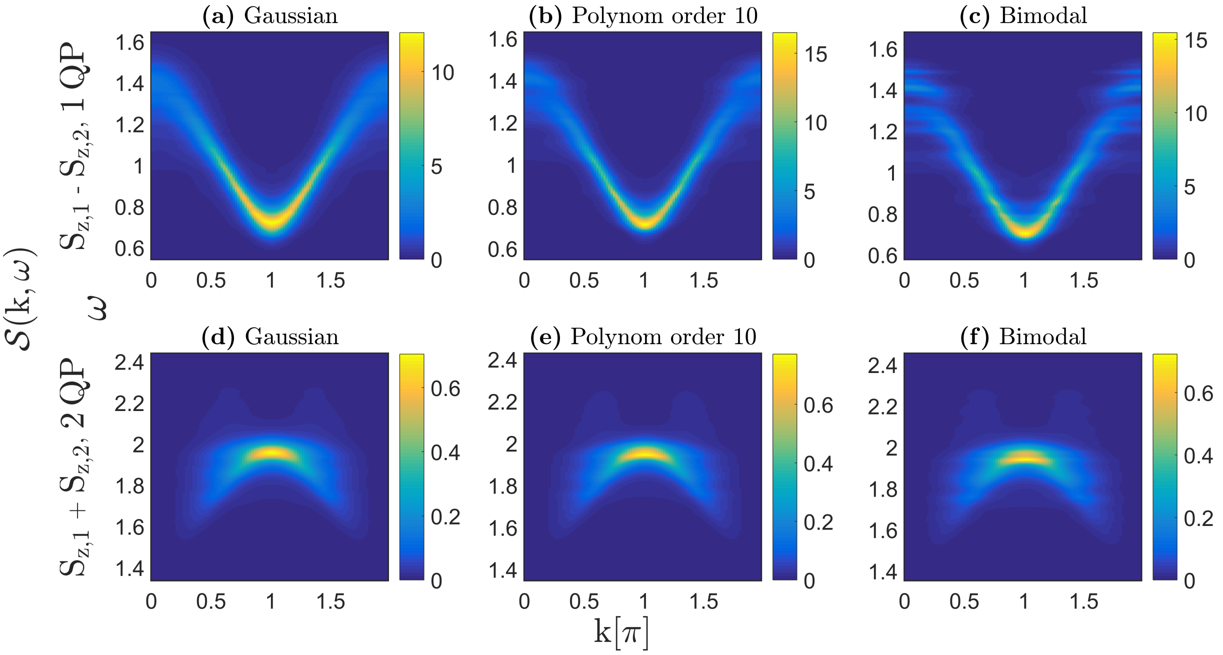

Fig. E.6: All plots were obtained by system sizes of $N = 100$, $R = 100$ samples and FWHM of the Lorentzian broadening of 0.02 and show the dynamic structure factor of the antisymmetric observable in the one-triplon and the symmetric observable in the two-triplon sector.
(a) and (d): Gaussian leg disorder of $\mathrm{Var}(J^{\|}_{\nu}) = 0.2^2$ and $\left\langle J^{\|}_{\nu} \right\rangle = 0.3$.
(b) and (e): Polynomial leg disorder of $J^{\|}_{\mathrm{max}} = 0.5$, $J^{\|}_{\mathrm{min}} = 0.1$, $P(J^{\|}) \propto (J^{\|} - 0.3)^{10}$ and $\left\langle J^{\|}_{\nu} \right\rangle = 0.3$.
(c) and (f): Bimodal leg disorder of $P(J^{\|} = 0.5) = 0.5$, $P(J^{\|} = 0.1) = 0.5$.

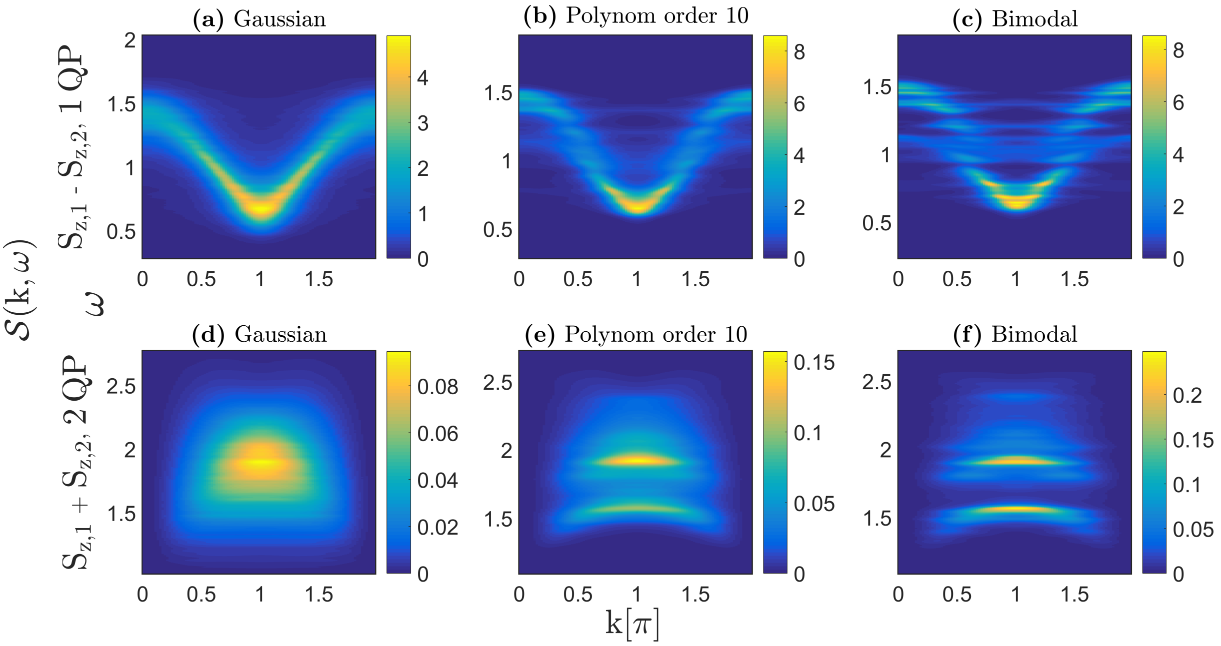

Fig. E.7: All plots were obtained by system sizes of $N = 100$, $R = 100$ samples and FWHM of the Lorentzian broadening of 0.02 and show the dynamic structure factor of the antisymmetric observable in the one-triplon sector (upper row) and the symmetric observable in the two-triplon sector.
(a) and (d): Gaussian rung disorder of $\mathrm{Var}(J_\nu^\perp) = 0.2^2$, $\langle J_\perp \rangle = 1$ and $J_\parallel = 0.3$.
(b) and (e): Polynomial probability distribution for the rung $P(J^\perp) \propto {J^\perp}^{10}$, $J^\parallel = 0.3$ and $J^\perp_{\mathrm{max}} = 1.2$, $J^\perp_{\mathrm{min}} = 0.8$.
(c) and (f): Bimodal rung disorder of $P(J^\perp = 1.2) = 0.5$, $P(J^\perp = 0.8) = 0.5$ and $J^\parallel = 0.3$.

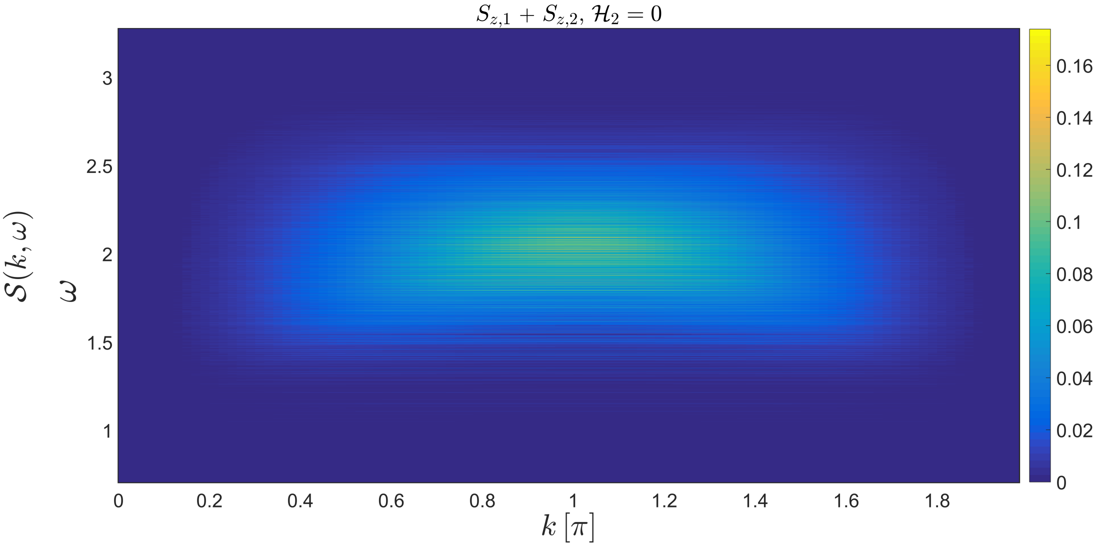

Fig. E.8: The plot shows the dynamic structure factor of the symmetric observable for Gaussian rung disorder of $\mathrm{Var}(J_\nu^\perp) = 0.2^2$, $\langle J_\perp \rangle = 1$ and $J_\| = 0.3$. System size is $N = 100$ and $R = 100$ samples were used. Energy bin width was $1/1000$. The two-particle interactions were switched off. The difference to the plot with two-particle interactions (see Fig. 4.19) is much smaller than in the bimodal disorder case.

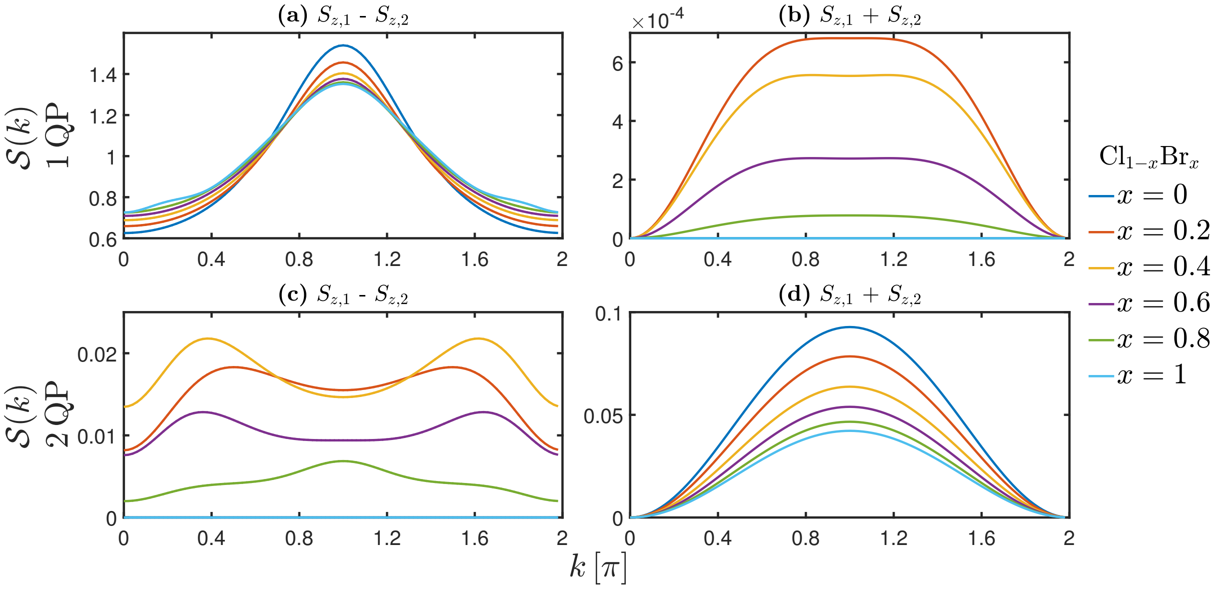

Fig. E.9: The plot shows the static structure factor of BPCBC for the symmetric and antisymmetric observable in the one- and two-triplon sector for different bromine concentrations and a system size of $N = 100$ and $R = 100$ samples.

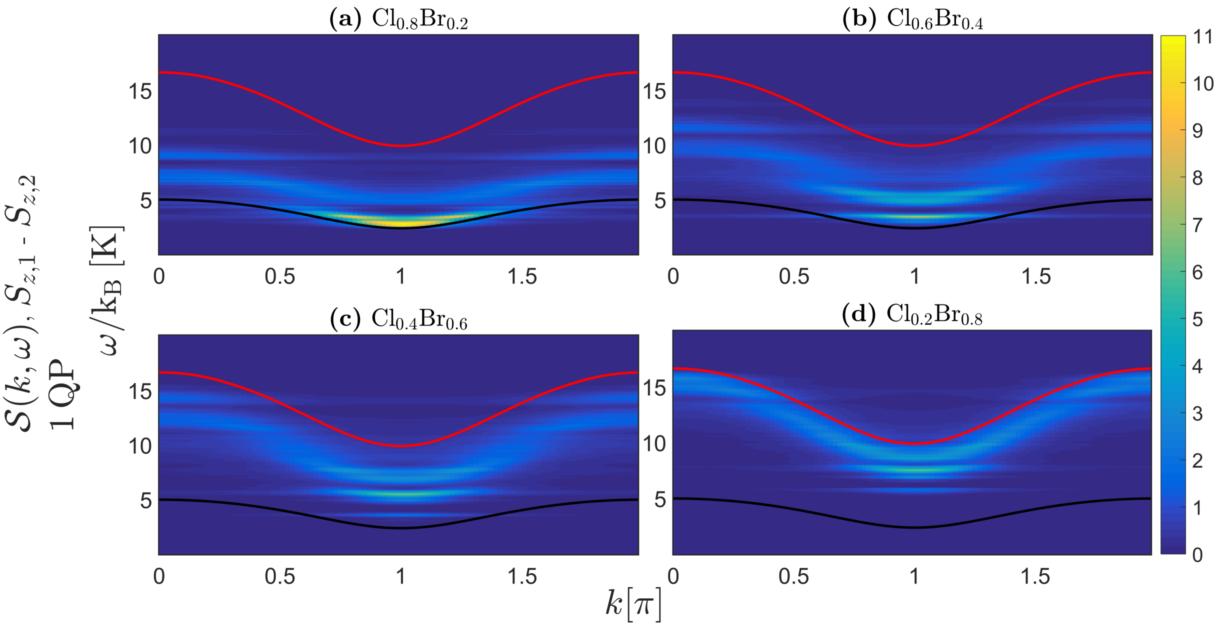

Fig. E.10: All plots were obtained by system sizes of $N = 100$, $R = 100$ samples and FWHM of the Lorentzian broadening of $0.08\,\mathrm{k_B}\,\mathrm{K}$ and show the dynamic structure factor of the antisymmetric observable in the one-triplon sector. They show the weight with the same colour scale and have same energy scales to show the changes in the dynamic structure factor when the concentration of bromine is gradually increased.
(a)-(d): The ratio of bromine atoms increases in steps of 20% from 0.2 to 0.8. The red curve shows the pure bromine dispersion and the black one the pure chlorine dispersion. The weight gradually shifts to higher energies as the concentration of bromine is increased. One can see dispersion-like structures belonging to each of the five different possible rung coupling values. The more likely the value is to be taken the more dispersion-like appear the structures. Values that are only taken rarely lead to stripe-like structures.

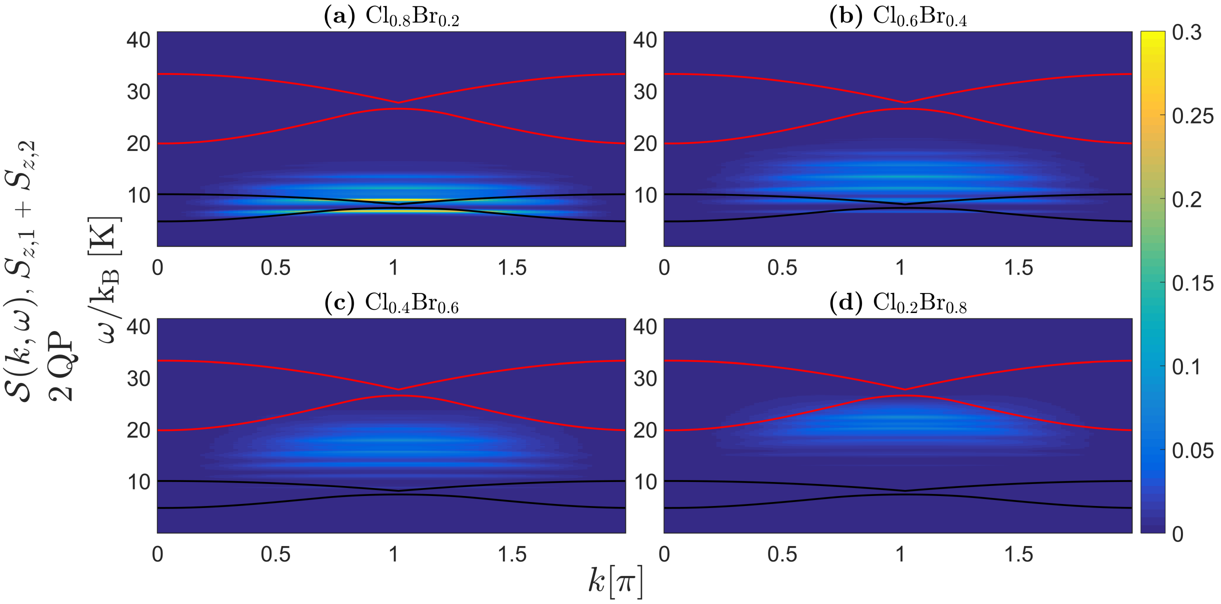

Fig. E.11: All plots were obtained by system sizes of $N = 100$, $R = 100$ samples and FWHM of the Lorentzian broadening of $0.08\,\mathrm{k_B\,K}$ and show the dynamic structure factor of the symmetric observable in the two-triplon sector. They show the weight with the same colour scale and have same energy scales to show the changes in the dynamic structure factor when the concentration of bromine is gradually increased.
(a)-(d): The ratio of bromine atoms increases in steps of 20% from 0.2 to 0.8. Red curves show the band edges of the continuum in the pure bromine case and black curves in the pure chlorine case. Bound states change to stripes with strong weight in the disordered configurations. For the cases of 20% and 40% bromine ((a) and (b)) the bound states can still be quite well resolved despite of the Lorentzian broadening. In the 20% bromine case the lowest-lying bound state is even separated and and its width is only slightly bigger than in the case of pure chlorine.

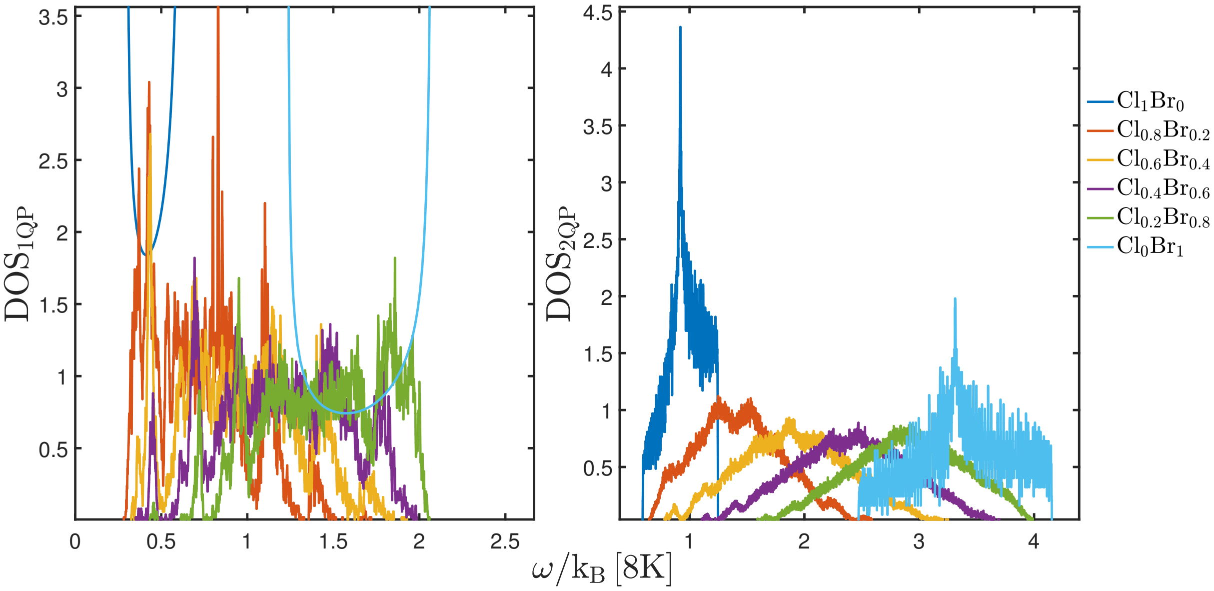

Fig. E.12: The density of states was calculated for the disordered material $\mathrm{BPCB}_x\mathrm{C}_{1-x}$ by averaging $R = 100$ samples of system size $N = 100$ with an energy bin width of $\Delta\omega = 0.008\,\mathrm{k_B}\,\mathrm{K}$. For the one-triplon sector the so obtained DOS was smoothed by a moving average filter with span of 5 energy bins. What one can clearly see is that the DOS in both the one- and two-triplon case is distributed flatter and over a wider range of energies in the disordered cases. One can also see several maxima and minima in the densities of states of the disordered materials that were not present in the non-disordered cases.

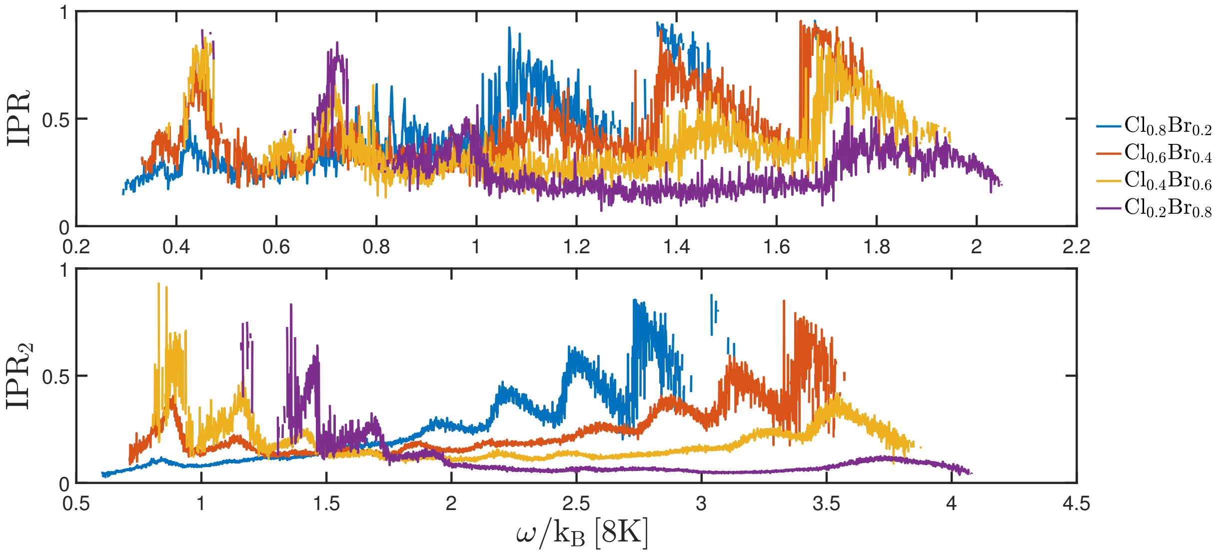

Fig. E.13: The inverse participation ratio and its generalized version for two triplons was calculated for the disordered material $\mathrm{BPCB}_x\mathrm{C}_{1-x}$ by averaging $R = 100$ samples of system size $N = 100$ with an energy bin width of $\Delta\omega = 0.008\,\mathrm{k_B\,K}$. Both quantities did not show any finite-size effects anymore thus leading to conclude that the states are localized for all energies. In the two-triplon sector they are localized in the two-triplon position basis. Another interesting point is that the IPR and the IPR_2 always show their biggest values in the energy ranges that belong to the pure material with smaller concentration in the disordered material. This is due to the fact that couplings that belong to such energy values have a lower probability to be taken.

Bibliography

[1] David J Thouless. Electrons in disordered systems and the theory of localization. *Physics Reports*, 13(3):93–142, 1974.

[2] Subir Sachdev. *Quantum phase transitions*. Wiley Online Library, 2007.

[3] Claudio Castelnovo, Roderich Moessner, and Shivaji L Sondhi. Magnetic monopoles in spin ice. *Nature*, 451(7174):42–45, 2008.

[4] Thomas Vojta. Rare region effects at classical, quantum and nonequilibrium phase transitions. *Journal of Physics A: Mathematical and General*, 39(22):R143, 2006.

[5] Philip W Anderson. Absence of diffusion in certain random lattices. *Physical review*, 109(5):1492, 1958.

[6] Abhijit Mookerjee. Averaged density of states in disordered systems. *Journal of Physics C: Solid State Physics*, 6(8):1340, 1973.

[7] Ferdinand Evers and Alexander D Mirlin. Anderson transitions. *Reviews of Modern Physics*, 80(4):1355, 2008.

[8] DC Herbert and R Jones. Localized states in disordered systems. *Journal of Physics C: Solid State Physics*, 4(10):1145, 1971.

[9] Olexei Motrunich, Kedar Damle, and David A Huse. Dynamics and transport in random quantum systems governed by strong-randomness fixed points. *Physical Review B*, 63(13):134424, 2001.

[10] R Mélin, Y-C Lin, P Lajkó, H Rieger, and F Iglói. Strongly disordered spin ladders. *Physical Review B*, 65(10):104415, 2002.

[11] Yu-cheng Lin. Strongly disordered quantum spin systems in low dimensions-numerical study of spin chains, spin ladders and two-dimensional systems. 2001.

[12] Matthias Vojta. Excitation spectra of disordered dimer magnets near quantum criticality. *Physical review letters*, 111(9):097202, 2013.

[13] Simon Nathan Ernleigh Ward. *Spin ladder physics and the effect of random bond disorder*. PhD thesis, UCL (University College London), 2015.

[14] B Normand and Ch Rüegg. Complete bond-operator theory of the two-chain spin ladder. *Physical Review B*, 83(5):054415, 2011.

[15] Sudha Gopalan, TM Rice, and M Sigrist. Spin ladders with spin gaps: A description of a class of cuprates. *Physical Review B*, 49(13):8901, 1994.

[16] Simon Ward, M Mena, P Bouillot, C Kollath, T Giamarchi, KP Schmidt, B Normand, KW Krämer, D Biner, R Bewley, et al. Bound states and field-polarized haldane modes in a quantum spin ladder. *Physical Review Letters*, 118(17):177202, 2017.

[17] T Lorenz, O Heyer, M Garst, F Anfuso, A Rosch, Ch Rüegg, and Karl Krämer. Diverging thermal expansion of the spin-ladder system $(C_5H_{12}N)_2CuBr_4$. *Physical review letters*, 100(6):067208, 2008.

[18] Subir Sachdev and RN Bhatt. Bond-operator representation of quantum spins: Mean-field theory of frustrated quantum heisenberg antiferromagnets. *Physical Review B*, 41(13):9323, 1990.

[19] T Barnes, E Dagotto, J Riera, and ES Swanson. Excitation spectrum of heisenberg spin ladders. *Physical Review B*, 47(6):3196, 1993.

[20] DG Shelton, AA Nersesyan, and AM Tsvelik. Antiferromagnetic spin ladders: Crossover between spin $S = 1/2$ and $S = 1$ chains. *Physical Review B*, 53(13):8521, 1996.

[21] Hans Bethe. Zur Theorie der Metalle. *Zeitschrift für Physik*, 71(3-4):205–226, 1931.

[22] Christian Knetter, Kai P Schmidt, and Götz S Uhrig. High order perturbation theory for spectral densities of multi-particle excitations: two-leg heisenberg ladder. *The European Physical Journal B-Condensed Matter and Complex Systems*, 36(4):525–544, 2003.

[23] Kai Phillip Schmidt. *Spectral properties of quasi one-dimensional quantum antiferromagnets. Perturbative continuous unitary transformations*. PhD thesis, Universität zu Köln, 2004.

[24] George Theodorou and Morrel H Cohen. Extended states in a one-demensional system with off-diagonal disorder. *Physical Review B*, 13(10):4597, 1976.

[25] Kazushige Ishii. Localization of eigenstates and transport phenomena in the one-dimensional disordered system. *Progress of Theoretical Physics Supplement*, 53:77–138, 1973.

[26] Christian Harrer. Green'sche Funktionen ungeordneter Quantensysteme. Diplomarbeit, Universität Bayreuth, 2008.

[27] Hirotsugu Matsuda. Special frequencies in the vibrational spectra of disordered chains. *Progress of theoretical physics*, 31(1):161, 1964.

[28] Franz Wegner. Flow-equations for hamiltonians. *Annalen der physik*, 506(2):77–91, 1994.

[29] Stanisław D Głazek and Kenneth G Wilson. Renormalization of hamiltonians. *Physical Review D*, 48(12):5863, 1993.

[30] Christian Knetter and Goetz S Uhrig. Perturbation theory by flow equations: dimerized and frustrated s= 1/2 chain. *The European Physical Journal B-Condensed Matter and Complex Systems*, 13(2):209–225, 2000.

[31] Jürgen Stein. Flow equations and the strong-coupling expansion for the hubbard model. *Journal of statistical physics*, 88(1):487–511, 1997.

[32] Andreas Mielke. Flow equations for band-matrices. *The European Physical Journal B-Condensed Matter and Complex Systems*, 5(3):605–611, 1998.

[33] Cécile Monthus. Flow towards diagonalization for many-body-localization models: adaptation of the toda matrix differential flow to random quantum spin chains. *J. Phys. A Math. Theor*, 49:305002, 2016.

[34] K Coester and KP Schmidt. Optimizing linked-cluster expansions by white graphs. *Physical Review E*, 92(2):022118, 2015.

[35] Christian Knetter. *Perturbative continuous unitary transformations: spectral properties of low dimensional spin systems*. PhD thesis, Universität zu Köln, 2003.

[36] Christian Knetter, Kai P Schmidt, and Götz S Uhrig. The structure of operators in effective particle-conserving models. *Journal of Physics A: Mathematical and General*, 36(29):7889, 2003.

[37] KP Schmidt, C Knetter, and GS Uhrig. Novel extrapolation for strong coupling expansions. *arXiv preprint cond-mat/0208358*, 2002.

[38] Sebastian Kirschner. Multi-particle spectral densities. Diplomarbeit, Universität zu Köln, 2004.

[39] Paul M Stevenson. Optimized perturbation theory. *Physical Review D*, 23(12):2916, 1981.

[40] RRP Singh and AP Young. Critical and griffiths-mccoy singularities in quantum ising spin-glasses on d-dimensional hypercubic lattices: A series expansion study. *arXiv preprint arXiv:1707.01557*, 2017.

Erklärung

Ich versichere, dass ich meine Masterarbeit ohne Hilfe Dritter und ohne Benutzung anderer als der angegebenen Quellen und Hilfsmittel angefertigt habe und die aus benutzten Quellen wörtlich oder inhaltlich entnommenen Stellen als solche kenntlich gemacht habe. Diese Arbeit hat in gleicher oder ähnlicher Form noch keiner Prüfungsbehörde vorgelegen.

Erlangen, den 14. August 2017

Max Hörmann

Danksagungen

Ich möchte mich an dieser Stelle bei Prof. Dr. Kai Phillip Schmidt für seine große Geduld und die Zeit, die er sich stets genommen hat, bedanken. Er half mir dabei, Verständnis für die betrachteten Spin-Modelle zu gewinnen und betreute mich gut.
Paul Wunderlich danke ich für seine vergleichende Arbeit mittels Molekularfeldnäherung und die interessanten Diskussionen. Insgesamt danke ich der Schmidt-Gruppe für das angenehme und auch erheiternde Klima. Genauso danke ich meinen Bürokollegen und den Kollegen vom Theorie I Lehrstuhl für den entspannten Umgang miteinander. Meiner Familie und insbesondere meiner Mutter danke ich für die immer währende Unterstützung während meines Studiums.